COMPOSITION, STRUCTURE, DYNAMICS AND FUNCTION OF C-TYPE LECTIN RECEPTOR DOMAINS

Michelle S. Itano

A dissertation submitted to the faculty of the University of North Carolina at Chapel Hill in partial fulfillment of the requirements for the degree of Doctor of Philosophy in the Department of Cell and Developmental Biology.

Chapel Hill
2012

Approved by:

Ken Jacobson, Ph.D.

Con Beckers, Ph.D.

Robin S. Broughton, Ph.D.

Douglas Cyr, Ph.D.

Ronald Swanstrom, Ph.D.

Nancy L. Thompson, Ph.D.

ABSTRACT

MICHELLE S. ITANO: Composition, Structure, Dynamics and Function of C-Type Lectin Receptor Domains
(Under the direction of Ken Jacobson)

DC-SIGN, a Ca^{2+}-dependent C-type transmembrane lectin, is found assembled in microdomains on the plasma membranes of dendritic cells. These microdomains bind a large variety of pathogens and facilitate their uptake for subsequent antigen presentation. In these studies, DC-SIGN dynamics and distribution in microdomains have been explored with several fluorescence microscopy methods and compared with those for influenza hemagglutinin (HA), which is also found in plasma membrane microdomains. Fluorescence recovery after photobleaching (FRAP), line-scan fluorescence correlation spectroscopy and defined valency quantum dot single particle tracking measurements showed that full-length and cytoplasmically truncated DC-SIGN is essentially immobilized in microdomains, whereas HA is laterally mobile within and outside microdomains and exchanges between these two regions. By contrast, FRAP measurements indicated that inner leaflet lipids are able to move through DC-SIGN microdomains. Wide-field fluorescence imaging indicated that DC-SIGN microdomains may contain other C-type lectins and that the DC-SIGN cytoplasmic region is not required for microdomain formation. A super-resolution imaging technique, Blink Microscopy (Blink), was applied to further investigate the lateral distribution of DC-SIGN. Blink indicates that DC-SIGN, another C-type lectin (CD206), and HA are all

localized in small (~80 nm in diameter) nanodomains. DC-SIGN and CD206 nanodomains are randomly distributed on the plasma membrane, whereas HA nanodomains cluster on length scales up to several microns. We estimate, as a lower limit, that DC-SIGN and HA nanodomains contain on average two tetramers or two trimers, respectively, while CD206 is often non-oligomerized. Two-color Blink determined that different C-type lectins rarely occupy the same nanodomain although they appear co-localized using widefield microscopy. Thus, a novel domain structure emerges in which elemental nanodomains, potentially capable of binding viruses, are organized in a random fashion; evidently, these nanodomains can be clustered into larger microdomains that act as receptor platforms for larger pathogens like yeasts. These results contribute significantly to a young field directed at elucidation of the complex intradomain structural features underlying function.

DEDICATION

To my parents, sister, and grandparents:

for “walking in the rain by my side… and loving more than anybody can;”

And to my husband, Kevin:

for “all those times I’ve told myself to hold onto as they pass.”

ACKNOWLEDGMENTS

The work presented in this thesis would not have been possible without the combined efforts by a community of people too large to specifically thank by name. I am deeply grateful to them all, and I would specifically like to acknowledge the following people who have helped shape my scientific career.

I am deeply and sincerely grateful to my advisor Ken Jacobson, who has been a mentor to me in the truest sense of the word. I am particularly grateful for his unwavering support for this project and my career, and for making possible all of the incredible opportunities I have had throughout my graduate career. He has undeniably been the driving force to positively shape me into the scientist I am today, and am yet to become.

I cannot go further without expressing my appreciation to Nancy L. Thompson, in addition to serving on my committee and providing numerous reference letters on my behalf, she has acted as a second mentor and advisor to me. I am deeply grateful for her commitment to ensure that our work is performed and presented at the highest quality possible and for all of the lessons that I have learned under her guidance.

I would like to thank all of my committee members, including Con Beckers, Robin S. Broughton, Doug Cyr, and Ron Swanstrom, for providing guidance and

enthusiastic support throughout my graduate career. I am honored to have worked with each of you.

All of the former and current members of the Jacobson Lab have helped make North Carolina into a home for me with their support, friendship, and engaging discussion. Particularly, I would like to thank: Robin S. Broughton for teaching me how to culture cells and her encouragement; Yun Chen for teaching me how to work with quantum dots; Ping Liu for being a true collaborator and hard-working colleague throughout these investigations on DC-SIGN; and Aaron K. Neumann for laying all of the important groundwork for these studies on DC-SIGN, for teaching me everything I know about the C-type lectins, and for his continued advice and perceptive insight.

Much of the work contained in this thesis would have been impossible without the aid of many scientific collaborators. I would particularly like to thank Michelle Digman, Carsten Forthmann, Enrico Gratton, Wolfgang Parak, Jürgen Schmied, Christian Steinhauer, Philip Tinnefeld, Xiang Wang, and Feng Zhang for their invaluable contributions. I sincerely appreciate all of the members of the Tinnefeld lab for graciously welcoming me into their lab and homes during my three trips to collect data in Germany.

I am also grateful to members of the extended UNC community whose support has been particularly meaningful to my graduate career: the faculty and staff of the Department of Cell and Developmental Biology, particularly Vytas Bankaitis for his help

mediating my transition into the department and into the Jacobson Lab; the opportunities provided by the staff of the Training Initiative in Biomedical and Biological Sciences, particularly by Josh Hall and Pat Phelps; the staff on the executive committee of the Biological and Biomedical Sciences Program who always respected my ideas and treated me as a colleague; and the staff of the UNC-Olympus Research Imaging Center for providing training and state-of-the-art equipment.

I would also like to thank those who I worked with in the past, but have left an undeniable footprint on my career. I am immensely grateful to Lois Abbott, for giving me unlimited access to her lab for four and a half years, for introducing me to biological research, for encouraging me, and for always treating me as a colleague. I find this to be all the more incredible because I was only 13 years old when I started working in her lab. I also owe a deep gratitude to Sarah C.R. Elgin, who has been a true mentor to me since college, and for the experiences in her lab, which were the main reason that I decided to pursue a career in biological and not archaeological research. I am continually grateful to her for teaching me the value of meaningful collaboration and of communicating science effectively and with enthusiasm.

I am exceedingly grateful to my extended family of friends, whose support has been invaluable to me. I would particularly like to thank Ian Carbone, Michael and Elisha Johnson, Punya Navaratnarajah, Samantha Roberts, Leah Watson, and Katie Wolfe for their friendship, for always believing the best in me, and for never ceasing to make me smile. No two people have done more to make North Carolina feel like home for me than

Kiani and Matthew Gardner, and I wish I had more eloquent words to express the deep and sincerest gratitude I feel for their friendship.

As I conclude my graduate career, I am more grateful than ever for the unconditional love and support I have received from my entire family. I would like to thank my in-laws, Bob and Debbie Bastian, who have always loved me as a daughter, are two of the most hard-working and generous people I have ever known, and who have been two of my fiercest and constant advocates. I am so proud to be the granddaughter of four of the most incredibly loving, courageous and honorable people I have ever met: Harvey and Rose Itano, and Ben and Alice Yoshinaga. I carry with me the legacy of my grandfathers; who did not live to see this day, but who, with my grandmothers, always believed that it would come. I am grateful to have always had a hero in my life to look up to, my sister Nicole Itano, whose courage and passion for life always inspires me; and to Barnaby Phillips, my brother-in-law, the only person I have ever met who is an equal match for Nicole's compassion towards people and thrill for adventure. I owe everything I have accomplished to my parents, Wayne and Chris Itano, who have never doubted, or allowed me to doubt, that I could fulfill my dreams. I thank them for being my ultimate role models, for defining unconditional love, and for instilling in me a love for science and for talking about science long before I ever stepped foot in a lab. And finally, I want to express my deepest gratitude for the daily and unconditional support I receive from my husband, Kevin Bastian, who has been my partner on this journey and has made me happier than I ever dreamed that I could be.

TABLE OF CONTENTS

LIST OF TABLES

LIST OF FIGURES

LIST OF ABBREVIATIONS AND SYMBOLS

% – percent

° – degree

AA – asorbic acid

AF1859 – goat polyclonal IgG specific for human dectin-1

AF2534 – goat polyclonal IgG specific for human CD206

AIDS – acquired immune deficiency syndrome

Blink – Blink Microscopy

BSA – bovine serum albumin

C – Celsius

Ca^{2+} – calcium cation

CBP – carboxyl-terminal Src kinase-binding protein

CCD – charge-coupled device

CLR – C-type lectin

cm – centimeter

CMOS – complementary metal-oxide semiconductor

CNS – Crystallography and NMR System

CON.1 – mouse monoclonal IgG2b specific for clathrin light chain from a variety of species

CSK – carboxyl-terminal Src kinase

C-terminus, C-term – carboxy terminus

CTL – C-type lectin

C-type – calcium dependent

CW – continuous wave

D – apparent diffusion coefficient

DC – dendritic cell

DCN46 – mouse monoclonal IgG2b specific for human DC-SIGN

DC-SIGN – dendritic cell-specific intracellular adhesion molecule-3-grabbing non-integrin

DC6 – mouse monoclonal IgG1 specific for human DC-SIGN

Δ35-MX-DCSIGN – NIH 3T3 cell line stably expressing human DC-SIGN with 35 amino acids truncated from the cytoplasmic region

Δ20-MX-DCSIGN – NIH 3T3 cell line stably expressing human DC-SIGN with 20 amino acids truncated from the cytoplasmic region

DIC – differential interference contrast

DMEM – Dulbecco's modified eagle medium

DMF – dimethylformamide

DNA – deoxyribonucleic acid

DOL – degree of labeling

DPBS – Dulbecco's phosphate-buffered saline

dSTORM – direct stochastic optical reconstruction microscopy

DTT – D,L-dithiothreitol

eB-h209 – biotinylated, rat monoclonal IgG2a specific for human DC-SIGN

EBP50-ERM – Ezrin-binding phosphoprotein 50-ezrin/radixin/moesin

EGFP – enhanced green fluorescent protein

EM – electron-multiplying

EMCCD – electron-multiplying charge coupled device

Fab – fragment, antigen-binding

FBS – fetal bovine serum

FC125 – mouse monoclonal IgG2a specific for HA

FCS – fluorescence correlation spectroscopy

FLIM – fluorescence lifetime imaging microscopy

FPALM – fluorescence photoactivation localization microscopy

FRAP – fluorescence recovery after photobleaching

FRET – Förster resonance energy transfer

FWHM – full width at half maximum

g – gram

g – gravitational acceleration

GM-CSF – ganulocyte-macrophage colony-stimulating factor

GM1 – monosialotetrahexosylganglioside

GPI – glycosylphosphatidylinositol

GSDIM – ground state depletion microscopy followed by individual molecule return

h – hour

HA – hemagglutinin

HAb2 – NIH 3T3 cell line stably expressing HA from the Japan strain of influenza

HA-7 – biotinylated, mouse monoclonal IgG1 specific for HA

HCL – hydrochloric acid

Hg– mercury

HIV – human immunodeficiency virus

HIV-1 – human immunodeficiency virus type 1

H-200 – rabbit polyclonal IgG specific for human DC-SIGN

Hz – hertz

IgG – immunoglobulin G

IL-4 – interleukin 4

KCL – potassium chloride

kHz – kilohertz

KS – Src-family kinase substrates

L – liter

LC – light chain

M – molar

ME – 2(β)-mercaptoethanol

MEA – mercaptoethylamine

mg – milligram

μ – micro

μg – microgram

μL – microliter

μm – micron

μM – micromole

μW – microwatt

min – minutes

mL – milliliters

mm – millimeter

mM – millimole

MMR – macrophage mannose receptor

mRFP – monomeric red fluorescent protein

ms – millisecond

MSD – mean squared displacement

MV – methyl viologen

mW – milliWatt

MX-DC-SIGN – NIH 3T3 cells that stably express human DC-SIGN

n – number of trials

N.A. – numerical aperature

ng – nanogram

NHS– N-hydroxysuccinimide

NIAID– National Institute of Allergy and Infectious Disease

NIH – National Institutes of Health

nL – nanoliter

n_{lines} – number of lines

nm – nanometer

nM – nanomole

n_{px} – number of pixels

OD – optical density

O/N – overnight

PAINT – points accumulation for imaging in nanoscale topography

PALM – photoactivated localization microscopy

PAMP – pathogen associated molecular pattern

PBS – phosphate-buffered saline

PCR – polymerase chain reaction

PEG – polyethyleneglycol

PFA – para-formaldehyde

pH – negative log (base 10) of the molar concentration of hydronium ions

P_∞ – recoverable percentage

PIP_2 – phosphatidylinositol 4,5-bisphosphate

PMT – plasma membrane tracer

PSF – point spread function

PTP – protein tyrosine phosphatase

Qdot – quantum dot

QE – quantum efficiency

RESOLFT – reversible saturatable optical fluorescence transitions

ROI – region of interest

RPMI – Roswell Park Memorial Institute

R^2 – coefficient of determination

s – seconds

SEM – standard errors of the means

SFK – Src-family kinases

SFV – Semliki Forest virus

SNR – signal-to-noise ratio

S_1 – first excited single state

SPT – single particle tracking

SR – super-resolution

STALL – stimulation-induced temporary arrest of lateral diffusion

STED – stimulated emission depletion

STORM – stochastic optical reconstruction microscopy

S_0 – ground state

$\tau_{1/2}$ – half-time for recovery

TCEP – tris(2-carboxlethyl)phosphine

TEM – tetraspanin-enriched microdomain

3D – three dimensional

3T3 – mouse embryonic fibroblast

TIR – total internal reflection

TIRF – total internal reflection fluorescence

v – volume

VSV – vesicular stomatitis virus

w – weight

WT – wild type

WZMW – Wissenschaftlichen Zentrums für Material-Wissenschaften (Scientific Center for Materials Science)

CHAPTER 1

Introduction

This chapter contains an overview of the doctoral work described in the six chapters of this dissertation. The research presented in this dissertation will relate to proteins expressed on dendritic cells, the main antigen presenting cells in the immune system. Dendritic cells express receptors, including the C-type lectins, that recognize pathogen-associated molecular patterns across their cell surface. In particular, two members of the C-type lectin family of proteins, DC-SIGN and CD206, are expressed in microdomains on the plasma membrane and are important receptors for many pathogens including HIV and Candida albicans. The work described in the subsequent chapters uses cutting-edge fluorescence microscopy techniques to characterize the composition, structure, dynamics, and function of single C-type lectin molecules in these domains on the plasma membrane.

The biological relevance of protein and lipid domains in the plasma membrane is discussed in Chapter 2. The work in Chapter 2 is reproduced/adapted with permission from a published article that was a part of the *F1000 series of Biology Reports* (Neumann AK, Itano MS, Jacobson K, 2010**. Understanding lipid rafts and other related membrane domains***, F1000 Biology Reports*, **2**:31. doi: 10.3410/B2-31).

In Chapter 3, the background and methodology specific for the super-resolution method called Blink Microscopy is provided. Chapter 3, a collaboration with investigators at the Technical University of Braunschweig who developed the Blink Microscopy method, will be published as an invited chapter by Methods in Molecular Biology (reproduced/adapted with permission from: Steinhauer C, Itano MS, Tinnefeld P. ***Super-resolution fluorescence imaging with blink microscopy***, new volume entitled "Nanoimaging: Methods and Protocols." Methods in Molecular Biology. USA: Humana Press; 2012, accepted book chapter). Blink Microscopy, which utilizes the successive localization of single molecules, is the predominant method used for the work presented in Chapter 5.

The work presented in Chapter 4 characterizes the composition of C-type lectin microdomains and contrasts the immobility of DC-SIGN and its mutants with a laterally mobile viral envelope protein from influenza. This chapter, conducted in collaboration with Nancy L. Thompson (Dept. of Chemistry, University of North Carolina), presents the results of three complementary modern measurements of the dynamics of proteins on the level of single, living cells and single molecules. To implement two of these methods, work was performed with input from Enrico Gratton (Director of the Laboratory for Fluorescence Dynamics at the University of California-Irvine) on aspects of fluorescence correlation microscopy, and with the Wolfgang Parak laboratory (Marburg University in Marburg, Germany) to generate quantum dots of defined valency. A discussion on how the particular dynamic and composition characteristics of DC-SIGN domains may contribute to the immunological function of these protein domains is also presented. The

work in this chapter is reproduced/adapted with permission from a paper published in the *Biophysical Journal* (Itano MS, Neumann AK, Liu P, Zhang F, Gratton E, Parak WJ, Thompson NL, Jacobson K, 2011. ***Dynamics of DC-SIGN and influenza hemagglutinin in microdomains on plasma membranes***, Biophysical Journal, **100**(11):2662-70. doi: 10.1016/j.bbr.2011.03.031).

The composition, structure, and distribution of CD206 and DC-SIGN C-type lectin domains are investigated using the super-resolution technique Blink Microscopy in Chapter 5. This work was conducted in collaboration with Nancy L. Thompson and investigators in Philip Tinnefeld's lab. The data was collected in Germany, primarily during three separate visits to Munich and Braunschweig for two to three weeks each. Two-color Blink Microscopy was performed to investigate whether two proteins, which appear to be co-localized by using widefield microscopy (with a resolution of ~300 nm), are actually co-localized when viewed at a higher spatial resolution (~30 nm). The work presented in Chapter 5 was reproduced/adapted with permission from a paper published in the *Biophysical Journal* (Itano MS, Steinhauer C, Schmied J, Forthmann C, Liu P, Neumann AK, Thompson NL, Tinnefeld P, Jacobson K, 2012. ***Super-resolution imaging of C-type lectin and influenza hemagglutinin nanodomains on plasma membranes using Blink Microscopy***, Biophysical Journal, **102**(7):1534-42. doi: 1.1016/j.bpj.2012.02.022).

In Chapter 6, the conclusions generated from the work presented in this dissertation are discussed. An outlook on how these conclusions affect the current understanding how proteins are organized on the plasma membrane is also provided.

CHAPTER 2

Understanding Lipid Rafts and Other Related Membrane Domains[1]

2.1 SUMMARY

Evidence in support of the classical lipid raft hypothesis has remained elusive. Data suggests that transmembrane proteins and the actin-containing cortical cytoskeleton can organize lipids into short-lived nanoscale assemblies that can be assembled into larger domains under certain conditions. This supports an evolving view in which interactions between lipids, cholesterol, and proteins create and maintain lateral heterogeneity in the cell membrane.

[1] Reproduced/apdapted with permission from:
Neumann AK, Itano MS, Jacobson K, 2010**. Understanding lipid rafts and other related membrane domains***, F1000 Biology Reports*, **2**:31. doi: 10.3410/B2-31

Michelle S. Itano primarily contributed to writing the "Major recent advances" portion of this manuscript and also contributed to the overall organization, writing, and editing of this manuscript, including figure preparation.

2.2 INTRODUCTION AND CONTEXT

Differential lipid composition between the apical and basolateral membrane domains of epithelial cell plasma membranes [1, 2] made it clear that membrane lipids are not laterally distributed in a homogeneous fashion. The lipid raft hypothesis was developed to explain lateral separation of bilayer lipids, and this idea quickly found applications in viral budding, endocytosis and signal transduction (reviewed in [3]). In model membranes, lipids can separate into microscopically resolvable raft-like domains [4]. Plasma membrane surrogates formed by chemical membrane blebbing or cell swelling procedures also show phase behavior [5-8]. Similar domains are not evident upon direct observation of unperturbed plasma membranes in living cells, but the non-equilibrium nature of cell membranes, including endocytosis, exocytosis, and other motile processes, may prevent overt phase separation. Likewise, quantitative analysis of lipid-anchored protein and lipid diffusion in cell membranes by fluorescence recovery after photobleaching (FRAP), Förster resonance energy transfer (FRET), and fluorescence correlation spectroscopy (FCS) [9-11] indicated that rafts in the plasma membrane of resting cells must be very small or ephemeral (or both), forcing an evolution of the lipid raft hypothesis. These tiny clusters do not represent lipid phase separations but are probably short-range ordering imposed upon lipids by transmembrane proteins and cortical actin structures. Thus, the current challenge for the field is to understand the interplay between protein and lipid that converts the exceedingly small, unstable clusters of components into larger, more stable membrane microdomains required for function [3, 12].

2.3 MAJOR RECENT ADVANCES

The recent development of sensitive quantitative microscopy methods has advanced our knowledge of lipid dynamics in resting cells. The diffusion of raft lipids (e.g., sphingomyelin) and non-raft lipids (e.g., phosphatidylethanolamine) was measured by an elegant FCS technique within regions as small as 30 nm in diameter using stimulation emission depletion fluorescence microscopy. The results indicate that raft lipids, but not non-raft lipids, are indeed preferentially trapped, albeit for short distances (<20 nm) and for short periods (10-20 ms) [13]. HomoFRET measurements, combining FRAP, emission anisotropy, and theoretical model fitting to test models of lateral organization in the membrane, were used to determine the degree of clustering of glycosylphosphatidylinositol (GPI)-anchored proteins in the plasma membrane [14, 15]. The formation of GPI-anchored protein nanoclusters (of ~4 molecules or even less) [14] is an active process involving both actin and myosin, and these nanoclusters are non-randomly distributed into larger domains of <450 nm [15]. Additionally, high-speed single-particle tracking (50 kHz) revealed that GPI-anchored proteins, along with other membrane proteins, undergo rapid hop diffusion between 40 nm actin-regulated compartments, with a compartment dwell time of 1-3 ms on average [16]. However, when GPI-anchored proteins were deliberately cross-linked by gold or quantum dot particles, they underwent transient confinement or 'STALL' (stimulation-induced temporary arrest of lateral diffusion) from a cholesterol-dependent nanodomain in a Src family kinase mediated manner [17-19]. A recent study identified a transmembrane protein (carboxyl-terminal Src kinase [Csk]-binding protein) involved in the linkage

between the particle-cross-linked GPI-anchored protein, Thy1, and the cytoskeleton (Figure 2.1) [20].

Larger microdomains involve raft lipids and specific membrane proteins. The lipid envelopes of influenza and HIV virions, but not those of the vesicular stomatitis virus (VSV) or Semliki Forest virus (SFV), are enriched in raft-like lipids, leading to the notion that these viruses bud from lipid microdomains in the plasma membrane [21-25]. By contrast, the lipidomes of VSV and SFV are very similar to each other and to that of the plasma membrane suggesting that these viruses do not select or generate lipid raft domains for budding [25].

The protein and lipid environment of the budding domains of hemagglutinin (HA) and HIV has been the source of several recent papers examining the process of viral budding using quantitative live-cell imaging techniques. Influenza buds from HA clusters (ranging up to micrometers in diameter) [26] regulated by the HA transmembrane region length and palmitoylation [27]. Recent fluorescence lifetime imaging microscopy (FLIM)-FRET experiments in living cells indicate that HA co-localizes with lipid microdomain markers, further supporting the role of lipid-protein interactions in influenza virus budding [28, 29]. Proton magic angle spinning nuclear magnetic resonance was used to detect a minor fraction (~10-15 %) of liquid-ordered membrane phospholipids in HA virions and virion lipid extracts at 37°C. While lipid ordering increased at lower temperatures it was not required for virion fusion with target membranes [30].

Progressive recruitment of cytoplasmic HIV-1 Gag to the membrane, via posttranslational acyl lipid modification and PIP_2/basic residue interactions, forms membrane domains that culminate in virion budding [31-33]. While the HIV-1 lipid envelope composition indicates enrichment in lipids and proteins associated with 'rafts' [21], paradoxically, one group failed to observe an enrichment of enhanced green fluorescent protein (EGFP)-GPI at Gag domains in living cells [32], suggesting that the local lipid microenvironment may not exactly parallel the classic raft lipid composition. Recent work has implicated the tetraspanin family of proteins in Gag domain formation and function. Tetraspanins, a widely expressed and highly conserved class of transmembrane proteins (reviewed in [34]), form tetraspanin-enriched microdomains (TEMs) through lateral tetraspanin-tetraspanin interactions and binding to non-tetraspanin membrane proteins. HIV-1 Gag is targeted to TEMs and virus buds from these domains [35, 36]. Tetraspanins can be palmitoylated [37] and the lipid environment within TEMs contains cholesterol, but GPI-anchored proteins and caveolin are not enriched in TEMs (reviewed in [38]). Recently, cholesterol and tetraspanin palmitoylation were implicated in the confined diffusion and co-diffusion (of two tetraspanin molecules) of the tetraspanin CD9 [39]. Tetraspanins appear to induce order in the plasma membrane by virtue of protein clustering, but they likely also stabilize lipid microenvironments in the plasma membrane allowing for lateral organization of HIV-1 Gag and virion budding.

Some lectin-based membrane domains form in the absence of posttranslational lipid modifications or known lipid binding activity. Dendritic cell-specific intracellular

adhesion molecule-3-grabbing non-integrin (DC-SIGN), a tetrameric C-type lectin with affinity for high-mannose glycans, forms microdomains on the plasma membrane [40-42] that serve as high-avidity binding sites for numerous pathogens. A previous report suggested that DC-SIGN interacts with lipid rafts [40], but this was based on detergent insolubility and cholera toxin co-localization assays, which generally do not faithfully report on intrinsic membrane lateral heterogeneity. Also, DC-SIGN domains do not depend on cholesterol (unpublished data). Surprisingly, DC-SIGN domains do not recover following photobleaching [42]. This result implies that DC-SIGN within domains does not exchange with the surrounding membrane. The source of this stability remains a mystery, and its cause may not reside in the membrane-apposed cytoskeleton but in extracellular cross-linking factors such as galectins (reviewed in [43]). DC-SIGN membrane domains that are multiplexed with another C-type lectin, CD206 (unpublished data), appear to mediate the formation of fungipods, novel cellular protrusive structures involved in fungal recognition by dendritic cells (Figure 2.2) [44]. Thus, the lateral heterogeneity in membranes provided by rafts and other microdomains continues to provide surprising functional consequences.

2.4 FUTURE DIRECTIONS

A variety of membrane domain forming systems have a wide gamut of lipid and protein constituents and possess a correspondingly broad range of functions. Recent advances have shown that preferential lipid trapping or confinement in the resting plasma membrane occurs only on very small spatiotemporal scales. Critical attention must be

paid when determining if and when such confinement becomes biologically meaningful for processes such as endocytosis and signal transduction. While lipid ordering can be stabilized by oligomerization of membrane-associated proteins (i.e., GM1 crosslinking, influenza HA clustering), the lipids in these domains may still exchange between domain and surrounding membranes, making even these stabilized raft-like domains dynamic environments. At what point does a membrane domain become stable enough to be biologically relevant? What is the range of protein and lipid turnover rates seen in membrane domains and are there different turnover rates for each constituent? It is likely that a spectrum of membrane microdomains exists with different compositions and physical characteristics suited to their diverse purposes. The lipid species and their ordering within raft-like complexes appear to be key factors in determining intradomain cohesiveness and resultant domain size and lifetime.

2.5 CREDITS

This work was supported by National Institutes of Health Grant GM 41402 and the Cell Migration Consortium Grant GM 064346.

2.6 FIGURE LEGENDS

Figure 2.1. EBP50-ERM assembly is the common adaptor complex for linking cholesterol-dependent Thy-1 clusters to the membrane apposed cytoskeleton. The GPI-anchored protein Thy-1 engages membrane lipids and proteins for transmembrane signaling. Thy-1 crosslinking by streptavidin-coated quantum dots aggregates GPI lipid tails in the outer leaflet of the plasma membrane in a cholesterol-dependent manner. Carboxyl-terminal Src kinase (Csk)-binding protein (CBP), a transmembrane protein, is recruited to or captured by Thy-1 clusters along with Src-family kinase substrates (KS). CBP or KS (or both) are phosphorylated by Src-family kinases (SFK), enabling CBP to bind to actin filaments via an EBP50-ERM (Ezrin-binding phosphoprotein 50-ezrin/radixin/moesin) adaptor linkage resulting in a transient anchorage. When either CBP or the adaptors are dephosphorylated by an unspecified protein tyrosine phosphatase (PTP), the anchorage is terminated. Image was reproduced/adapted with permission from [20]; Chen *et al*., *J Cell Sci* 2009, doi: 10.1242/jcs.049346.

Figure 2.2. C-type lectin domains and fungipod formation. C-type lectins (CLRs) form a type of plasma membrane domain that is not dependent on cholesterol. (*A*) Plasma membrane domains containing mixtures (yellow) of dendritic cell-specific intracellular adhesion molecule-3-grabbing non-integrin (DC-SIGN) (green) and CD206 (red) are observed on a monocyte-derived dendritic cell (DC) by immunofluorescence. DC-SIGN domains are known sites of binding and entry for a range of pathogens including HIV-1. (*B*) Yeast cell wall material is sensed by these CLR membrane domains, triggering a unique protrusive response, the fungipod. The image shows an example of a DC fungipod

formed via CD206 ligation by a fixed *Saccharomyces cerevisiae* particle (zymosan), visualized by scanning electron microscopy (9500×). Figure 2.2b was reproduced/adapted with permission from [44], Neumann & Jacobson, *PLoS Pathog* 2010, doi:10.1371/journal.ppat.1000760.

FIGURE 2.1

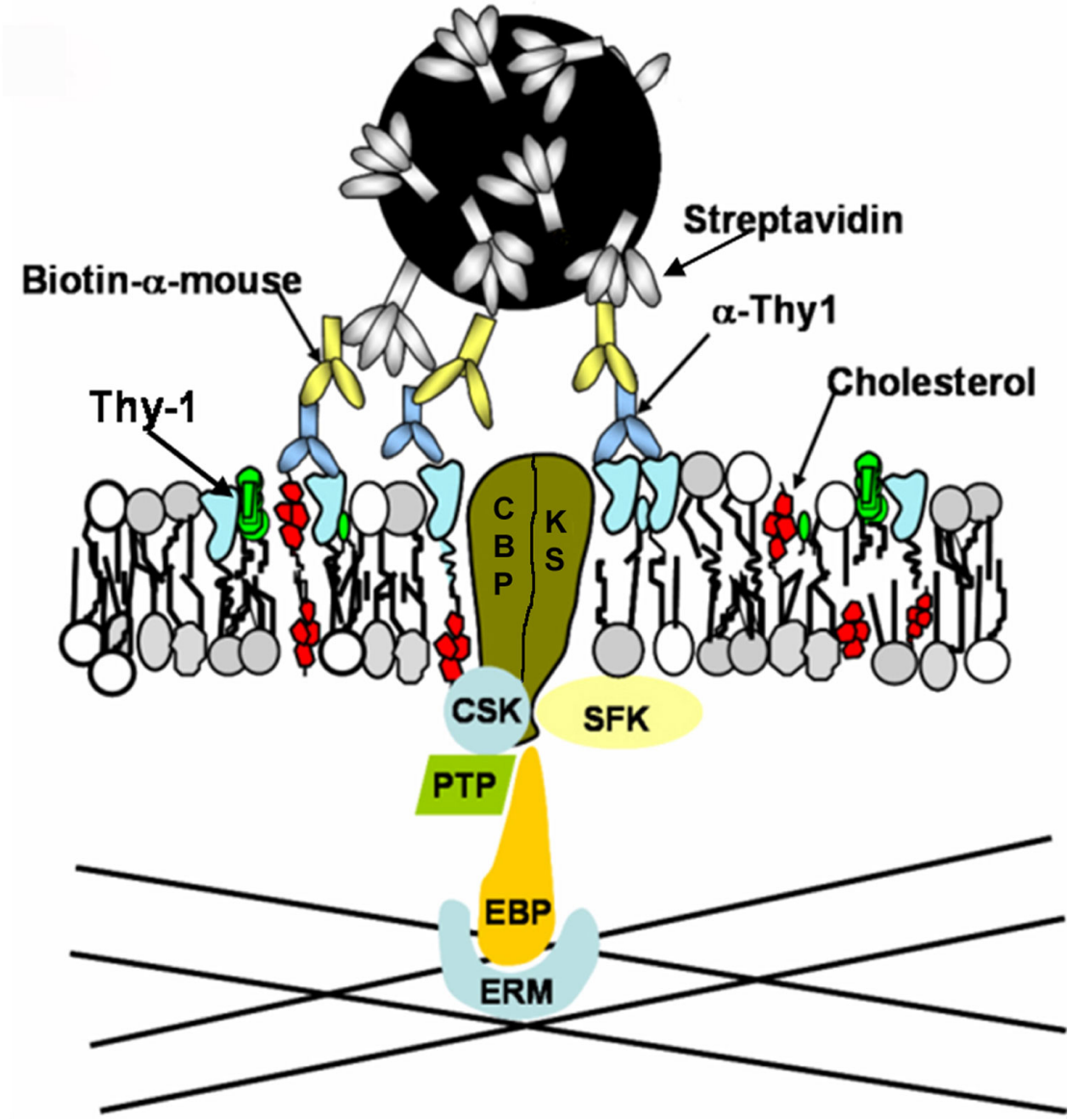
Streptavidin
Biotin-α-mouse
α-Thy1
Thy-1
Cholesterol
CBP
KS
CSK
SFK
PTP
EBP
ERM

FIGURE 2.2

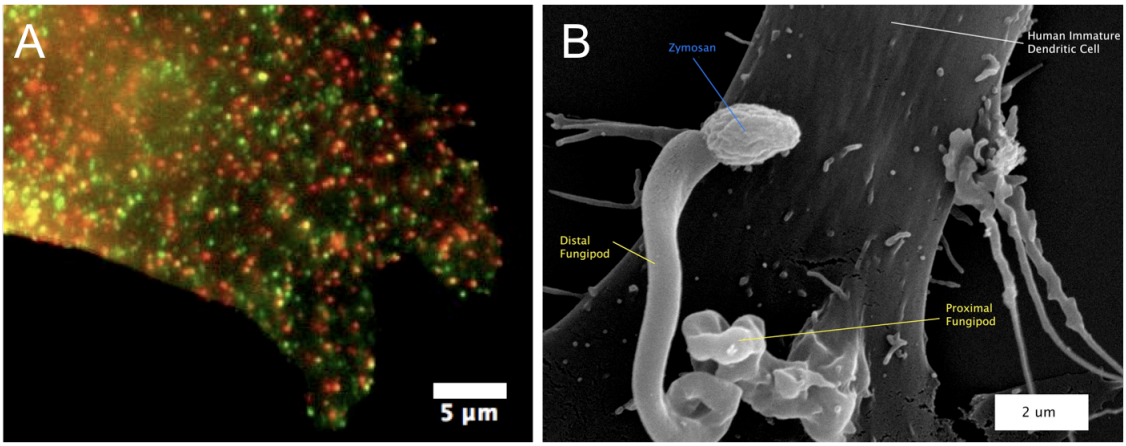
A
5 µm
B
Zymosan
Human Immature
Dendritic Cell
Distal
Fungipod
Proximal
Fungipod
2 um

2.7 REFERENCES

1. Kawai, K., M. Fujita, and M. Nakao. 1974. Lipid components of two different regions of an intestinal epithelial cell membrane of mouse. Biochim Biophys Acta 369:222-233.

2. van Meer, G., and K. Simons. 1982. Viruses budding from either the apical or the basolateral plasma membrane domain of MDCK cells have unique phospholipid compositions. EMBO J 1:847-852.

3. Lingwood, D., and K. Simons. 2010. Lipid rafts as a membrane-organizing principle. Science 327:46-50.

4. Dietrich, C., L. A. Bagatolli, Z. N. Volovyk, N. L. Thompson, M. Levi, K. Jacobson, and E. Gratton. 2001. Lipid rafts reconstituted in model membranes. Biophys J 80:1417-1428.

5. Veatch, S. L., P. Cicuta, P. Sengupta, A. Honerkamp-Smith, D. Holowka, and B. Baird. 2008. Critical fluctuations in plasma membrane vesicles. ACS Chem Biol 3:287-293.

6. Baumgart, T., A. T. Hammond, P. Sengupta, S. T. Hess, D. A. Holowka, B. A. Baird, and W. W. Webb. 2007. Large-scale fluid/fluid phase separation of proteins and lipids in giant plasma membrane vesicles. Proc Natl Acad Sci U S A 104:3165-3170.

7. Sengupta, P., A. Hammond, D. Holowka, and B. Baird. 2008. Structural determinants for partitioning of lipids and proteins between coexisting fluid phases in giant plasma membrane vesicles. Biochim Biophys Acta 1778:20-32.

8. Lingwood, D., J. Ries, P. Schwille, and K. Simons. 2008. Plasma membranes are poised for activation of raft phase coalescence at physiological temperature. Proc Natl Acad Sci U S A 105:10005-10010.

9. Kenworthy, A. K., B. J. Nichols, C. L. Remmert, G. M. Hendrix, M. Kumar, J. Zimmerberg, and J. Lippincott-Schwartz. 2004. Dynamics of putative raft-associated proteins at the cell surface. The Journal of Cell Biology 165:735-746.

10. Glebov, O. O., and B. J. Nichols. 2004. Lipid raft proteins have a random distribution during localized activation of the T-cell receptor. Nat Cell Biol 6:238-243.

11. Lenne, P. F., L. Wawrezinieck, F. Conchonaud, O. Wurtz, A. Boned, X. J. Guo, H. Rigneault, H. T. He, and D. Marguet. 2006. Dynamic molecular confinement

in the plasma membrane by microdomains and the cytoskeleton meshwork. EMBO J 25:3245-3256.

12. Jacobson, K., O. G. Mouritsen, and R. G. Anderson. 2007. Lipid rafts: at a crossroad between cell biology and physics. Nat Cell Biol 9:7-14.

13. Eggeling, C., C. Ringemann, R. Medda, G. Schwarzmann, K. Sandhoff, S. Polyakova, V. N. Belov, B. Hein, C. von Middendorff, A. Schonle, and S. W. Hell. 2009. Direct observation of the nanoscale dynamics of membrane lipids in a living cell. Nature 457:1159-1162.

14. Sharma, P., R. Varma, R. C. Sarasij, Ira, K. Gousset, G. Krishnamoorthy, M. Rao, and S. Mayor. 2004. Nanoscale organization of multiple GPI-anchored proteins in living cell membranes. Cell 116:577-589.

15. Goswami, D., K. Gowrishankar, S. Bilgrami, S. Ghosh, R. Raghupathy, R. Chadda, R. Vishwakarma, M. Rao, and S. Mayor. 2008. Nanoclusters of GPI-anchored proteins are formed by cortical actin-driven activity. Cell 135:1085-1097.

16. Umemura, Y. M., M. Vrljic, S. Y. Nishimura, T. K. Fujiwara, K. G. Suzuki, and A. Kusumi. 2008. Both MHC class II and its GPI-anchored form undergo hop diffusion as observed by single-molecule tracking. Biophys J 95:435-450.

17. Chen, Y., W. R. Thelin, B. Yang, S. L. Milgram, and K. Jacobson. 2006. Transient anchorage of cross-linked glycosyl-phosphatidylinositol-anchored proteins depends on cholesterol, Src family kinases, caveolin, and phosphoinositides. J Cell Biol 175:169-178.

18. Suzuki, K. G., T. K. Fujiwara, F. Sanematsu, R. Iino, M. Edidin, and A. Kusumi. 2007. GPI-anchored receptor clusters transiently recruit Lyn and G alpha for temporary cluster immobilization and Lyn activation: single-molecule tracking study 1. J Cell Biol 177:717-730.

19. Suzuki, K. G., T. K. Fujiwara, M. Edidin, and A. Kusumi. 2007. Dynamic recruitment of phospholipase C gamma at transiently immobilized GPI-anchored receptor clusters induces IP3-Ca2+ signaling: single-molecule tracking study 2. J Cell Biol 177:731-742.

20. Chen, Y., L. Veracini, C. Benistant, and K. Jacobson. 2009. The transmembrane protein CBP plays a role in transiently anchoring small clusters of Thy-1, a GPI-anchored protein, to the cytoskeleton. J Cell Sci 122:3966-3972.

21. Nguyen, D. H., and J. E. Hildreth. 2000. Evidence for budding of human immunodeficiency virus type 1 selectively from glycolipid-enriched membrane lipid rafts. J Virol 74:3264-3272.

22. Aloia, R. C., H. Tian, and F. C. Jensen. 1993. Lipid composition and fluidity of the human immunodeficiency virus envelope and host cell plasma membranes. Proc Natl Acad Sci U S A 90:5181-5185.

23. Scheiffele, P., A. Rietveld, T. Wilk, and K. Simons. 1999. Influenza viruses select ordered lipid domains during budding from the plasma membrane. J Biol Chem 274:2038-2044.

24. Brugger, B., B. Glass, P. Haberkant, I. Leibrecht, F. T. Wieland, and H. G. Krausslich. 2006. The HIV lipidome: a raft with an unusual composition. Proc Natl Acad Sci U S A 103:2641-2646.

25. Kalvodova, L., J. L. Sampaio, S. Cordo, C. S. Ejsing, A. Shevchenko, and K. Simons. 2009. The lipidomes of vesicular stomatitis virus, semliki forest virus, and the host plasma membrane analyzed by quantitative shotgun mass spectrometry. J Virol 83:7996-8003.

26. Hess, S. T., T. J. Gould, M. V. Gudheti, S. A. Maas, K. D. Mills, and J. Zimmerberg. 2007. Dynamic clustered distribution of hemagglutinin resolved at 40 nm in living cell membranes discriminates between raft theories. Proceedings of the National Academy of Sciences of the United States of America 104:17370-17375.

27. Takeda, M., G. P. Leser, C. J. Russell, and R. A. Lamb. 2003. Influenza virus hemagglutinin concentrates in lipid raft microdomains for efficient viral fusion. Proceedings of the National Academy of Sciences of the United States of America 100:14610-14617.

28. Engel, S., S. Scolari, B. Thaa, N. Krebs, T. Korte, A. Herrmann, and M. Veit. 2010. FLIM-FRET and FRAP reveal association of influenza virus haemagglutinin with membrane rafts. Biochem J 425:567-573.

29. Scolari, S., S. Engel, N. Krebs, A. P. Plazzo, R. F. De Almeida, M. Prieto, M. Veit, and A. Herrmann. 2009. Lateral distribution of the transmembrane domain of influenza virus hemagglutinin revealed by time-resolved fluorescence imaging. J Biol Chem 284:15708-15716.

30. Polozov, I. V., L. Bezrukov, K. Gawrisch, and J. Zimmerberg. 2008. Progressive ordering with decreasing temperature of the phospholipids of influenza virus. Nat Chem Biol 4:248-255.

31. Jouvenet, N., P. D. Bieniasz, and S. M. Simon. 2008. Imaging the biogenesis of individual HIV-1 virions in live cells. Nature 454:236-240.

32. Ivanchenko, S., W. J. Godinez, M. Lampe, H. G. Krausslich, R. Eils, K. Rohr, C. Brauchle, B. Muller, and D. C. Lamb. 2009. Dynamics of HIV-1 assembly and release. PLoS Pathog 5:e1000652.

33. Saad, J. S., J. Miller, J. Tai, A. Kim, R. H. Ghanam, and M. F. Summers. 2006. Structural basis for targeting HIV-1 Gag proteins to the plasma membrane for virus assembly. Proc Natl Acad Sci U S A 103:11364-11369.

34. Hemler, M. E. 2005. Tetraspanin functions and associated microdomains. Nat Rev Mol Cell Biol 6:801-811.

35. Nydegger, S., S. Khurana, D. N. Krementsov, M. Foti, and M. Thali. 2006. Mapping of tetraspanin-enriched microdomains that can function as gateways for HIV-1. J Cell Biol 173:795-807.

36. Jolly, C., and Q. J. Sattentau. 2007. Human immunodeficiency virus type 1 assembly, budding, and cell-cell spread in T cells take place in tetraspanin-enriched plasma membrane domains. J Virol 81:7873-7884.

37. Claas, C., C. S. Stipp, and M. E. Hemler. 2001. Evaluation of prototype transmembrane 4 superfamily protein complexes and their relation to lipid rafts. J Biol Chem 276:7974-7984.

38. Le Naour, F., M. Andre, C. Boucheix, and E. Rubinstein. 2006. Membrane microdomains and proteomics: lessons from tetraspanin microdomains and comparison with lipid rafts. Proteomics 6:6447-6454.

39. Espenel, C., E. Margeat, P. Dosset, C. Arduise, C. Le Grimellec, C. A. Royer, C. Boucheix, E. Rubinstein, and P. E. Milhiet. 2008. Single-molecule analysis of CD9 dynamics and partitioning reveals multiple modes of interaction in the tetraspanin web. J Cell Biol 182:765-776.

40. Cambi, A., F. de Lange, N. M. van Maarseveen, M. Nijhuis, B. Joosten, E. M. van Dijk, B. I. de Bakker, J. A. Fransen, P. H. Bovee-Geurts, F. N. van Leeuwen, N. F. Van Hulst, and C. G. Figdor. 2004. Microdomains of the C-type lectin DC-SIGN are portals for virus entry into dendritic cells. J Cell Biol 164:145-155.

41. Koopman, M., A. Cambi, B. I. de Bakker, B. Joosten, C. G. Figdor, N. F. van Hulst, and M. F. Garcia-Parajo. 2004. Near-field scanning optical microscopy in liquid for high resolution single molecule detection on dendritic cells. FEBS Letters 573:6-10.

42. Neumann, A. K., N. L. Thompson, and K. Jacobson. 2008. Distribution and lateral mobility of DC-SIGN on immature dendritic cells--implications for pathogen uptake. J Cell Sci 121:634-643.

43. Grigorian, A., S. Torossian, and M. Demetriou. 2009. T-cell growth, cell surface organization, and the galectin-glycoprotein lattice. Immunol Rev 230:232-246.

44. Neumann, A. K., and K. Jacobson. 2010. A novel pseudopodial component of the dendritic cell anti-fungal response: the fungipod. PLoS Pathog 6:e1000760.

CHAPTER 3

Super-Resolution Fluorescence Imaging with Blink Microscopy[1]

3.1 SUMMARY

Recently, a new approach for super-resolution microscopy has emerged which is based on the successive localization of single molecules. The majority of molecules are prepared to reside in a non-fluorescent dark state, leaving only a few single molecules fluorescing. The single molecules can subsequently be localized on the camera image. Successive localization of all molecules allows reconstruction of a super-resolved image of the labeled structure. A variety of ways for limiting the number of locatable molecules have been developed recently which expand this current field of imaging. Here we describe a super-resolution microscopy method that employs the use of reversible, generic dark states, for example radical ion states. This method requires only a single laser source and can be carried out with many fluorescent dyes, and in some cases even in living cells. We provide a step-by-step procedure for this method, which we have called Blink Microscopy.

---

[1] Reproduced/adapted with permission from:
Steinhauer C, Itano MS, Tinnefeld P. ***Super-resolution fluorescence imaging with blink microscopy***, new volume entitled "Nanoimaging: Methods and Protocols." Methods in Molecular Biology. USA: Humana Press; 2012, accepted book chapter.

Michelle S. Itano primarily contributed to writing the “Sample Preparation” and “Post-Processing” sections, providing the data for Figure 3.3, and also contributed to the overall organization, writing and editing of this manuscript.

3.2 INTRODUCTION

Since the publication of STORM and (F)PALM in 2006 [1-3] several similar approaches have been developed based on the wide-field detection and localization of single molecules [4-14]. These approaches mainly differ from each other in the way that single molecule fluorescence events are generated. Generally, this is achieved by affecting how the majority of fluorophores are prepared to reside in a non-fluorescent state while a small subset emits, resulting in point-spread functions originating from single molecules. An overview of different methods can be found in review articles in various journals [15-20].

This chapter focuses on, and describes in detail, the unique features of Blink Microscopy. Blink Microscopy employs single-molecule blinking, a well-known feature of organic fluorophores, to cycle dyes between a fluorescent ON-state and a non-fluorescent OFF-state.

With the exception of stimulated emission depletion microscopy (STED) and other realizations of the RESOLFT (REversible Saturatable OpticaL Fluorescence Transitions) concept [17], many emerging super-resolution (SR) imaging methods are based on the successive localization of single molecules [1, 2]. In these methods, the majority of molecules are prepared to reside in a non-fluorescent dark state, leaving only a few single molecules fluorescing. These single molecules are subsequently localized by fitting a two-dimensional Gaussian function to the point spread functions (PSFs) of their

fluorescence intensities. This temporal separation of fluorescence is the most crucial step in localization-based microscopy; how to achieve this separation using organic fluorophores is a major focus of the following sections. The super-resolved image is then reconstructed from all single-molecule localizations. An example of Blink Microscopy data is shown in Figure 3.1.

Interestingly, both STED/RESOLFT and localization-based approaches can use the same types of organic fluorophores, although the photophysical requirements for the fluorophores are considerably different. Both approaches require very photostable fluorophores that can be switched between an ON- and an OFF-state [16, 17]. One exemplary method exploits generic dark states (e.g. radical anion states) of the fluorophores in order to switch the major fraction of molecules OFF, so that the remaining subpopulation of molecules can be precisely localized. In this method, fluorescent dyes are switched OFF by transiently accepting an electron from a reductant molecule, which then yields dark states of up to several hundred seconds (Figure 3.2 *A*) [6, 21, 22]. Such dark states appear as blinking in single-molecule intensity transients (see Figure 3.2 *B*). Therefore, this technique has been termed “Blink Microscopy”.

To rationalize the blinking, we take a brief look at the thermodynamics of photoinduced electron transfer reactions. Following excitation, the fluorescent dye is shelved from the ground state, S0, to the first excited single state, S1. In other words, the dye has entered a state of higher energy. In this state, the dye is a better electron acceptor than it was when it was in the ground state because the highest occupied molecular

orbital of the molecule is only singly occupied, and can therefore accept an electron quite easily. When a putative electron donor such as ascorbic acid or a thiolate ion collides with a dye in the excited singlet or triplet state, electron transfer to the dye can occur. The lifetime of the radical anion (for a dye molecule with an assumed neutral ground state) depends on the stability of the radical anion and the concentration of potential electron acceptors, such as oxygen. Thus, the lifetime can be controlled in vitro by adapting the oxidant (e.g. the oxygen) concentration. For in vivo measurements, certain dyes that show sufficiently long OFF-state lifetimes in physiological oxygen concentrations have to be used. Due to their high reduction potentials, examples of suitable dyes include the oxazines ATTO655, ATTO680, and ATTO700 [16, 22].

Long OFF-states are of profound importance for super-resolution microscopy methods that utilize successive single-molecule localizations. The OFF-state lifetime and the time it takes to read out the photons emitted during one ON-state are crucial parameters affecting the obtainable resolution. More molecules can be registered for an area of the size of the point-spread function when the ratio of OFF- to ON- times is large. This requires the use of dyes with long OFF-states, comparably strong lasers, and fast cameras to enable fast readouts [16].

Belonging to the class of techniques that employ successive single-molecule localizations, Blink Microscopy distinguishes itself by working with common organic dyes and requiring only one laser (for each color, in multi-color applications). In addition, Blink Microscopy can work in the presence of oxygen, and offers a rather broad range of

possible buffer conditions that are close to physiological. Blink Microscopy has been used to study cytoskeletal structures, such as actin filaments in fixed cells, amyloid aggregates, DNA nanostructures, and single-molecule assembled structures [6, 22-25]. In parallel, very similar techniques have been developed by the Sauer and the Hell laboratories, which have been termed dSTORM and GSDIM [5, 7, 26], respectively, showing that single-molecule blinking can even be applied in living cells [27, 28].

In this article, we provide a detailed protocol for Blink Microscopy, including the microscope setup, chemical and sample preparation, measurement procedures, and issues to consider for data analysis and trouble-shooting. The method is exemplarily demonstrated by imaging DC-SIGN, a transmembrane lectin that forms domains on the membrane of dendritic cells. These domains are commonly too small to be resolved by conventional fluorescence microscopy [29].

3.3 MATERIALS

3.3.1 Chemicals and Consumables

1. MilliQ water
2. PBS, pH 7.4, preferentially as tablets to dissolve in water
3. Ascorbic acid (AA)
4. Methyl viologen (MV)
5. Mercaptoethylamine (MEA)
6. Beta-mercaptoethanol (ME)

7. TCEP (Sigma 646547)
8. Tris
9. Catalase (Sigma C 100-50 mg)
10. Glucose oxidase (Sigma G2133-50KU)
11. Glucose
12. Glycerol 86 %
13. LabTek chambered coverglasses (Nunc 155411)
14. 96-well Plate sealing sheets
15. 16 % Para-formaldehyde (PFA) stock solution
16. Primary antibody corresponding to a protein of interest
17. Secondary antibody, preferably unlabeled Fab_2 fragments
18. Amine reactive dye, e.g. ATTO655 NHS-ester. Dissolve in DMF, make 0.1 mg aliquots and dry in a speed-vac. Store at -20 °C.
19. Oxygen scavenging stock solution (20×): 5 mL 100 mM Tris-HCl, 25 mM KCl, pH 7.5; 5 mL Glycerol (86 %); 40 µl TCEP (0.5 M); 40 µl Catalase (20 mg/mL as supplied); 10 mg Glucose oxidase. Store in working aliquots at -20 °C. Due to its negligible influence on dye photophysics, TCEP is used instead of DTT.
20. NAP-5 Columns (GE Healthcare)
21. NanoRuler calibration standards to test sub-diffraction resolution (www.sts-nano.com)

3.3.2 Microscope

1. Leica SR-GSD, Zeiss Elyra PAL-M or Nikon nSTORM commercial microscope system
2. Appropriate excitation laser with at least 100 mW output power
3. High-quality emission and excitation filters
4. High numerical aperture (≥1.4) oil-immersion objective with 60× or 100× magnification
5. Back-illuminated EMCCD-camera
6. Stage micrometer for pixel size calibration

3.4 METHODS

3.4.1 Sample Preparation

Cells

Cells are grown in standard media and at recommended conditions. Growing the cells on LabTek chambered coverglass slides offers the advantages that they can easily be transferred to the microscope, buffers can be changed easily, and chambers can be sealed for oxygen removal. When using other non-glass cell culture slides, the oxygen permeability of some plastics should be considered.

Detailed conditions for the proper growth and fixation of cells depend strongly on the type of cells used and the molecule being imaged, and are not

described here. However, it is important to note that fixation chemicals may have an influence on dye photophysics. In addition, fixation methods, especially those which use hardening media, might alter the shape of the structures of interest. Dehydrating formulas, for example, tend to flatten cells and change the appearance of the nucleus [30]. Therefore, if Blink Microscopy is unsuccessful or yields unexpected results, you may want to consider using alternate methods for fixation. Correspondingly, we recommend keeping the samples in buffer, if possible. Another benefit of keeping cells in buffer is that it allows for simple and fast tuning of the ON- and OFF-times by changing the reductant and oxidant concentrations in the buffer solution.

Fluorophores

It is as important to choose an appropriate fluorophore and appropriate imaging and staining conditions, as it is to use a highly sensitive microscope. There are many options available in regards to choosing an appropriate fluorophore to use for imaging, but in general, commercially-available dyes (e.g. ATTO dyes) work well for use with Blink Microscopy.

Antibody Labeling

As with other immunofluorescence-based labeling methods, a primary antibody must be carefully chosen to ensure both reliable specificity and affinity for the desired target molecule. It is best to directly label the primary antibody with the fluorophore, as this will lead to both less spatial distance between the

molecule of interest and the dye, and a simpler estimation of the number of dyes per target protein. Alternatively, if labeling the primary antibody is either technically difficult or results in altered binding to the target protein, sequential immuno-labeling with an unlabeled primary antibody and a labeled secondary antibody can be employed. Keep in mind, however, that this antibody complex can have a spatial extent of 10-20 nm, which may be a limiting factor when imaging very small structures, for example, quantifying nano-domain sizes.

Good protocols for labeling antibodies with fluorescent dyes are provided by the suppliers of reactive dyes, such as NHS-esters and maleimides. Our standard procedure for labeling with amine-reactive NHS-esters is as follows:

1. Dissolve the protein in PBS at 0.5 – 1 mg/mL.
2. Adjust the pH of a 250 µl antibody solution to be between 8.5 – 9.
3. Dissolve 0.1 mg of dye in 10 µl of DMF, or another water-free solvent.
4. Add 1 – 5 µl of dye solution to the antibody solution. Whole IgG molecules contain more amine groups and require more dye than, for example, Fab_2 fragments.
5. Shake at room temperature for at least three hours.
6. Remove excess dye using a desalting column (e.g. NAP-5, GE Healthcare).
7. Determine the degree-of-labeling by absorption spectroscopy of the filtrate.

For Blink Microscopy, it is best to have a low fluorophore number per target molecule. In part, this reduces the likelihood that more than one dye will be simultaneously emitting within the area of a point-spread function (PSF) of the dye. If more than one dye is emitting within a single PSF it is likely that the dyes will be rejected during image processing steps and not included in the final SR image, or will lead to a wrong localization. Both will worsen the quality of the final SR image. Additionally, more fluorophores within a small area may lead to physical contact between dyes, which can alter their photophysical properties and compromise Blink Microscopy.

Cell Labeling

In order to generate an accurate SR image (without missing information from unlabeled target molecules) or to estimate the number of molecules from a SR image, it is important to label the structure of interest to saturation or as completely as possible. Saturation can be assured by immunostaining samples with increasing concentration of primary antibody (combined with an excess of labeled secondary antibody, for sequential immunostaining experiments). The concentration of the primary antibody should be increased until the fluorescence intensity of the structure, using identical acquisition settings for widefield microscopy, saturates. The lowest antibody concentration that achieves the maximum possible fluorescence intensity is then used for the experiments. For very dense structures, it is possible to label with antibody concentrations below saturation levels in order to achieve single-molecule localization during

acquisition. However, in this instance, it should be noted that the final SR image will not represent the complete structure, so the staining should occur at concentrations as close to saturation as possible. Of course, this labeling characterization only works with primary antibodies with high specificity for their target molecule. If antibodies bind non-specifically, the fluorescence intensity will saturate at much higher concentrations, where the non-specific fluorescence will outshine the actual signal.

Fixation and staining of cells will depend upon the particular cell type and target structure to be studied. Careful attention should be given to the choice and concentration of antibodies. As an example, the procedure for staining transmembrane proteins DC-SIGN and Dectin-1 on human dendritic cells is given:

1. Wash cells 3 × with PBS. Incubate cells in between washes to maintain cell health.
2. Fix with 4 % PFA/PBS, by incubating at room temperature for 20 min. Note that depending on the structure to be visualized, cell permeabilization may be necessary.
3. Wash cells 3 × with PBS. At this stage, cells can be stored in PBS w/ 0.05 % sodium azide at 4 °C for several weeks.
4. Block by incubating 30 min or overnight in PBS + 0.1 % BSA.

5. Stain with 100 µl of the primary antibody for the first protein of interest (in this example, mouse monoclonal IgG2b specific for human protein DC-SIGN) for 20 min at room temperature with a concentration of ≈10 µg/mL in PBS + 0.1 % BSA.
6. Wash cells 3 × with PBS.
7. Add 100 µl of the secondary antibody (in this example, goat anti-mouse ATTO655-Fab) at a concentration of ≈2 µg/mL in PBS w/ 0.1 % BSA. Incubate at room temperature for 15 min in the dark (covered with foil or in a drawer).
8. Wash cells 5 × with PBS.
9. If a second color is required, proceed as described in steps 10-14 below. Otherwise see step 15.
10. Stain with 100 µl of the other primary antibody for the second protein of interest (in this example, goat polyclonal IgG specific for human protein Dectin-1) for 20 min at room temperature with a concentration of ≈10 µg/mL in PBS + 0.1 % BSA.
11. Wash cells 3 × with PBS.
12. Add 100 µl of appropriate secondary antibody for the second protein (in this example, rabbit anti-goat Alexa546). Incubate at room temperature for 15 min in the dark (covered with foil or in a drawer).
13. Wash cells 5 × with PBS.

14. Store cells in 2 mL PBS, at 4 °C, sealed with parafilm and protected from light.
15. Visualize with fluorescence for Blink Microscopy.

3.4.2 Microscope Set-up

A prerequisite for any super-resolution approach that is based on the localization of single molecules is the ability to detect single fluorophores with a good signal-to-noise ratio (SNR). This imposes an upper limit for the resolution that can be achieved for a given dye. It is also important to use a strong laser, combined with a fast camera, which can drastically reduce the image acquisition time and increase the achievable resolution by optimizing the ratio of ON-times to OFF-times.

The task of breaking the diffraction barrier is not trivial and requires attainment of the highest detection efficiency, signal-to-noise ratio and optical resolution. Any trade-offs made regarding the components of the microscope will certainly compromise SR image quality and resolution.

Microscope Body

Any microscope body that has an entrance for a laser light source and side-, front-, or bottom- port to attach an EMCCD camera can be used. An autofocus system is not necessary, however, it may be helpful if longer image acquisition times are required. Manual refocusing during the acquisition of a SR image introduces too many vibrations.

Light Source

Blink Microscopy requires a relatively strong CW laser that has at least 100 mW output power. This intensity is needed in order to drive the fluorophore into its dark radical form within milliseconds of illumination. An even higher-powered laser may be beneficial if the light is coupled into an optical fiber, or if a large sample area is to be illuminated.

Filters and Dichroics

High-end filters and dichroics are essential to obtain a suitable signal-to-noise ratio. For most solid-state laser sources, a clean-up filter is required to block non-peak wavelength light emitted by the laser. The dichroic should be specific for the chosen laser and be able to reflect >90% of the respective wavelength. The emission filter must have an OD = 6 in the range that the clean-up filter has an OD < 3. When multiple lasers are used, care must be taken that each emission filter can completely block each laser. Some filters tend to have low ODs in regions a few hundred nanometers away from their transmission window.

Objective

For sufficient magnification and collection efficiency, high-N.A. objectives with 60× or 100× magnification should be used. A numerical aperture of at least 1.4 is required for objective-based total internal reflection (TIR) microscopy, which offers a much better SNR than conventional widefield microscopy.

CCD-Camera

For the detection of single molecules, each emitted photon is important. So the detection efficiency should be as high as possible. Back-illuminated EMCCD cameras are the most widely used, because they offer a quantum efficiency of >90% between 480 nm and 700 nm. A new generation of CMOS chips can acquire images much faster, but are currently only available in front-illuminated versions that have quantum efficiencies around 50-60%.

Optical Alignment

Beam path optics are provided by the microscope manufacturers. If possible, the illuminated area should be set to an area as small as possible (yet sufficiently large to illuminate the desired field of view) in order to maximize illumination density. Depending on the camera's physical pixel size, additional magnification in the detection path may be used to achieve an image pixel size between 80 nm and 140 nm.

For later analysis it is essential to measure the effective image pixel size for each configuration (objective, additional magnification, and camera). For this purpose, stage micrometers with 10 µm line distances are commercially available.

1. Mount the stage micrometer on the microscope and align it so that the lines appear vertical on the camera.

2. Count the number of lines (n_{lines}) visible on the camera and determine the number of pixels (n_{px}) between the outermost lines.
3. The pixel size in nanometers is: $\frac{n_{lines} \bullet 10{,}000\ nm}{n_{px}}$

3.4.3 Does the Microscope Detect Single Molecules?

Before starting a SR measurement, make sure the microscope is working properly. This can be done by preparing a simple test slide with single fluorophores.

1. Prepare a 5 mg / mL BSA solution.
2. Incubate the BSA solution on a glass slide for 15 minutes.
3. Wash the slide, mount it on the microscope, and add the labeled antibody used for imaging at a concentration of ≈ 10^{-8} M in the BSA solution.
4. Incubate for 5 minutes and wash 2 × with the BSA solution (when imaging with a TIR microscope, the dye solution can remain on the slide, because the solution background should not be visible).
5. Cool the camera to -55 °C, set the EM gain to 250, make sure the optics are set for TIRF illumination, and adjust the laser power to approximately 10 µW/µm².
6. Single molecules should be visible on the glass surface. If too many molecules have bound, repeat with reduced concentration of labeled antibody and/or incubation time. If there are no molecules visible, supplement the BSA solution used in the first step with some primary antibodies that will bind to the labeled secondary antibody.

7. Test for the presence of single molecules by continuously imaging with high laser intensity and observing single-step photobleaching, or count bleaching steps and compare to the expected dye-to-protein ratio calculated according to the degree-of-labeling of the secondary antibody.
8. At this point an *estimate* for the localization precision can be obtained by recording the raw data and analyzing it as if it was actual Blink Microscopy data (see section on **Post-Processing**). The FWHM of the resulting spots in the super-resolution image reflects the expected resolution for the Blink experiment.

3.4.4 Testing the Resolution with NanoRulers

To ensure that the microscope is not only able to detect single molecules, but is also able to perform super-resolution measurements, it is favorable to actually test for the ability to resolve sub-diffraction distances. Since 2011, there are commercially available calibration standards specifically for this purpose (www.sts-nano.com).

The resolution stated in many publications is based on experimental evidence from cellular structures. This approach is certainly not inaccurate, but may be hard to reproduce and depends on how long the researcher is willing to search for "the right structure". This structure consists of two spots or lines at a distance large enough to be resolved and small enough to demonstrate the resolution advantage of using the respective method. A novel approach for creating nanoscale distance standards, based on DNA nanotechnology, can supply the required resolution test sample [24]. Based on the

DNA origami technique [31], fluorophores are placed at specific positions on a 100 x 70 nm grid. Thousands of identical structures, all exhibiting a distance of, 80 nm, for example, can be immobilized on a glass surface and imaged with Blink Microscopy or other complimentary techniques. These standards, named “NanoRulers”, are easy to use without further technical knowledge and provide reliable information on the status of the microscope.

3.4.5 Preparing the Dye to Blink

Depending on the fluorophore used, slightly different procedures are required to make the fluorophores blink in the right way for Blink Microscopy. Some exemplary procedures are listed below. They should be considered examples to act as a starting point for optimizing the respective conditions for each cell type and protein of interest. Details on how to fine-tune these conditions can be found in the section on **Finding the Right Blink Parameters**.

Cyanine Dyes (e.g. Cy3b and Cy5 [6])

Cy5 is widely used in fluorescence imaging. Previous SR imaging techniques like STORM [2] and dSTORM [8] were first demonstrated with this fluorophore, but rely on a different mechanism [32, 33]. The mechanism of Blink Microscopy requires the fluorophore to be reduced from an excited state, forming a radical anion. As in STORM and dSTORM, oxygen must be removed, as it acts as a triplet quencher and oxidant. This can easily be done enzymatically as described in the literature [34, 35]. Also, the absence of oxygen drastically increases the photostability of the dye.

1. Prepare an AA working solution by diluting the 100 mM stock 1:10 in PBS.
2. Fill 95 % of the LabTek chamber, containing cells that have been stained (as in the section on **Cell Labeling**), with PBS containing 1 % glucose (➔700 µl).
3. Add 7 µl of AA working solution.
4. Add 35 µl of oxygen scavenging solution, which should completely fill the chamber.
5. Mix quickly (by pipetting up and down) and seal chamber using sealing sheets.
6. Wait approx. 5 – 10 minutes, until oxygen is removed (see **Notes 2** and **3**).

Oxazine Dyes (e.g. ATTO655 [22])

Due to the relatively low energy level of the radical anion of ATTO655, its reduced state is remarkably stable, even in the presence of oxygen. Because of this, oxygen removal is not required to obtain sufficiently long OFF-times for Blink Microscopy. To prevent photobleaching, however, oxygen can be removed and the OFF-times adjusted by addition of an alternative oxidizing agent, e.g. methyl viologen.

Another characteristic feature of ATTO655 is that the number of photons emitted can be tuned by varying the concentration of AA. High photon numbers offer the advantage of higher localization precision, but at the cost of imaging speed and vice versa. The ideal parameters for each type of experiment are found empirically [22].

1. Prepare a working solution of AA by diluting the 100 mM stock 1:10 in PBS.
2. Fill 95 % of the LabTek chamber with PBS (containing 1 % glucose if oxygen removal is required).
3. Add 7 µl of AA working solution.
4. Note: No oxygen removal is required.
5. Note: Optimize Blink parameters as discussed in the section on **Finding the Right Blink Parameters**.

Other Dyes

Many other dyes can potentially be used for Blink Microscopy. We found the fluorophore Alexa 546 to work with the same parameters as given for ATTO655 in the previous section. It may be helpful to also try other reducing agents, like the thiols mercaptoethylamine (MEA) or beta-mercaptoethanol (ME), if ascorbic acid does not show the desired effect (see dSTORM, ref [26]). In the case of thiols, the reducing species is the thiolate, which means that thiols are used at higher concentrations and reproduced through the acid-base equilibrium. For thiols, however, the pH has to be carefully controlled, since the effective thiolate concentration is strongly pH dependent.

3.4.6 Finding the Right Blink Parameters [36]

In a first step, acquire 2000 frames at the fastest camera integration time (≈4 ms) and highest laser power (≈200 mW). Discard the first 10 – 200 frames, when too many

dye molecules are still in their ON-state. Browse through the raw data looking at individual frames.

It is essential that the raw data is of good quality, exhibiting single-molecule blink events with a good SNR. The following sections should help to identify possible error sources and eliminate them.

Check for Single Molecule Events

When looking at consecutive frames, diffraction limited spots should be identified. They must be perfectly circular (within the limit of the pixel size), uniform in brightness, and appear and disappear within one or two frames. If all spots appear asymmetric or elliptical in the same way, microscope detection optics should be checked. Otherwise, the dyes are not blinking properly and multiple spatially-distributed emitters are forming an asymmetric emission pattern.

Laser Intensity / ON-times

Assuming one is imaging with the highest laser intensity possible and has succeeded in imaging single-molecule events, look at individual fluorescent regions over time. Most Blink events (ON-times) should have a length of 1 – 3 frames. Consider that ON-times are distributed exponentially.

1. If the majority of events exhibit ON-times of 3 or more frames, the laser intensity can be increased. Alternatively, the ON-times of dyes like ATTO655 can be reduced by adding higher amounts of a reducing agent. If both these measures are not feasible or sufficient, a longer ON-time is acceptable in the case that the OFF time is sufficiently long and/or the sample is not too densely labeled.
2. If all or almost all fluorescent events occur within just one frame, meaning fluorescence starts in one frame and is no longer detected in the next frame, the laser power is set too high and should be decreased until a distribution of ON-times, as described above, is obtained.

OFF-times

For localization-based super-resolution microscopy to work, Blink events from individual molecules within a diffraction-limited area must be separated in time. In principle, just one dark frame in between two Blink events is sufficient, however, the exponential distribution of OFF-times makes it necessary to have a cumulative average OFF-time of at least a few frames. This cumulative OFF-time is the time while all molecules within the area of one diffraction limited spot are in their dark state, and is the cumulative effect of a stochastic distribution of the OFF-times of all single emitters.

If fluorescence events are not separated by several dark frames, try adjusting (decreasing) the oxidizing agent concentration. Alternatively, if the

DOL of the secondary antibody is greater than two, re-labeling of the antibody with a lower dye concentration is recommended.

Camera Integration Time and Laser Intensity

According to ref [36], the camera integration time is ideally set to equal approximately twice the average ON-time of a single fluorophore. In most cases, the fastest possible recording time (5 – 10 ms) is desired, as this minimizes drift effects. Depending on whether the camera speed or the laser power is the limiting factor, the other must be adjusted to obtain optimal resolution. To increase the camera frame rate, a subset of the CCD pixels can be read out to achieve faster acquisition. This is especially applicable when using TIRF illumination, which often does not excite the whole field-of-view.

3.4.7 Data Collection

Software

The collection of data is relatively uncritical, and therefore there is a large range of feasible possibilities. One of the simplest possibilities is the use of the software supplied by the camera manufacturer, combined with subsequent analysis in a separate software program. More elegantly, one could use highly integrated software that controls the whole microscopy system and integrates live display of the super-resolution image as it is recorded. This software is usually provided with commercial microscopes.

Camera Settings

1. Cool the camera to -55 °C; this can take a few minutes.
2. Enable EM gain and set it to 250 (see **Note 4**).
3. Enable frame transfer mode. This is an important setting. Otherwise there will be pauses for CCD readout between the camera frames. Photons emitted during this time will not be detected (up to 80 %).
4. Set the camera integration time (see the section on **Camera Integration Time and Laser Intensity**).

Recording Raw Data

1. The laser should run at the full power used for SR imaging. When imaging to find the structure of interest and adjust the focus, the laser should be attenuated to about 5 mW to avoid introducing significant photobleaching.
2. It has proven practical to use a fast remote-controlled shutter to protect the sample from photodamage while removing (or adjusting) the attenuator.
3. Before opening the shutter, image acquisition should be started to collect some dark frames. This has the advantage that when the shutter is opened, an image is acquired where all fluorophores are still in their active state. This resembles a standard wide field image that can subsequently be compared to the SR image.
4. Images can be acquired until no more fluorophores are active (complete photobleaching has occurred).

Post-Processing

As the raw data of a SR image is a stack of thousands of diffraction-limited images, the information of each frame must be extracted and combined into a single graph. There are several approaches that differ in speed, accuracy, and their level of corrections. If you are using a custom-built microscope, there are several programs freely available on the internet [9, 37, 38]. Usually, in a first step, single-molecule Blink events are identified. In this step, algorithms can be applied that exclude emission from multiple molecules, which are identified by shape or intensity. Second, the identified spots are fit to a two-dimensional Gaussian function. The most straightforward approach utilizes a least-square fit. This yields very accurate results, but is relatively time consuming. Simpler alternatives involve the centroid-finding functionalities included in most programming environments, e.g. LabView, Igor, or Matlab. Faster, more specialized algorithms, are developed constantly [39].

As an example, a set of Blink Microscopy data was analyzed with three different software packages that are freely available (see Figure 2.3). The software available from the publication of DNA-PAINT [9], the built-in Igor localization algorithm, and the ImageJ-plugin named quickPALM [38] were employed using standard settings. For better comparison, molecule coordinates were exported and plotted in Origin. This comparison is not meant to identify "the best" software, or to give a comprehensive overview of what is available, but to

show that the choice of data analysis software may have an influence on the interpretation of SR data.

3.5 NOTES

1. *What is the Resolution, Actually?* One of the most important and probably most asked questions about super-resolution microscopy is: "what is the best resolution one can get?". Each publication on a new SR method claims to achieve a number as low as possible, and this claim is generally supported by using an experimental example. However, it is hard to predict the resolution limit of a particular experiment in advance [40]. In practice, determining the achieved resolution limit will require finding and imaging very small structures that are at or below the resolution limit of the experiment (see discussion in section on **Microscope Set-up**). Additionally, there are several aspects relating to the conditions used for labeling that can further limit or enhance the achievable resolution. The first resolution-limiting factor, relating to the density and size of the label, is independent of the imaging method chosen. In general, the higher the degree of labeling, the more detail can be resolved in an image. Therefore, the labeling of the sample must be sufficiently high to show the required amount of detail for the desired resolution. Once again, quoting Nyquist in a different context [41], the labeling density must be at least twice the resolution of the image. In practice, if one wants to discern two objects at a distance of 10 nm, there must be room for a fluorescent label every 5 nm or less. Speaking in a simplified, descriptive way, there must be room for a gap (or label) between the two objects.

When using indirect immunostaining methods (using primary and secondary antibodies), the achievable resolution may be limited to >30 nm, because the antibodies are generally 5-15 nm in size. This is one of the reasons why we prefer using Fab_2 fragments over whole IgGs.

Secondly, the resolution of localization-based microscopy indirectly depends on the labeling density, the number of fluorophores per diffraction-limited area. If a structure is densely-packed, there is a higher probability that there will be more than one dye in an ON- state within a diffraction-limited area than if the same number of dyes are diffusely spread over a larger area. If a software program attempts to fit a diffraction-limited spot that contains more than one dye, false localizations may be present in the final SR image and the overall resolution of the SR image will be decreased [36]. Increasing the OFF-times of the dyes will effectively decrease the labeling density because it will reduce the number of dyes that are emitting in a PSF at a given time. Therefore, imaging a densely-packed structure requires longer OFF-times than when imaging a diffusely-spread signal. In practice, this means that longer OFF-times are required when imaging a densely-packed cluster of proteins than when imaging a cytoskeleton protein that is diffusely located along a filament [40]. In this manner, the resolution obtained in one published experiment is not necessarily what can be achieved in a different context.

2. If there is more than a small bubble of air in the chamber, increase all volumes proportionally.

3. There is no need for an oxidizing agent, as cyanine dyes switch on spontaneously by the remaining oxygen.

4. All current EMCCD cameras offer a linear gain in the range of about 1 – 1000. If your camera gain cannot be set to 250, set it to the highest possible value.

5. *It's a graph, not an image*. The output of the software described in the section on **Post-Processing** reports fluorophore coordinates in a double precision floating-point format (e.g. x = 31.23589062, y = 9.14215860). Each coordinate by itself is zero-dimensional, so it does not occupy any space in an image. The pixels in a SR image are created by binning the number of localizations within a certain area (e.g. 10 µm divided into 10 nm pixels). The size of these bins can be chosen arbitrarily and changed in post-processing without loss of information. However, the more important question is: What binning is actually reasonable? According to the sampling theorem of Nyquist [41], the bin size must be at least half the expected resolution of the method. For a resolution of 20 nm, then, the recommended pixel size is somewhere between 5 – 10 nm. Fig. 4 shows a particular structure binned in 30, 10 and 3 nm pixels. Choosing the bins too large (left) makes it impossible to determine the substructure in the example. The center binning reveals a structure in the area of interest. When the bins are chosen too small (right panel), mostly single pixels are visible, which do not form an image easily perceived by the eye. The pixel size must therefore be chosen carefully, particularly when automatically analyzing SR images to determine cluster sizes. This should actually be done not on a SR image, but directly on the localization coordinates with specialized algorithms.

3.6 FIGURE LEGENDS

Figure 3.1. An example of Blink Microscopy data from filamentous actin on a glass surface (reproduced/adapted with permission from ref. [36], doi: 10.1007/978-90-481-9977-8_5). Left: At the beginning, all fluorophores are in their ON state. This ensemble of fluorescent molecules provides a diffraction-limited image. Center: The excitation laser quickly drives all molecules into their OFF-state while individual molecules switch back ON and can be localized as single-molecule events with high precision. This step is at the heart of Blink Microscopy and most experimental parameters described in this chapter aim at optimizing this single-molecule blinking. Right: all found localizations are binned into a super-resolved image.

Figure 3.2. Dark state reactions used for Blink Microscopy (reproduced/adapted with permission from ref. [16], doi: 10.1002/cphc.201000189). a) Jablonski diagram showing the photophysical states of a single fluorophore. The driving force behind the OFF-switching reaction is provided by fluorescence excitation (k_{exc}), followed by occasional intersystem crossing (k_{ISC}) and reduction by a reductant in solution (k_{Red}). The fluorophore switches back ON due to oxidation by oxygen or an added oxidant (k_{Ox}). Note that there is no need for a separate switching laser and that the reaction is fully reversible, so that each dye can run through many ON-OFF cycles. b) Fluorescence vs. time transient showing several switching cycles of a single fluorophore.

Figure 3.3. Blink Microscopy data analyzed with different software programs. a) An example of the localization of the protein DC-SIGN on fixed human dendritic cells

following sequential immunostaining (with DCN46, Invitrogen, and ATTO655-Fab, ATTO-TEC) and imaging with Blink Microscopy. The standard TIRF image is shown in green, overlaid with red SR data. The cell boundary is indicated by a red line. A subset of SR raw data was analyzed with b) DNA-PAINT software, c) quickPALM software and d) the IGOR standard spot finding algorithm. Each dataset was plotted in Origin to obtain comparable graphical output (unbinned, non-convoluted spot positions). Scale bars are 1μm.

Figure 3.4. Effects of bin size on SR image appearance. SR data binned in 30, 10 and 3 nm pixels (left to right).

FIGURE 3.1

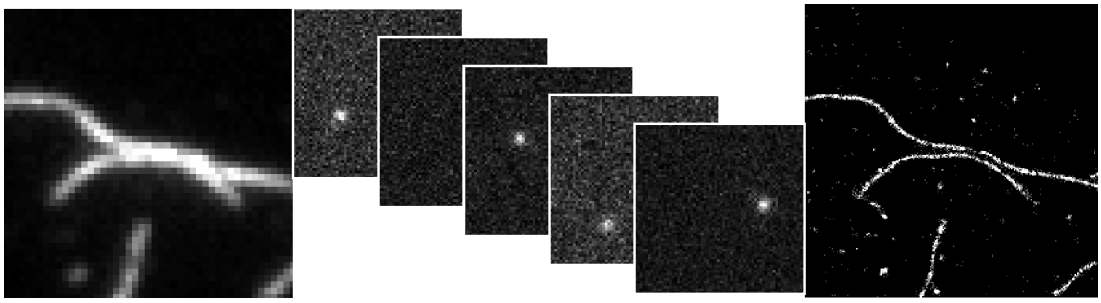

FIGURE 3.2

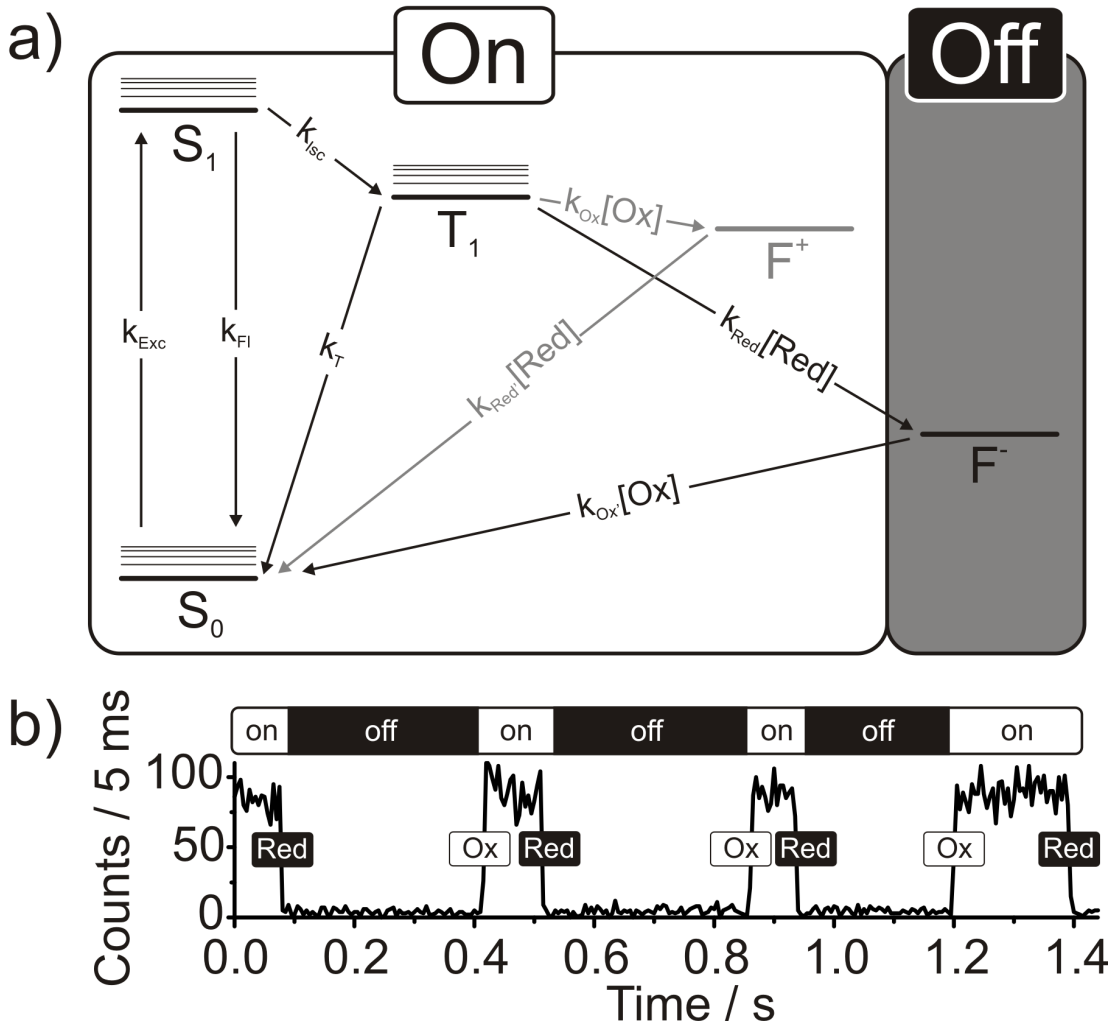
a)
On
Off
S1
T1
F+
F-
S0
kExc
kFl
kT
kisc
kOx[Ox]
kRed[Red]
kRed'[Red]
kOx'[Ox]
b)
on
off
on
off
on
off
on
Red
Ox
Red
Ox
Red
Ox
Red
Counts / 5 ms
100
50
0
0.0
0.2
0.4
0.6
0.8
1.0
1.2
1.4
Time / s

FIGURE 3.3

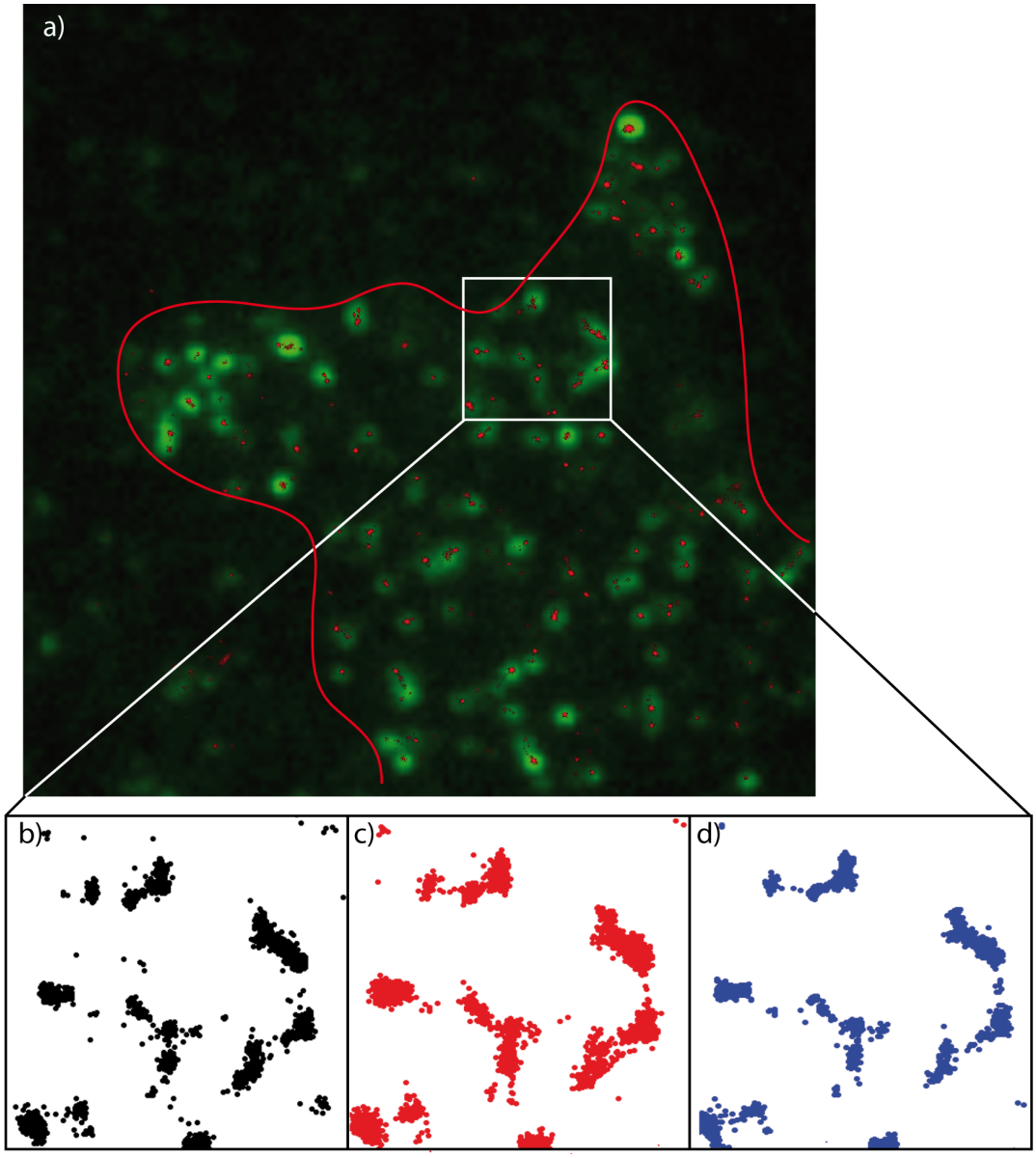

FIGURE 3.4

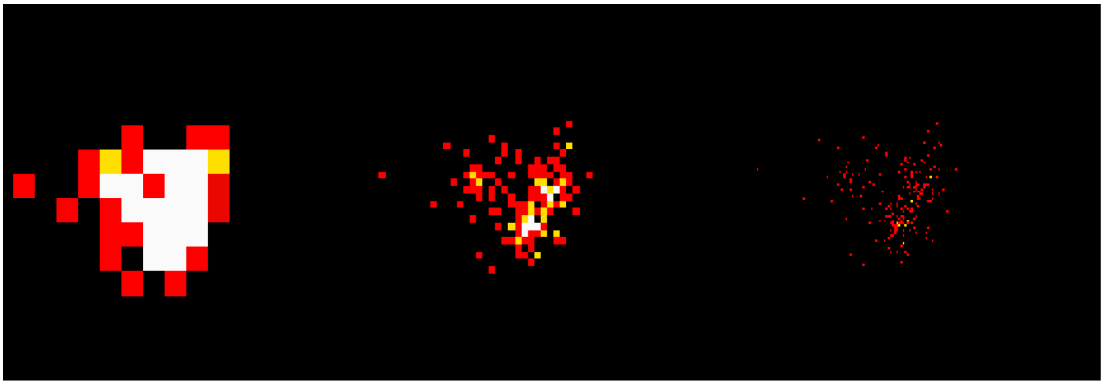

3.7 REFERENCES

1. Betzig, E., G. H. Patterson, R. Sougrat, O. W. Lindwasser, S. Olenych, J. S. Bonifacino, M. W. Davidson, J. Lippincott-Schwartz, and H. F. Hess. 2006. Imaging intracellular fluorescent proteins at nanometer resolution. Science 313:1642-1645.

2. Rust, M. J., M. Bates, and X. Zhuang. 2006. Sub-diffraction-limit imaging by stochastic optical reconstruction microscopy (STORM). Nat Methods 3:793-795.

3. Hess, S. T., T. P. Girirajan, and M. D. Mason. 2006. Ultra-high resolution imaging by fluorescence photoactivation localization microscopy. Biophys J 91:4258-4272.

4. Sharonov, A., and R. M. Hochstrasser. 2006. Wide-field subdiffraction imaging by accumulated binding of diffusing probes. Proceedings of the National Academy of Sciences of the United States of America 103:18911-18916.

5. Folling, J., M. Bossi, H. Bock, R. Medda, C. A. Wurm, B. Hein, S. Jakobs, C. Eggeling, and S. W. Hell. 2008. Fluorescence nanoscopy by ground-state depletion and single-molecule return. Nat Methods 5:943-945.

6. Steinhauer, C., C. Forthmann, J. Vogelsang, and P. Tinnefeld. 2008. Superresolution microscopy on the basis of engineered dark states. Journal of the American Chemical Society 130:16840-16841.

7. van de Linde, S., R. Kasper, M. Heilemann, and M. Sauer. 2008. Photoswitching microscopy with standard fluorophores. Applied Physics B: Lasers and Optics 93:725-731.

8. Heilemann, M., S. van de Linde, M. Schuttpelz, R. Kasper, B. Seefeldt, A. Mukherjee, P. Tinnefeld, and M. Sauer. 2008. Subdiffraction-Resolution Fluorescence Imaging with Conventional Fluorescent Probes. Angew Chem Int Ed Engl 47:6172-6176.

9. Jungmann, R., C. Steinhauer, M. Scheible, A. Kuzyk, P. Tinnefeld, and F. C. Simmel. 2010. Single-molecule kinetics and super-resolution microscopy by fluorescence imaging of transient binding on DNA origami. Nano Lett 10:4756-4761.

10. Gunkel, M., F. Erdel, K. Rippe, P. Lemmer, R. Kaufmann, C. Hormann, R. Amberger, and C. Cremer. 2009. Dual color localization microscopy of cellular nanostructures. Biotechnol J 4:927-938.

11. Flors, C., C. N. Ravarani, and D. T. Dryden. 2009. Super-Resolution Imaging of DNA Labelled with Intercalating Dyes. Chemphyschem.

12. Schoen, I., J. Ries, E. Klotzsch, H. Ewers, and V. Vogel. 2011. Binding-activated localization microscopy of DNA structures. Nano Lett 11:4008-4011.

13. Schwering, M., A. Kiel, A. Kurz, K. Lymperopoulos, A. Sprödefeld, R. Krämer, and D.-P. Herten. 2011. Hochauflösende Mikroskopie mit reversiblen chemischen Reaktionen. Angewandte Chemie 123:2996-3001.

14. Giannone, G., E. Hosy, F. Levet, A. Constals, K. Schulze, A. I. Sobolevsky, M. P. Rosconi, E. Gouaux, R. Tampe, D. Choquet, and L. Cognet. 2010. Dynamic superresolution imaging of endogenous proteins on living cells at ultra-high density. Biophys J 99:1303-1310.

15. Huang, B., H. Babcock, and X. Zhuang. 2010. Breaking the diffraction barrier: super-resolution imaging of cells. Cell 143:1047-1058.

16. Vogelsang, J., C. Steinhauer, C. Forthmann, I. H. Stein, B. Person-Skegro, T. Cordes, and P. Tinnefeld. 2010. Make them blink: probes for super-resolution microscopy. Chemphyschem 11:2475-2490.

17. Hell, S. W. 2007. Far-field optical nanoscopy. Science 316:1153-1158.

18. Heilemann, M., P. Dedecker, J. Hofkens, and M. Sauer. 2009. Photoswitches: Key molecules for subdiffraction-resolution fluorescence imaging and molecular quantification. Laser & Photonics Review 3:180-202.

19. Henriques, R., C. Griffiths, E. Hesper Rego, and M. M. Mhlanga. 2011. PALM and STORM: unlocking live-cell super-resolution. Biopolymers 95:322-331.

20. Fernandez-Suarez, M., and A. Y. Ting. 2008. Fluorescent probes for super-resolution imaging in living cells. Nat Rev Mol Cell Biol 9:929-943.

21. Vogelsang, J., R. Kasper, C. Steinhauer, B. Person, M. Heilemann, M. Sauer, and P. Tinnefeld. 2008. A reducing and oxidizing system minimizes photobleaching and blinking of fluorescent dyes. Angew Chem Int Ed 47:5465-5469.

22. Vogelsang, J., T. Cordes, C. Forthmann, C. Steinhauer, and P. Tinnefeld. 2009. Controlling the fluorescence of ordinary oxazine dyes for single-molecule switching and superresolution microscopy. Proc Natl Acad Sci U S A 106:8107-8112.

23. Cordes, T., M. Strackharn, S. W. Stahl, W. Summerer, C. Steinhauer, C. Forthmann, E. M. Puchner, J. Vogelsang, H. E. Gaub, and P. Tinnefeld. 2010. Resolving single-molecule assembled patterns with superresolution blink-microscopy. Nano Lett 10:645-651.

24. Steinhauer, C., R. Jungmann, T. L. Sobey, F. C. Simmel, and P. Tinnefeld. 2009. DNA Origami as a Nanoscopic Ruler for Super-Resolution Microscopy. Angew Chem Int Ed Engl 48:8870-8873.

25. Duim, W. C., B. Chen, J. Frydman, and W. E. Moerner. 2011. Sub-diffraction imaging of huntingtin protein aggregates by fluorescence blink-microscopy and atomic force microscopy. Chemphyschem 12:2387-2390.

26. van de Linde, S., A. Loschberger, T. Klein, M. Heidbreder, S. Wolter, M. Heilemann, and M. Sauer. 2011. Direct stochastic optical reconstruction microscopy with standard fluorescent probes. Nat Protoc 6:991-1009.

27. Wombacher, R., M. Heidbreder, S. van de Linde, M. P. Sheetz, M. Heilemann, V. W. Cornish, and M. Sauer. 2010. Live-cell super-resolution imaging with trimethoprim conjugates. Nat Methods 7:717-719.

28. Bierwagen, J., I. Testa, J. Folling, D. Wenzel, S. Jakobs, C. Eggeling, and S. W. Hell. 2010. Far-field autofluorescence nanoscopy. Nano Lett 10:4249-4252.

29. Cambi, A., F. de Lange, N. M. van Maarseveen, M. Nijhuis, B. Joosten, E. M. van Dijk, B. I. de Bakker, J. A. Fransen, P. H. Bovee-Geurts, F. N. van Leeuwen, N. F. Van Hulst, and C. G. Figdor. 2004. Microdomains of the C-type lectin DC-SIGN are portals for virus entry into dendritic cells. J Cell Biol 164:145-155.

30. Cordes, T., A. Maiser, C. Steinhauer, L. Schermelleh, and P. Tinnefeld. 2011. Mechanisms and advancement of antifading agents for fluorescence microscopy and single-molecule spectroscopy. Phys Chem Chem Phys 13:6699-6709.

31. Rothemund, P. W. 2006. Folding DNA to create nanoscale shapes and patterns. Nature 440:297-302.

32. Heilemann, M., E. Margeat, R. Kasper, M. Sauer, and P. Tinnefeld. 2005. Carbocyanine Dyes as Efficient Reversible Single-Molecule Optical Switch. Journal of the American Chemical Society 127:3801-3806.

33. Dempsey, G. T., M. Bates, W. E. Kowtoniuk, D. R. Liu, R. Y. Tsien, and X. Zhuang. 2009. Photoswitching mechanism of cyanine dyes. J Am Chem Soc 131:18192-18193.

34. Aitken, C. E., R. A. Marshall, and J. D. Puglisi. 2008. An oxygen scavenging system for improvement of dye stability in single-molecule fluorescence experiments. Biophys J 94:1826-1835.

35. Rasnik, I., S. A. McKinney, and T. Ha. 2006. Nonblinking and long-lasting single-molecule fluorescence imaging. Nat Methods 3:891-893.

36. Steinhauer, C., C. Forthmann, R. Jungmann, J. Vogelsang, F. Simmel, and P. Tinnefeld. 2011. Nanoscopy using localization and temporal separation of fluorescence from single molecules. In Biophotonics: Spectroscopy, Imaging, Sensing, and Manipulation. Springer.

37. Hedde, P. N., J. Fuchs, F. Oswald, J. Wiedenmann, and G. U. Nienhaus. 2009. Online image analysis software for photoactivation localization microscopy. Nat Methods 6:689-690.

38. Henriques, R., M. Lelek, E. Fornasiero, F. Valtorta, C. Zimmer, and M. M. Mhlanga. 2010. QuickPALM: 3D real-time photoactivation nanoscopy image processing in ImageJ. Nat Methods 7:339–340.

39. Wolter, S., M. Schuttpelz, M. Tscherepanow, V. D. L. S, M. Heilemann, and M. Sauer. 2010. Real-time computation of subdiffraction-resolution fluorescence images. J Microsc 237:12-22.

40. Vogelsang, J., C. Steinhauer, C. Forthmann, I. H. Stein, B. Person-Skegro, T. Cordes, and P. Tinnefeld. 2010. Make them Blink: Probes for Super-Resolution Microscopy. Chemphyschem.

41. Nyquist, H. 1928. Certain Topics in Telegraph Transmission Theory. Transactions of the American Institute of Electrical Engineers 47.

CHAPTER 4

DC-SIGN and Influenza Hemagglutinin Dynamics in Plasma Membrane Microdomains are Markedly Different[1]

4.1 SUMMARY

DC-SIGN, a Ca^{2+}-dependent transmembrane lectin, is found assembled in microdomains on the plasma membranes of dendritic cells. These microdomains bind a large variety of pathogens and facilitate their uptake for subsequent antigen presentation. In this paper, DC-SIGN dynamics in microdomains have been explored with several fluorescence microscopy methods and compared with those for influenza hemagglutinin (HA), which is also found in plasma membrane microdomains. Fluorescence imaging indicated that DC-SIGN microdomains may contain other C-type lectins and that the DC-SIGN cytoplasmic region is not required for microdomain formation. FRAP measurements showed that neither full-length nor cytoplasmically truncated DC-SIGN in microdomains appreciably exchanged with like molecules in other microdomains and the membrane surround, whereas HA in microdomains exchanged almost completely. Line-

[1] Reproduced/adapted with permission from:
Itano MS, Neumann AK, Liu P, Zhang F, Gratton E, Parak WJ, Thompson NL, Jacobson K, 2011. ***Dynamics of DC-SIGN and influenza hemagglutinin in microdomains on plasma membranes***, Biophysical Journal, **100**(11):2662-70.
doi: 10.1016/j.bbr.2011.03.031

Michelle S. Itano contributed to all of the Figures in the manuscript, and was also the primary contributor to the overall organization, writing and editing of this manuscript. Aaron K. Neumann contributed to Figures 4.1 - 4.3 and Supplemental Figure 4.1. Ping Liu contributed to Figure 4.5

scan FCS indicated an essentially undetectable lateral mobility for DC-SIGN but appreciable mobility for HA within their respective domains. SPT with defined valency quantum dots confirmed that HA has significant mobility within microdomains, whereas DC-SIGN does not. By contrast, FRAP indicated that inner leaflet lipids are able to move through DC-SIGN microdomains. The surprising stability of DC-SIGN microdomains may reflect structural features that enhance pathogen uptake either by providing high-avidity platforms or by protecting against rapid microdomain endocytosis.

4.2 INTRODUCTION

Immature dendritic cells are highly endocytic professional antigen presenting cells that recognize pathogen associated molecular patterns (PAMPs) to mediate antigen acquisition [1, 2]. Antigen recognition is facilitated by calcium-dependent antigen-capture receptors, called C-type lectins, that bind to high mannose structures present on the surfaces of numerous pathogens including viruses, bacteria, yeast and parasites [3, 4]. One C-type lectin abundantly expressed on immature dendritic cells is DC-SIGN (dendritic cell-specific intercellular adhesion molecule-3-grabbing non-integrin), also termed CD209. Other C-type lectins are also found on immature dendritic cells, including dectin-1 and macrophage mannose receptor (MMR, or CD206). The molecular details through which these transmembrane receptors mediate pathogen uptake are at present not fully understood. The work described in this paper focuses primarily on DC-SIGN.

DC-SIGN is thought to exist as a tetramer in the plasma membrane through interactions of the extracellular repeat domains of the protein [5-7]. Transmission electron microscopy and near-field scanning optical microscopy studies have determined that DC-SIGN molecules (presumably in the form of tetramers) in fixed cells are found in distinct protein microdomains on the nanometer scale [8-10]. More recently, the distribution and dynamics of DC-SIGN microdomains on the plasma membranes of live dendritic cells were examined by using wide field and confocal fluorescence microscopy techniques [11]. The clustering of DC-SIGN is required for efficient pathogen binding and internalization [8]. DC-SIGN clustering increases binding avidity, which may improve binding to small or multivalent ligands. The particular molecular interactions

that mediate the clustering of DC-SIGN have not yet been determined and, furthermore, the dynamics of DC-SIGN molecules within microdomains have not been investigated.

In this chapter, we describe our findings regarding the dynamics of the general pathogen receptor DC-SIGN, and compare the dynamics to those of the well-studied influenza hemagglutinin (HA). We find that DC-SIGN in microdomains is partially co-localized with dectin-1, MMR and clathrin. Multiple fluorescence microscopy techniques indicate that DC-SIGN is essentially immobilized in microdomains and that this stability is not dependent on the cytoplasmic tail of DC-SIGN. These findings contrast with HA, which also forms microdomains on the plasma membrane, but is laterally mobile within and outside microdomains and exchanges between these two regions. Although DC-SIGN shows no appreciable mobility within microdomains, lipids are free to move through these small regions. Taken together, our results strongly suggest that microdomains containing DC-SIGN have a complex, unexpected underlying molecular structure.

4.3 MATERIALS & METHODS

Cells

Human monocyte-derived immature dendritic cells were prepared from human whole blood obtained from the New York Blood Center (Long Island City, NY) as previously described [11]. Peripheral blood mononuclear cells were isolated from the blood by centrifuging over a Ficoll gradient (Ficoll-Paque PLUS, GE Healthcare,

Uppsala, Sweden) and resuspended in Dulbecco's phosphate-buffered saline (DPBS, 0.08 M sodium phosphate, 0.14 M NaCl, pH 7.4, GIBCO, Grand Island, NY) with 0.5 % (w/v) bovine serum albumin (BSA, Santa Cruz Biotechnology, Santa Cruz, CA). Monocytes were culled from the peripheral mononuclear cells by adherence to tissue culture flasks for 2-3 hours followed by washing with RPMI-1640 medium containing 10% fetal bovine serum (FBS). After approximately 24 hours detached cells were replated on glass-bottom MatTek dishes (MatTek Corp., Ashland, MA) with RPMI-1640, 10 % FBS, 500 U/mL of human IL-4 and 800 U/mL of human GM-CSF (Peprotech, Rocky Hill, NJ) to stimulate development of immature dendritic cells.

Three types of NIH 3T3 mouse fibroblasts permanently expressing different versions of human DC-SIGN were used. NIH 3T3 cells do not endogenously express mouse DC-SIGN [11]. The MX-DCSIGN cell line, originally generated by Drs. Thomas D. Martin and Vineet N. KewalRamani [12], was obtained through the NIH AIDS Research and Reference Reagent Program, Division of AIDS, NIAID, NIH. The Δ35-MX-DCSIGN and Δ20-MX-DCSIGN cell lines were made by using NIH 3T3 cells, plasmids encoding human DC-SIGN with either 35 or 20 amino acids truncated in the cytoplasmic region, respectively (a generous gift from Dan Littman, New York University and Howard Hughes Medical Institute, New York, NY), and the Phoenix-ECO retroviral packaging system (ATTC product# SD 3444) following the Phoenix-Helper dependent protocol (http://www.stanford.edu/group/nolan/protocols/pro_helper_dep.html). All three cell types were propagated in culture using the medium recommended for MX-DCSIGN, high glucose DMEM with 10 % FBS.

For the lipid FRAP experiments, DC-SIGN and a monomeric red fluorescent protein targeted to the inner leaflet of the plasma membrane (PMT-mRFP), were co-expressed in NIH 3T3 cells. The PMT-mRFP construct, kindly provided by Ichiro Maruyama (Genome Institute of Singapore, Singapore), contains the consensus sequence for *N*-myristoyl transferase and one site for the attachment of a palmitoyl moiety [13]. Previous work and our observations (data not shown) indicate that the protein product is mainly restricted to the plasma membrane [13, 14]. First, the DC-SIGN gene was amplified by polymerase chain reaction (PCR) from the pMX-DCSIGN vector (as obtained through the AIDS Research and Reference Reagent Program, Division of AIDS, NIAID, NIH, originally generated by Dr. Douglas Kwon and Dr. Dan Littman) with primers encoding *EcoR I* and *Sal I* sites (underlined), respectively: 5' –CCGGAATTCCA TGAGTGACTCCAAGGAACCAAGA and 5' –CAAGACGTCGACCTACGCAGGAG GGGGGTTTGGGGT. The PCR product was then digested with *EcoR I* and *Sal I*, and cloned into a modified pEGFP-C1 vector (Clontech, Mountain View, CA), kindly provided by Cai Huang (University of Kentucky, Lexington, KY), in which the EGFP gene was removed. The construct was confirmed by DNA sequencing. For the co-expression of DC-SIGN and PMT-mRFP, the ratio of the amounts of the two plasmids was kept at 1:1 (2 μg DC-SIGN/2 μg PMT-mRFP per dish). NIH 3T3 cells were seeded in 35 mm glass-bottom dishes (MatTek) in high glucose DMEM with 10 % FBS one day before transfection, and the mixture of the two plasmids were introduced into the cells by following the standard Fugene 6 protocol (Roche, Indianapolis, IN). Two days after transfection, cells were first stained by DCN46 (BD BioSciences, 10 μg/mL) for 15 min and followed by secondary goat anti-mouse Alexa488-conjugated IgG (Invitrogen, 1

μg/mL) for 5 min at 37 °C in an incubator. The cells were then washed thoroughly with DPBS, and covered with DPBS during the observation on the microscope. FRAP measurements were carried out at room temperature as described later in detail.

An NIH 3T3 cell line (called HAb2) that permanently expresses HA from the Japan strain of influenza was obtained from Judith White (University of Virginia, Charlottesville, VA). These cells were maintained in culture using high glucose DMEM with 10 % FBS.

Antibodies

Most antibodies were obtained commercially, as follows: mouse monoclonal IgG2b specific for human DC-SIGN (DCN46; BD Biosciences, San Jose, CA), rabbit polyclonal IgG specific for human DC-SIGN (H-200; Santa Cruz Biotechnology), goat polyclonal IgG specific for human dectin-1 (AF1859; R&D Systems, Minneapolis, MN), goat polyclonal IgG specific for human CD206 (MMR) (AF2534; R&D Systems), mouse monoclonal IgG2b specific for clathrin light chain from a variety of species (CON.1; Santa Cruz Biotechnology), Alexa568-conjugated and Alexa488-conjugated goat polyclonal antibodies specific for mouse IgG (Invitrogen), Alexa488-conjugated donkey polyclonal antibodies specific for goat IgG (Invitrogen), Alexa488-conjugated donkey polyclonal antibodies specific for rabbit IgG (Invitrogen), biotinylated, rat monoclonal IgG2a specific for human DC-SIGN (eB-h209; eBioscience, San Diego, CA), and biotinylated, mouse monoclonal IgG1 specific for HA (HA-7; Sigma-Aldrich, St. Louis, MO). According to the manufacturers, fluorescent antibodies contained approximately 5-

7 fluorophores per protein and biotinylated antibodies contained approximately 3-7 biotin moieties per protein.

Two antibodies were prepared in-house. The mouse hybridoma DC6, which secretes IgG1 specific for human DC-SIGN [15], was a gift of Robert Doms (University of Pennsylvania, Philadelphia, PA). The mouse hybridoma FC125, which secretes IgG2a specific for human HA [16], was obtained from Thomas Braciale (University of Virginia). In both cases, hybridomas were grown in PFHM-II protein-free hybridoma medium (GIBCO). DC6 and FC125 IgG were purified from hybridoma supernatants by Protein A affinity chromatography (Pierce Biotechnology, Rockford, IL). The column was sequentially washed with 100 mM and 10 mM Tris at pH 8.0 and eluted with 50 mM glycine at pH 3.0. Eluates (1-4 mL) were immediately neutralized with 1 M Tris (pH 8.0), concentrated by using spin columns (Ultracel-10k; Millipore, Billerica, MA) and dialyzed with Slide-A-Lyzer cassettes (Pierce Biotechnology) against 4 L PBS (diluted from PBS, 10×, Cellgro, Manassas, VA). For the line-scan FCS and the single-color FRAP experiments, these antibodies were conjugated with Alexa488 (Invitrogen), and the fluorophore to IgG ratio was estimated to be 0.7 according to the manufacturer's protocol.

Sample Preparation

In all cases, cells were plated in 35 mm glass-bottomed microscopy dishes (MatTek) in the appropriate medium. At the time of observation, cells were treated differently, such as fixed or permeabilized, depending on the measurement of interest as

described below. For all experiments the cells were always washed with PBS or media, and immersed in the appropriate medium not containing phenol red before imaging.

Co-Localization Measurements

Immature human dendritic cells were fixed by using paraformaldehyde solution [4 % (w/v) in PBS, pH 7.4] for 20 minutes at 25 °C. For measurements probing clathrin co-localization, cells were then permeabilized with PBS containing 0.01 % Triton-X-100 for 5 minutes at 25 °C. Fluorescence labeling was carried out by treating with primary antibodies (10 μg/mL), washing with medium, treating with fluorescent secondary antibodies (1 μg/mL), and then final washing. For the dectin-1 and CD206 measurements, the primary antibodies were goat polyclonal IgG specific for human dectin-1 and CD206, respectively, and the secondary antibodies were Alexa488-conjugated donkey polyclonal IgG specific for goat IgG. In these measurements, DC-SIGN was labeled with DCN46 followed by Alexa568-conjugated anti-mouse IgG. For the clathrin measurements, the primary antibodies were CON.1 and H-200, for clathrin and DC-SIGN, respectively, and the secondary antibodies were Alexa568-conjugated goat polyclonal IgG specific for mouse IgG and Alexa488-conjugated donkey polyclonal IgG specific for rabbit IgG, respectively.

Epifluoresence imaging was carried out on a dual-channel Olympus IX81 inverted microscope equipped with a 60× oil immersion, 1.4 N.A. objective and a 100 W Hg arc lamp. Filters and dichroic mirrors (Chroma Technology Corp., Rockingham, VT) for Alexa488 and Alexa568 imaging were as follows: Alexa488, excitation, 488/10,

emission, 535/25; Alexa568, excitation, 535/50, emission, 610/75. Images were captured using an air-cooled SensiCam QE CCD camera (Cooke Corp., Romulus, MI) driven by Metamorph (Molecular Devices/Meta Imaging, Downingtown, PA).

For percent co-localization analysis, domains were first identified using ImageJ as follows. A "cell area mask" was created by thresholding the original image at a value intermediate to non-cell and cell area backgrounds. The cell area mask was then used to exclude (set to zero intensity) all pixels from non-cell area regions thus creating the "cell area image". The cell area image was thresholded at the maximum intensity minus 1 standard deviation to remove background (autoflourescence of the cell), identify domain areas and create the "cell area domains image". An "eroded cell area mask" was created by applying the erosion function (single pixel width, ten iterations) to the cell area mask. Edge artifacts were avoided by multiplying the cell area domains image and the eroded cell area mask to create the "eroded cell area domains image". A watershed filter was then applied to the eroded cell area domains image to separate adjacent domains. The domains were then identified using the Particle Analyzer (1-200 pixels, 0.500-1 circularity) and output as a mask to generate the "final domains image" for each protein interrogated in the original images. The area of co-localization was determined by applying the logical 'AND' to the final domains images of two proteins to be compared. The logical 'OR' operation was used on the same images to determine the total domain area for both proteins. The percent co-localization was then calculated by taking the 'AND' area divided by the 'OR' area for each image pair.

In order to determine whether the co-localization was above what would be expected for two overlapping random distributions, a Ripley's-K bivariate analysis was applied. The final domains images were cropped to exclude cell boundaries and their centroids were identified using the Particle Analyzer. The centroids were used as input for the Cellspan software (University of New Mexico, New Mexico) to perform 'Ripley's K for bivariate data' analysis. Output is provided in the form of the L function, L(t)-t, as previously described [17]. This function transforms Ripley's K function to a form where L(t)-t=0 for random distributions at all length scales (t). When L(t)-t (black line) is within the confidence interval for randomness (i.e., between the red lines), this indicates a random distribution. L(t)-t greater than the randomness confidence interval indicates clustering on the length scales denoted on the x-axis of the graph.

Domain Imaging

MX-DCSIGN, Δ35-MX-DCSIGN, Δ20-MX-DCSIGN, and HAb2 cells were fixed by using PBS with 4 % (v:v) paraformaldehyde for 20 minutes at 25 °C. Cells were then fluorescently labeled by using primary and secondary antibodies as described above. The primary antibodies were either DCN46 or FC125 and the secondary antibodies were Alexa488-conjugated goat anti-mouse IgG. Images were acquired as described above for the green (Alexa488) channel.

Fluorescence Recovery After Photobleaching (FRAP*)*

Measurements were carried out on live cells. MX-DCSIGN and Δ35-MX-DCSIGN cells were labeled with 50 μg/mL Alexa488-conjugated DC6 for 5 minutes at

37 °C. HAb2 cells were labeled in the same manner with Alexa488-conjugated FC125. NIH 3T3 cells containing PMT-mRFP were fluorescent in the red channel as a consequence of the transfection and were labeled with DCN46 followed by Alexa488-conjugated goat polyclonal IgG specific for mouse IgG for the purpose of identifying the locations of DC-SIGN domains.

Measurements were carried out on an upright Olympus FV1000 confocal microscope equipped with a live cell chamber and a LUMPL FL 60× W/IR 0.90 N.A. water immersion objective or, for the lipid FRAP experiments, on an inverted Olympus FV1000 equipped with a live cell chamber and a 60× 1.42 N.A. oil immersion objective. The 488 nm line of the argon ion laser was used for the Alexa488 excitation and the 559 nm diode laser was used to excite the mRFP, with the laser power set between 0.1 and 5 % according to the power slider in the FV1000 microscope software, for monitoring pre- and post-bleach fluorescence intensities. The variable slit had a nominal bandwidth of 500-545 nm for the green emission channel and 590-650 nm for the red emission channel. Circular regions of interest (ROI) consisting of small areas on cell membranes containing individual domains were selected by using the green channel and the tornado scanning feature contained in the FV1000 software. These regions typically ranged from 1.2 to 3.4 μm in diameter. Larger, square areas with sides ranging from 13 μm to 66 μm and surrounding the smaller, selected circular regions were imaged during the course of the experiment. Circular regions surrounding individual domains were bleached by using either the 488 nm (for HA, full-length DC-SIGN and Δ35-DC-SIGN) or 559 nm (for PMT-mRFP) beam at 100 % power for 300 ms or 150 ms, respectively. Bleaching was

carried out to ~ 50 % completion so that the partially bleached domains could still be tracked.

FRAP data were analyzed as previously described [18]. For the analysis, three circular ROIs were defined within the larger, square areas that were used for image acquisition (see above). The first ROI (hereby referred to as ROI_1) was the same ROI as was used to define the bleached area for the tornado scan, and therefore was used to define the region containing the domain that was bleached during the experiment. The second ROI (hereby referred to as ROI_2) was placed in a region not occupied by the fluorescent cell and was used to define the contribution of background intensity during the experiment. The third ROI (hereby referred to as ROI_3), with the same dimensions as ROI_1, was placed around a nearby unbleached domain. The mean intensities from ROI_1, ROI_2 and ROI_3 as functions of time are denoted as $A_{raw}(t)$, $B(t)$ and $C_{raw}(t)$, respectively. First, the raw fluorescence data from $A_{raw}(t)$ and $C_{raw}(t)$ were background corrected by subtracting $B(t)$. Therefore, the mean intensities following background subtraction $A(t)$ and $C(t)$ were calculated as follows: $A(t) = A_{raw}(t) - B(t)$ and $C(t) = C_{raw}(t) - B(t)$. Next, the recovery data were adjusted to correct for the effects of photobleaching during pre-bleach and post-bleach observation. The data were adjusted in the following way: $F(t) = A(t)[C(-)/C(t)]$, where $C(-)$ was the average pre-bleach intensity (acquired before the bleaching tornado scan). The % recovery was calculated by using the expression $P(t) = 100[F(t)-F(0)]/[F(-)-F(0)]$, where $F(-)$ was the pre-bleach fluorescence and $F(0)$ was the fluorescence immediately after bleaching. The function $P(t)$ was fit to the phenomenological expression, $P(t) = P_\infty[1-\exp(-kt)]$, with P_∞ and k as free parameters,

using Igor Pro 6.0 (Wavemetrics, Portland, OR). From the fit, the values of P_∞ were taken as mobile percentages and the values of k were used to calculate recovery half-times as $\tau_{1/2} = k^{-1} \ln(2)$. The recovery times, $\tau_{1/2}$, for HA and the PMT-mRFP ranged from 2 s to 100 s and from 0.3 to 1.7 s, respectively. Apparent diffusion coefficients were calculated from $\tau_{1/2}$ by using the equation: $D = \rho^2/(4\tau_{1/2})$, where ρ denotes the radius of ROI_1 which is the radius of the bleached area. Other more nuanced methods for analyzing confocal FRAP data have been developed (e.g., [19]) but were not employed here.

The possibility that molecular exchange occurs with molecules arising from the cell interiors is considered to be highly unlikely for HA, full-length DC-SIGN and Δ35-DCSIGN in microdomains because this process would most likely require internalization of whole domains and subsequent recycling. First, recycling is expected to occur on a much longer time-scale than that for which FRAP measurements were carried out [20]. More importantly, selected domains were tracked subsequent to photobleaching and disappearance (internalization) of whole domains was not observed. For PMT-mRFP, it is possible but highly unlikely that post-bleach recovery occurred through exchange with unbleached molecules in the cell interior because recovery was measured over less than ten seconds; in any event, this effect would be expected to be small over such durations. Therefore, the values of P_∞ and $\tau_{1/2}$ are interpreted as arising from the molecular mobilities within and outside of domains, the distance between domains, and the kinetic barriers associated with entry into and exit from domains.

Line-Scan Fluorescence Correlation Spectroscopy (line-scan FCS)

Measurements were carried out on live MX-DCSIGN, Δ35-MX-DCSIGN, and HAb2 cells, prepared as described above for FRAP measurements. Confocal microscopy was performed on the FV1000 instrument using the same lasers and filters as described above for the FRAP measurements. For each line scan, 256×1 pixels were probed at 20.0 μs/pixel. The corresponding line time was 5.12 ms and the lag time between scans was 1.12 ms. A total of 32,000 lines was acquired per domain. The electronic zoom of the microscope was 16.3, which corresponds to a line length of 12.8 μm. For all line-scans, the pixel size was 50 nm in length and the $1/e^2$-radius of the point spread function (PSF) was $\omega = 0.30$ μm.

The line-scan data were analyzed using the SimFCS program (Laboratory for Fluorescence Dynamics, Irvine, CA). The intensity data are presented using a carpet representation in which the abscissa corresponds to the point along the line (pixels) and the ordinate corresponds to the time, with the first scan appearing at the top of the carpet and the last scan at the bottom. Domains were tracked and aligned to remove movement of the entire domain from the calculation of the molecular diffusion coefficient. A moving average correction was employed to remove slowly varying parameters from the analysis (e.g., photobleaching). Fluorescence fluctuation autocorrelation functions were calculated from the time-dependent, corrected data contained in each column of the carpet. These functions were curve-fit to $G(\tau) = G(0)/[1 + \tau/\tau_D]$ with $G(0)$ and τ_D as free parameters. Apparent molecular diffusion coefficients were calculated as $D = \omega^2/4\tau_D$.

The range of diffusion coefficients measurable by the version of line-scan FCS used in this work can be defined given the average time between line-scans (Δt = 6.24 ms) and the total number of line-scans (32,000). Assuming that the half-time for autocorrelation function decay must be at least five-fold higher than the time between sampling individual pixels, then $\tau_D = \omega^2/(4D) \geq 5\ \Delta t$. Thus, $D \leq \omega^2/(20\ \Delta t) = 0.7\ \mu m^2/s$. This upper limit is consistent with the values of D measured for HA. For the lower limit of measurable diffusion coefficients, if we assume that the half-time for autocorrelation function decay cannot be greater than the product of the scan time and one-half of the number of scans, then $\tau_D \leq 16{,}000\ \Delta t$ and $D \geq 2 \times 10^{-4}\ \mu m^2/s$. This lower limit is consistent with (some of) the values of D measured for DC-SIGN and Δ35-DC-SIGN. Physically speaking, the upper limit of this range derives from the fact, that owing to rapid diffusion, concentration fluctuations above the upper limit of D will decay almost completely during the sampling interval while the lower limit originates from the need for some decay of a fluctuation to occur within the sampling interval. It should be noted that the upper limit of D can be increased by several orders of magnitude by using the confocal microscope, but employing raster-scan image correlation spectroscopy [21-23].

For all measurements, G(0) values ranged from ≈ 0.0073 to 0.066. At this juncture, we do not feel comfortable analyzing G(0) values due to a number of experimental variables and insufficient theory to properly interpret the result. Primarily, photobleaching during data acquisition reduces the average number of fluorescent molecules in the probed region. Other concerns include whole cell or domain movement, particularly in the vertical direction which is not accounted for by the horizontal

alignment correction; uncertainty arising from the distribution of labels on the antibodies, possible self-quenching, and an unknown degree to which the molecules of interest are saturated with antibodies; and the lack of a theory that addresses spot-based FCS carried out on domains with an apparent size on the order of the spot size. These concerns may also raise the lower limit of intradomain diffusion coefficients measureable by line-scan FCS.

Quantum Dot (Qdot) Single Particle Tracking

Qdots emitting at 610 nm (CdSe/ZnS based, Evident Technologies, Troy, NY) with exactly one streptavidin per Qdot were generated according to a previously published procedure [24]. Briefly, hydrophobic Qdots were transferred into aqueous solution by coating them with an amphiphilic polymer, leading to a carboxyl-terminated surface [25]. Next polyethylene glycol (PEG) with a terminal biotin on the free-end of the PEG was covalently attached to the Qdots, leading to a hydrodynamic diameter of approximately 15 nm [26]. These biotin-Qdots were further treated with a saturating concentration of streptavidin. Electrophoresis was used to isolate Qdots containing only one streptavidin molecule [25].

These Qdots were diluted to a working concentration of 0.1 μM with Qdot Incubation Buffer (Quantum Dot Corp, Hayward, CA), and used at a 0.01 μM concentration when pre-incubated with a large excess of biotinylated anti-human DC-SIGN (eB-h209) or biotinylated anti-human HA (HA-7) antibodies in HHS (GIBCO HAMS F12 media supplemented with 15 % FBS and 25 μM HEPES) media for 1 hr,

rotating at room temperature. Unbound antibodies were removed by purification with a spin filter (Nanosep 100K Omega, PALL, Ann Arbor, MI). These complexes were then used to directly label live MX-DCSIGN or HAb2 cells at a concentration of 50 pM in HHS media, for 10 min at 25°C. Cells were then washed three times with HHS media.

Imaging was carried out on the Olympus IX81 instrument described above for co-localization measurements (Alexa568 channel), with the addition of a 0.6 neutral density filter for low-light movie acquisition. Sequential images were obtained with a cooled, intensified Stanford Photonics (Palo Alto, CA) XR/Mega-10Z ICCD camera at 100 Hz using the Piper Control Imaging software package (v.2.4.40) for 10 s (1000 frames). Data were acquired using the Track Objects function with the Threshold Result algorithm (50 % size match criterion). The spot of interest was defined manually by a 6×6 pixel region in the first frame and tracked automatically thereafter with a 10×10 pixel search area. Positions were determined as the centroids of the best-fits of the intensities to 2D-Gaussians. The algorithm can accommodate up to two blank frames that may arise from blinking. A very small proportion (< 5 %) of trajectories were not included in the analysis due to excessive blinking. Traces from Qdots adhered to the glass, in areas that did not contain a cell, were used to determine the amount of jitter that is expected from noise inherent to the acquisition and analysis according to the procedure outlined in [27].

Traces were analyzed using Microsoft Excel to calculate mean squared displacements (MSDs) as a function of time τ. The slopes of the first ten points of these

plots were used to calculate apparent diffusion coefficients according to MSD = 4Dτ. The intercepts are non-zero as previously described [27].

4.4 RESULTS & DISCUSSION

4.4.1 DC-SIGN Partially Co-Localizes with Other Transmembrane C-Type Lectins and Clathrin.

Previous work has shown that DC-SIGN appears as small (several hundred nm but in many cases greater than optical resolution) clusters, or microdomains, on the plasma membranes of live and fixed dendritic cells [8-11]. While it is clear that DC-SIGN ectopically expressed in fibroblasts and other cell types is sufficient for microdomain formation [11], we asked whether other C-type lectins mix with DC-SIGN in microdomains on dendritic cells.

Co-localization studies, using widefield fluorescence microscopy, were carried out on fixed, immature human dendritic cells for two candidate molecules, dectin-1 and macrophage mannose receptor (MMR), which are both C-type lectin transmembrane proteins that might be expected to be contained in DC-SIGN domains. As shown in Fig. 4.1, *A* and *B*, both dectin-1 and MMR are also present in microdomains. These clusters sometimes, but not always, co-localize with DC-SIGN microdomains (Quantified in Supplemental Fig. 4.1). Thus, DC-SIGN microdomains appear heterogeneous in the sense that they may or may not contain dectin-1 and/or MMR. Conversely, dectin-1 and MMR microdomains may or may not contain DC-SIGN. A variety of C-type lectin microdomains having different compositions could facilitate pathogen recognition,

internalization and subsequent antigen presentation in part by multiplexing signals from different pattern recognition receptors within the same domain.

Clathrin-coated pits are thought to mediate the internalization of cargo-loaded DC-SIGN microdomains [28]. As shown in Fig. 4.1 *C*, individual clathrin microdomains can be visualized on the cell periphery. Examining the images of these regions indicates that clathrin microdomains are sometimes, but far from always, co-localized with DC-SIGN domains. This result implies that clathrin is not required for DC-SIGN domain stability. However, it is possible that the DC-SIGN domains containing clathrin are more mature and that DC-SIGN acquires clathrin prior to internalization.

The images in Fig. 4.1 were obtained from fixed (and subsequently permeabilized, for clathrin) cells by using two-color indirect immunofluorescence labeling. The observed co-localization is above what would be expected due to random distribution of the proteins, as determined by a bi-variate Ripley's K-analysis (Supplemental Fig. 4.1). Minimal fluorescence was observed in either the green (dectin-1, MMR or DC-SIGN, in the case of clathrin labeling) or red (co-localized partner) channels when cells were treated only with the secondary, labeled antibodies and not the primary antibodies, or when NIH 3T3 cells (that do not endogenously express either HA or DC-SIGN) were stained with primary and secondary antibody, indicating specificity of labeling. It is highly unlikely that the domains shown in Fig. 4.1 were induced by the double-antibody labeling because, first, the cells were fixed prior to antibody treatment and, second, DC-SIGN domains with very similar appearance were observed on live cells treated only with

fluorescently labeled anti-DC-SIGN Fabs [11]. Also, other transmembrane proteins that form microdomains, including some members of the tetraspanin family, do not co-localize with DC-SIGN (data not shown).

4.4.2 Comparison of DC-SIGN Microdomains with Those of HA.

The manner in which cells pre-form molecular subassemblies to carry out different functions is a topic of current interest. Thus, it is valuable to compare the properties of DC-SIGN microdomains with those of another membrane protein known to form plasma membrane microdomains. For this purpose, influenza hemagglutinin (HA) was selected. HA is a glycoprotein found on the surface of influenza viruses and plays a key role in the process through which immunological cells bind and internalize the virus, and subsequently present it to other immunological cells for anti-viral immunity [29]. HA also assembles in microdomains on virally infected cell surfaces and these HA-containing clusters are presumed sites of viral budding [30, 31]. When HA is expressed alone in uninfected cells (e.g., fibroblasts), it forms plasma membrane microdomains on both fixed and live cells [32, 33]. The size and density of microdomains containing HA in uninfected NIH 3T3 fibroblasts stably expressing HA (HAb2 cells) are roughly similar to those of DC-SIGN microdomains (Fig. 4.2) and are used for comparison purposes throughout the remainder of the work described herein.

4.4.3 DC-SIGN Does Not Require its Cytoplasmic Tail to Form Membrane Microdomains.

The possibility arises that the formation of DC-SIGN clusters and/or their subsequent stability requires molecular interactions involving the 40 amino acid N-

terminal cytoplasmic region (Fig. 4.3 *A*). To address this question, mutants of DC-SIGN (Δ35-DCSIGN and Δ20-DCSIGN) in which the cytoplasmic domain was partially (Δ20) or almost completely (Δ35) deleted were ectopically expressed in NIH 3T3 cells using a retroviral expression system. Δ35- and Δ20-DCSIGN expression on these cell lines was visualized by using indirect immunofluorescence, after fixation, with the primary monoclonal antibody DCN46. As shown in Fig. 4.3, *B* and *C*, ectopically expressed Δ20-DCSIGN or Δ35-DCSIGN both form membrane microdomains on NIH 3T3 cells. Therefore, DC-SIGN microdomain assembly and stability do not require the cytoplasmic tail. This result indicates either that the cytoskeleton is not required or that cytoskeletal factors participate in forming and maintaining DC-SIGN microdomains only through one or more intermediary molecules of unknown origin at present.

4.4.4 Ability of Molecules within Microdomains to Exchange with Molecules of the Same Type from Other Cellular Regions.

One way to address the stability of plasma membrane microdomains is to characterize the degree to which molecules within the microdomains can exchange with molecules of the same type residing in 1) the areas of the membrane surrounding the domains; 2) nearby microdomains, with an intermediate step requiring diffusion through the distance between domains; or 3) the cell interior. Confocal FRAP was used to address this question. These measurements were carried out for HA, full-length DC-SIGN, Δ35-DCSIGN, and a lipid-linked fluorescent protein residing in the inner leaflet of the plasma membrane (denoted as PMT-mRFP). For all four molecules, exchange mobility was probed for molecules residing within either HA or DC-SIGN domains. Confocal FRAP

was also used to examine the exchange capability of PMT-mRFP and HA in regions not identified as domains.

In the confocal FRAP measurements, first, small, circular regions surrounding single domains were selected. The mean fluorescence intensity from these circular ROIs was monitored before and after photobleaching. The degree of photobleaching in the circular tornado scan was restricted to ≈ 50 % so that the domains could be tracked as they moved (slightly) as a whole in the membrane following the bleach pulse. Two aspects related to domain stability can be addressed by this type of measurement: the recoverable percentage P_∞ and the half-time for recovery $\tau_{1/2}$ (see Materials & Methods). The apparent diffusion coefficient can then be calculated for each $\tau_{1/2}$ value for the area of the bleach spot used in each experiment.

Fig. 4.4 *A* illustrates the results of a typical confocal FRAP measurement of an HA microdomain, labeled with Alexa488-conjugated FC125, on the surface of an HAb2 cell. Consistent with previous reports [34-36], overall, these measurements indicated that HA in microdomains exhibits a large recoverable percentage (P_∞ = 68 ± 10 %, mean ± standard errors of the means (SEM), Table 4.1). This result indicates that HA molecules within their microdomains exchange with those from outside the microdomains on a relatively fast time-scale. The recovery times, $\tau_{1/2}$, in general, should depend on the sizes of the bleached areas, the fractions of the areas occupied by the domains, the diffusion coefficients of the HA within and outside of the domains, and the rates of exchange associated with HA moving into and out of domains. Apparent diffusion coefficients,

calculated for each recovery curve using the $\tau_{1/2}$ and the radius of the bleach spot, yielded an average of D = 0.10 ± 0.01 $\mu m^2/s$. These values are based on the assumption that possible kinetic barriers for HA leaving and entering domains are negligible and that the D values for HA in domains and the surround are comparable. The fact that the diffusion coefficients are similar to those previously reported in works not emphasizing domains [34-36] suggests that the assumptions above are valid.

A representative confocal FRAP measurement for a domain containing full-length, wild-type DC-SIGN, labeled with Alexa488-conjugated DC6, on the surface of an NIH 3T3 cell is illustrated in Fig. 4.4 *B*. As shown, very little to zero recovery is detectable after > 4 minutes. This result is consistent with previous measurements [11] and contrasts starkly with the results for HA domains. There are several possible explanations for the lack of DC-SIGN recovery: 1) DC-SIGN is extremely restricted in terms of its mobility within microdomains and therefore does not exchange with DC-SIGN in the surrounding membrane on a measurable time-scale; 2) DC-SIGN is mobile within domains, but the domains maintain, through an unknown molecular mechanism, a strict separation between molecules within the domain and the surrounding membrane; 3) the density of DC-SIGN between microdomains is so low and the domains are so sparse that mobility between domains cannot be observed by confocal FRAP. As shown below, the apparent diffusion coefficient of DC-SIGN within domains is extremely low and therefore the first explanation is the most likely one.

The question arises of whether the cytoplasmic region of DC-SIGN participates in, or is responsible for, the dramatic, observed difference between the exchanges of HA and full-length DC-SIGN in microdomains with the membrane surround. Fig. 4.4 *C* shows a typical confocal FRAP measurement for a domain containing Δ35-DCSIGN, labeled with Alexa488-conjugated DC6, on the surface of an NIH 3T3 cell. As shown, DC-SIGN lacking its cytoplasmic region exhibits no appreciable difference from full-length DC-SIGN in these measurements. The average recoverable percentage is essentially zero on the time scale of the measurement. Therefore, direct association of the cytoplasmic region of full-length DC-SIGN with the cytoskeleton can be eliminated as the primary cause of DC-SIGN microdomain stability.

The observation that DC-SIGN domains are heterogeneous, at least in some cases containing dectin-1 and MMR, raises the essential question of possible sub-domain structure. One issue related to this question is whether or not lipids within DC-SIGN domains can freely exchange with the membrane surround. Interestingly, Pinaud et al. [37] find that a GPI-anchored probe dynamically partitions into GM1-enriched domains indicating that this probe can diffuse through such domains, usually, but not always, with a reduced diffusion coefficient within the domain. Confocal FRAP was carried out on NIH 3T3 cells transiently expressing DC-SIGN and PMT-mRFP, fluorescent in the red channel. In these measurements, plasma membrane microdomain regions for photobleaching (and pre-bleach and post-bleach observation) of PMT-mRFP were selected by DC-SIGN expression as reflected by labeling with DCN46 followed by Alexa488-conjugated goat polyclonal IgG specific for mouse IgG. Microdomains were

identified by the green channel (DC-SIGN) fluorescence but FRAP measurements were carried out on these regions in the red channel (PMT-mRFP). As shown in Fig. 4.5 *A* and Table 4.1, PMT-mRFP exhibited significant recovery after photobleaching (P_∞ = 69 ± 3 %), with an apparent diffusion coefficient of D = 1.7 ± 0.2 $\mu m^2/s$. These results indicate, first, that although DC-SIGN is extremely restrained within its plasma membrane microdomains, lipids are not. The percentage recoveries are equivalent to those observed in FRAP measurements of PMT-mRFP in regions of the plasma membrane that do not contain DC-SIGN (P_∞ = 76 ± 6 %, D = 1.8 ± 0.2 $\mu m^2/s$, Fig. 4.5, *B* and *C*, Table 4.1). Values of the apparent diffusion coefficients for PMT-mRFP, but not the recoverable percentages, are possibly underestimated because appreciable diffusion through the bleached region may occur during the bleach pulse. However, because the measured apparent D values are quite high and consistent with other measurements of PMT-mRFP [14] and other lipid [38] diffusion it is unlikely that these possible artifacts are significant within the context of the work described here. More importantly, the substantial recovery of the lipid analog suggests that it may diffuse between smaller, elemental units containing DC-SIGN, not resolvable by wide field microscopic methods. Whether the lipid analog can actually enter these putative units is an open question at this juncture.

4.4.5 Intradomain Mobility Monitored by Line-Scan FCS.

As described above, confocal FRAP indicates that the rate of exchange of both DC-SIGN and Δ35-DCSIGN between microdomains and the surrounding membrane is extremely low (i.e., not observable). A possible explanation for this result is that DC-SIGN is essentially immobile in domains (see above). To address this possibility, a

technique with greater spatial resolution than conventional FRAP is required. Recently, the inherent temporal and spatial components of data acquired with a standard laser scanning confocal microscope have been combined with fluorescence correlation spectroscopy analysis to determine rates of apparent diffusion or binding kinetics on the spatial scale of a single pixel [21-23]. Line-scan FCS is one such method. In this method, data are acquired by repetitively scanning the same single line. The data can be visualized by placing successive lines directly underneath the previous line-scan, creating a line-scan carpet, which is similar to a kymograph. Temporal fluctuations in the intensity of a single pixel in a carpet column, sampled on the ms time scale, are sufficient to produce autocorrelation functions that capture aspects of membrane diffusion over an area determined by the point spread function (PSF) but with a spatial resolution determined by the lateral pixel size.

To establish the use of line-scan FCS to study the lateral diffusion of molecules within membrane microdomains, we initially investigated the intradomain diffusion of HA. HAb2 cells, stably expressing HA, were stained with anti-HA FC125 conjugated to Alexa488. Line-scans were acquired and arranged into line-scan carpets (Fig. 4.6 *A*), in which domains of high fluorescence intensity are color coded to appear more red on the carpet and background and areas of lower fluorescence intensity are color coded to appear more blue. The domains were centered to remove horizontal positional jitter and then de-trended to remove the influence of slowly varying components like photobleaching (Fig. 4.6 *B*). Apparent diffusion coefficients were calculated for single pixels by analyzing the fluorescence intensity fluctuations over time in single columns of

the line-scan carpets; these analyses were carried out for each lateral pixel in each carpet to determine the apparent diffusion coefficients of HA within, at the edges, and outside of microdomains (Fig. 4.6 *C*). This analysis indicated that HA is highly mobile within domains with a mean apparent diffusion coefficient of D = 0.127 ± 0.005 $\mu m^2/s$ and that the apparent diffusion coefficients were approximately constant across the microdomains (Fig. 4.6 *D*). The apparent D for HA outside of domains was similar (data not shown).

Line-scan FCS was next used to probe the lateral mobility of DC-SIGN and Δ35-DCSIGN (labeled with Alexa488-conjugated DC6) within microdomains on NIH 3T3 cells. These data indicated that both molecules are essentially immobilized within their domains (Fig. 4.6). The average apparent diffusion coefficients for DC-SIGN and Δ35-DCSIGN in microdomains were found to be D = 0.0025 ± 0.0004 $\mu m^2/s$ and D = 0.002 ± 0.001 $\mu m^2/s$ (Fig. 4.6, Table 4.1). Furthermore, for both DC-SIGN and Δ35-DCSIGN, the diffusion coefficient was sometimes so small that the autocorrelation functions could not be fit to the appropriate functional form (see **Materials & Methods**). These diffusion coefficients are in the range of the lower limit of what could be measured with line-scan FCS under our experimental conditions (see **Materials & Methods**). Thus, the results indicate that DC-SIGN within its microdomains, unlike HA, undergoes very little lateral diffusion and is immobilized in some way. This immobilization can account for the lack of exchange of DC-SIGN and Δ35-DCSIGN between microdomains and the surrounding membrane on the time scale of confocal FRAP measurements.

4.4.6 Defined valency Qdot tracking confirms that DC-SIGN and Δ35-DC-SIGN exhibit much more restricted mobility than HA within domains.

To corroborate the line-scan FCS results and obtain additional information, Qdot tracking was employed to more directly investigate the dynamics of DC-SIGN molecules within microdomains at high speeds and with very high spatial resolution. In this type of measurement, it is important to use Qdots with limited valency, as Qdots with high valency have the potential to cross-link–DC-SIGN and yield results in which the measured lateral mobility is artifactually decreased. Therefore, a new synthetic Qdot method was employed in which Qdots covalently linked to streptavidin through biotinylated PEG spacers are subjected to gel electrophoresis [24]. This technique separates Qdots bound to none, one, or two streptavidin molecules into distinct bands, which are then cut from gels to isolate Qdots of defined valency [25].

Qdots conjugated to single streptavidin molecules were preincubated with biotin-anti-DC-SIGN or biotin-anti-HA antibodies. The maximum biotin valency of the Qdots is three; however, one of these biotin binding sites is most likely sterically inaccessible due to the streptavidin structure, strongly suggesting that the maximum valency of these Qdots is two. In addition, the two remaining binding sites are likely too close together to accommodate two antibodies. NIH 3T3 cells stably expressing HA, DC-SIGN or Δ35-DC-SIGN were labeled with these preincubated Qdots and movies were acquired at 100 Hz for 10 s. Single particle tracking analysis was then carried out. Tracking analysis was restricted to single Qdots, which were identified by avoiding very bright clusters and observing Qdot blinking during the video.

Representative Qdot traces are shown in Fig. 4.7 and the results are summarized in Table 4.1. In all cases, plots of the MSD as a function of time saturated during the period of investigation. The initial slopes were high for HA but very low for DC-SIGN and Δ35-DC-SIGN. Apparent diffusion coefficients were calculated from the initial slopes of these plots (by using only the first ten points). This analysis gave D = 0.103 ± 0.003 $\mu m^2/s$ (R^2 = 0.82) for HA, which is approximately equal to the value measured by FRAP and line-scan FCS (Table 4.1). Approximately 28 % of the traces were on Qdots that were determined to be immobile and were not used to calculate the average D. The apparent diffusion coefficients for DC-SIGN and Δ35-DC-SIGN were 0.003 ± 0.001 $\mu m^2/s$ (R^2 = 0.76) and 0.0004 ± 0.0001 $\mu m^2/s$ (R^2 = 0.99), respectively. Positional jitter arising from mechanical fluctuations, flexibility through the PEG-streptavidin-antibody linkers, and/or statistical noise associated with the Gaussian fits was evaluated by carrying out tracking analyses for Qdots strongly adhered to glass surfaces. These measurements gave apparent D values of 0.0025 ± 0.0001 $\mu m^2/s$ (R^2 = 0.47). Therefore, the diffusion coefficients of DC-SIGN and Δ35-DC-SIGN measured by Qdot tracking are within the range of those produced by fluctuations due to sources other than lateral diffusion, consistent with the results obtained with line-scan FCS and confirming essential immobility of DC-SIGN within its microdomains.

4.5 DISCUSSION

Pathogen recognition by DC-SIGN is implicated in the defense or infection route against many critical players in human disease including HIV-1, dengue virus, hepatitis

C, and *Candida* [2-4]. This calcium-dependent (C-type) transmembrane lectin is endogenously expressed in small microdomains on the plasma membranes of immature dendritic cells, key mediators between the innate and the adaptive arms of the immune system, and DC-SIGN clusters are required for efficient pathogen binding and internalization [8-11]. The manner in which DC-SIGN clusters mediate either crucial (infection defense) or detrimental (infection) functions is of considerable interest. In this work, we have reported a number of observations that both enhance current understanding of the structure and dynamics of DC-SIGN microdomains and also raise a number of intriguing questions.

Co-localization imaging showed that DC-SIGN clusters sometimes, but do not always, contain two other C-type transmembrane lectins (dectin-1 and MMR); furthermore, DC-SIGN clusters are partially co-localized with clathrin. The observation that DC-SIGN microdomains may or may not contain more than one C-type lectin implies that these clusters are heterogeneous in composition; i.e., that a spectrum of microdomain sub-types exists. This conclusion is supported by recent work showing that the multiplexing of C-type lectins is regulated so that pattern recognition receptors sample the phagosome in a sequential manner [39]. Multiple C-type lectins are also found in contact sites between dendritic cells and yeast that stimulate formation of a recently defined cellular protrusive structure, the fungipod, which participates in fungal recognition by dendritic cells [40]. The compositional heterogeneity of C-type lectin microdomains may be required for efficient pathogen recognition and processing.

Cell imaging showed that two forms of DC-SIGN with partially or almost completely deleted cytoplasmic regions form plasma membrane microdomains that appear, within classical, light microscopic resolution, to be similar in size and distribution to those formed by wild-type, full-length DC-SIGN. Therefore, DC-SIGN domain formation and stability do not require direct interactions between DC-SIGN and cytoskeletal components close to the inner leaflet of the plasma membrane. However, whether the truncation mutants form a domain substructure identical to that of wild-type DC-SIGN domains remains an open question.

Consistent with previous results [11, 34-36], confocal FRAP measurements showed that neither DC-SIGN nor cytoplasmically truncated DC-SIGN in microdomains undergo measureable exchange with the pool of like proteins in the surrounding membrane whereas HA in microdomains [35] does exchange with the surround. Apparent plasma membrane diffusion coefficients calculated for HA are consistent with long range diffusion coefficients of a number of transmembrane proteins ($\approx 0.1\ \mu m^2/s$), but for DC-SIGN and its variants, the measurements yield apparent diffusion coefficients so low that it is not possible to distinguish between the possibilities of extremely slow mobility and instrumental constraints.

To further illuminate the FRAP results, both line-scan FCS and Qdot tracking measurements were carried out for DC-SIGN, cytoplasmically truncated DC-SIGN, and HA. These measurements yielded apparent diffusion coefficients for HA, both within and outside of microdomains, that were consistent with the D values measured by confocal

FRAP. More importantly, these measurements showed that the two forms of DC-SIGN were so limited in their intra-domain mobilities that, again, it was not possible to distinguish between the possibilities of extremely slow mobility and instrumental limitations. Thus, the mobility of DC-SIGN variants within microdomains is very low, and most likely accounts for the lack of exchange between the domains and their surrounds observed by confocal FRAP.

Surprisingly, although DC-SIGN and cytoplasmically truncated DC-SIGN are unable to exchange with the membrane surround, a lipid-linked fluorescent protein bound to the inner leaflet of the plasma membrane does undergo significant exchange with like proteins in the surrounding membrane. Thus, lipid molecules can permeate and diffuse through these domains relatively unimpeded, suggesting that the bilayer is contiguous within the domains in spite of the fact that, in wide-field microscopy, they appear continuous and can be sized [11]. This result strongly suggests that DC-SIGN microdomains are not only heterogeneous in composition but also that they possess a complex internal structure with features smaller than can be resolved by conventional fluorescence microscopy, consistent with earlier results obtained with near-field microscopy [10]. We are currently conducting super-resolution microscopy studies to explore C-type lectin domain structure on smaller length scales (M.S. Itano et al., unpublished observations).

Precisely which protein, or perhaps lipid, components maintain the surprising stability of DC-SIGN in microdomains, and possibly other cell-surface microdomains

containing C-type lectins, is a key structural issue. DC-SIGN microdomains might be organized through direct interactions between DC-SIGN molecules, although this possibility seems at present to be too simple of a picture given that we now know that DC-SIGN microdomains contain a number of other molecules and have preliminary results from super-resolution microscopy (data not shown) suggesting otherwise. Three possible hypotheses for explaining the stability of DC-SIGN microdomains include attachments to other microdomain-forming transmembrane proteins (e.g., tetraspanins [41]); interaction of DC-SIGN with as yet unidentified molecules that bridge the gap to the cytoskeleton; and binding to members of the secreted family of galectins [42] known to organize membrane scaffolds. The resolution of this important issue awaits advanced compositional investigations.

Taken together, our results highlight the fact that DC-SIGN microdomains are considerably more complex than previously thought and may provide a prototype for certain other cell-surface, protein-containing microdomains. Moreover, signaling is initiated from these domains [2-4, 40] and they can be rapidly transported rearward in dendritic cells to sites of internalization [11]. It is clear that a better understanding of how the composition, structure and dynamics of C-type lectin domains mediate pathogen internalization could suggest means to modulate pathogen entry and antigen acquisition in cells of the innate immune system.

4.6 CREDITS

For their generous gifts, we thank Judith White, Thomas Braciale, and Robert Doms for the HAb2, FC125 and DC6 cell lines, respectively, Ichiro Maruyama for the PMT-mRFP construct, Cai Huang for the modified pEGFP-C1 vector, and Dan Littman for the pMX-Δ20-DCSIGN and pMX-Δ35-DCSIGN plasmids. We also thank Xiang Wang, Dept. of Chemistry, University of North Carolina, Chapel Hill, NC, and Michelle Digman, Laboratory for Fluorescence Dynamics, Dept. of Biomedical Engineering, University of California, Irvine, CA, for their contributions. This work was supported primarily by NIH grant GM-041402 (KJ and NLT). Additional funding was provided by NIH Cell Migration Consortium grant GM-064346 (KJ), NSF grant MCB-0641087 (NLT), NIH grant P41-RR-003155 (EG), NIH grant P50-GM-076516 (EG), European Commission grant Nanognostics (WJP), and German Research Foundation grant PA794/11-1 (WJP).

4.7 FIGURE LEGENDS

Figure 4.1. DC-SIGN partially co-localizes with other lectins and clathrin on immature dendritic cells. (*A*,*B*) DIC image of a dendritic cell on left and an overlay of the same area stained for DC-SIGN (DCN46 and anti-mouse-Alexa568) in red and either Dectin-1 stained with AF1859 and anti-goat-Alexa488 (*A*) or CD206 stained with AF2534 and anti-goat-Alexa488 (*B*) in green on the right. (*C*) Overlay of a dendritic cell stained for DC-SIGN (H-200 and anti-rabbit-Alexa488) in green and Clathrin LC (CON.1 and anti-mouse-Alexa568) in red. Areas of co-localization are seen as yellow. Scale bars, 10 μm (*A*,*B*), 5 μm in (*C*).

Figure 4.2. Comparison of DC-SIGN and HA microdomains. (*A*) DC-SIGN expression on a dendritic cell stained with DCN46 and anti-mouse-Alexa488. (*B*) HA expression on an HAb2 cell stained with FC125 and anti-mouse-Alexa488. Marked areas are shown at higher magnification in insets. Scale bars, 10 μm; Scale bar insets, 1 μm.

Figure 4.3. Ectopic expression of DC-SIGN with truncations in the cytoplasmic tail form membrane microdomains. (*A*) Schematic representations, not to scale, of wildtype (wt) full-length DC-SIGN, Δ20-DCSIGN and Δ35-DCSIGN, the latter two of which have deletions in the cytoplasmic tail of DC-SIGN. The cytoplasmic tail is depicted on the left of the transmembrane (TM) domain, while the extracellular portion of the wt protein is depicted to the right of the TM domain. Two internalization motifs are present in the cytoplasmic tail, a di-leucine based motif (LLEEE) and a tyrosine-based motif (YKSL). The extracellular portion of the protein contains 7.5 tandem repeats, which are thought to

mediate the tetramerization of DC-SIGN, followed by a carbohydrate recognition domain (CRD). (DC-SIGN is a type 2 membrane protein so that its C-terminus is at the end of the ectodomain.) (*B*-*D*) NIH 3T3 cells stably expressing either wildtype (*wt*) full-length DC-SIGN in (*B*), Δ20-DCSIGN in (*C*) or Δ35-DCSIGN in (*D*) stained for DC-SIGN (DCN46 and anti-mouse-Alexa488). Marked areas are shown at higher magnification in inset. Scale bars, 10 μm; Scale bar insets, 1 μm.

Figure 4.4. Ability of molecules within microdomains to exchange with molecules of the same type from other cellular regions. (*A*-*C*) Fluorescence recovery of a bleached domain on an HAb2 (*A*), MX-DCSIGN (*B*), or Δ35-MX-DCSIGN (*C*) cell stained with either FC125 (*A*) or DC6 (*B*,*C*) conjugated to Alexa488. A montage showing the bleaching of a representative cluster is above each recovery profile. The area of photobleaching is indicated by the circle in the first image. Images prior to photobleaching ($t \approx -10$ and -5 s) are shown on the left of the small arrow, which indicates the first image directly following the time of photobleaching ($t \approx 0$ s); images following photobleaching are shown to the right of the arrow ($t \approx 100$ and 200 s). The bleached domain is indicated with a large arrow. Given the definition of P(t), the plotted function is zero immediately after photobleaching. Scale bars, 500 nm.

Figure 4.5. Ability of lipids within DC-SIGN microdomains to exchange with lipids in the surrounding membrane. Representative fluorescence recovery of a bleached PMT-mRFP membrane region containing a DC-SIGN domain (*A*) or not containing a DC-SIGN domain (*B*), on an NIH 3T3 cell coexpressing PMT-mRFP and DC-SIGN. To

identify membrane regions containing domains, cells were stained with DC-SIGN using DCN46 and goat anti-mouse-Alexa488 secondary antibody. A montage showing the bleaching of a representative membrane region is above each recovery profile. The area of defined photobleaching is indicated by the yellow circle. Images prior to photobleaching ($t \approx -0.38$ and -0.19 s) are shown on the left of the blue arrow, which indicates the first image directly following the time of photobleaching ($t \approx 0$ s); images following photobleaching are shown to the right of the arrow ($t \approx 3.8$ and 9.4 s). For the experiment in a membrane region containing a DC-SIGN domain (*A*), the first image in the montage is the same area shown in the subsequent images, but this image is for DC-SIGN stained with DCN46 and anti-mouse-Alexa488 in green, while the subsequent images are for the PMT-mRFP in red. Given the definition of P(t), the plotted function is zero immediately after photobleaching. Scale bars, 500 nm. (*C*) A graph showing the average % recovery for PMT-mRFP on transfected NIH 3T3 cells in membrane domains in areas containing (*left*) or not containing (*right*) a DC-SIGN domain. Uncertainties are SEMs. Representative FRAP curves are from a single experiment, while the bar graph in Fig. 4.5 *C* represents an average for all of the measurements. While the variance in data points for individual % recovery curves can be larger than the SEM in Fig. 4.5 *C*, the SEM refers to the variance between multiple experiments (n= 8 and 18, Table 4.1). The percent recoveries from the representative curves are slightly lower than the means but they fall within one standard deviation of the means.

Figure 4.6. Intradomain mobility monitored by line-scan FCS. (*A*) A line-scan carpet, in which a single 256-pixel line is repetitively scanned (20.0 μs/pixel) on the cell

membrane of an HAb2 cell that has been stained with FC125 conjugated to Alexa488. Successive lines (~ 6 ms/line) are placed directly below the previous line. The pixel intensity is shown in heat map, with red indicating high intensity and blue indicating low intensity. There is a domain in focus centered around Column 225. (*B*) The line-scan carpet from (*A*) after alignment of the domain (to remove effects of movement of the entire domain) and removal of the effect of photobleaching (moving average subtraction). (*C*) The average apparent diffusion coefficients of columns in a domain. In this case, column 1 has been standardized to represent the left-most column of a domain in a given line-scan carpet. The average D over many domains was calculated. Line-scans were acquired on domains on HAb2 cells labeled with FC125 conjugated to Alexa488 (red line), MX-DCSIGN cells labeled with DC6 conjugated to Alexa488 (green line), or Δ35-MX-DCSIGN cells labeled with DC6 conjugated to Alexa488 (blue line). Green and blue lines are essentially superimposed. (*D*) Apparent diffusion coefficients were calculated for all columns within domains and averaged from line-scans acquired as described in (*C*). Uncertainties are SEMs.

Figure 4.7. Defined valency Qdot tracking confirms that DC-SIGN and Δ35-DCSIGN exhibit much more restricted mobility than HA within domains. Qdots bound to a single streptavidin were pre-incubated with either biotinylated anti-HA and used to label HAb2 cells, biotinylated anti-DC-SIGN and used to label MX-DCSIGN cells, biotinylated anti-DC-SIGN and used to label Δ35-MX-DCSIGN cells, or found adhered to the glass in a region without a cell present. (*A*) Representative trajectories of Qdots either bound to HA (right), DC-SIGN (top left), Δ35-DCSIGN (middle left), or

adhered to the glass (bottom left) from videos acquired at 100 Hz for 10 s. (*B*-*D*) Mean squared displacement vs. τ plots from trajectories for Qdots bound to either HA (*B*), DC-SIGN (*C*), or Δ35-DCSIGN (*D*). The best-fit line for the first 10 points from the MSD plots, which is used to calculate the D, is indicated by the straight black line in each plot. Note that the ordinate is much smaller in (*C*) and (*D*) than it is in (*B*).

4.8 SUPPLEMENTAL FIGURE LEGEND

Supplemental Figure 4.1. DC-SIGN co-localizes with other C-type lectins and Clathrin. (*A*-*C*) Ripley's-K bivariate analysis is shown as L(t)-t (black line) for two representative analyzed images for DC-SIGN with Dectin-1 (*A*), CD206 (*B*), and Clathrin light chain (LC) (*C*). When L(t)-t is between the dashed red lines (randomness confidence interval), the distribution is considered random; clustering is indicated when the L(t)-t is above the dashed red lines. (*D*) Percent co-localized area of DC-SIGN with Dectin-1, CD206, and Clathrin-LC is shown. Error bars are SEM.

TABLE 4.1

Mobility of Molecules Associated with DC-SIGN and HA Microdomains*

	FRAP			Line-scan FCS		Qdot Tracking		
	P_∞	D ($\mu m^2/s$)	n	D ($\mu m^2/s$)	n	D ($\mu m^2/s$)	R^2	n
HA	68 ± 10	0.10 ± 0.01	15	0.127 ± 0.005	31	0.103 ± 0.003	0.82	25
DC-SIGN	~ 0	~ 0	12	0.0025 ± 0.0004	35	0.003 ± 0.001	0.76	31
Δ35-DCSIGN	~ 0	~ 0	15	0.002 ± 0.001	28	0.0004 ± 0.0001	0.99	19
PMT-mRFP (non-domain)	76 ± 6	1.8 ± 0.2	8					
PMT-mRFP in DC-SIGN domains	69 ± 3	1.7 ± 0.2	18					

*Uncertainties are standard deviations of the means. The parameter n is the number of trials.

FIGURE 4.1

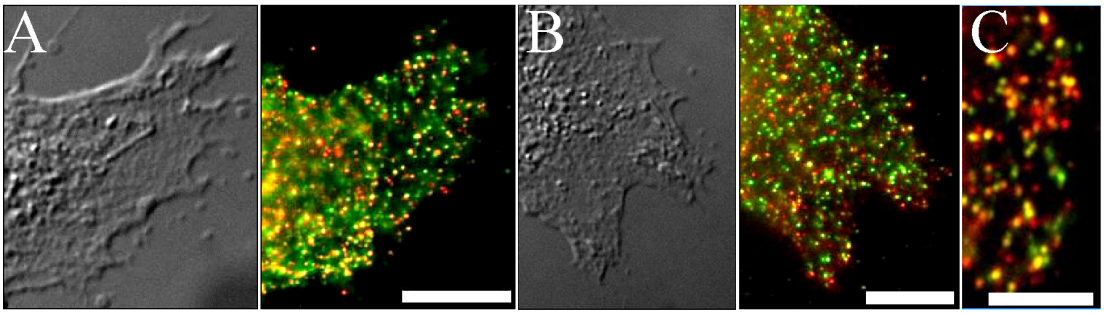

FIGURE 4.2

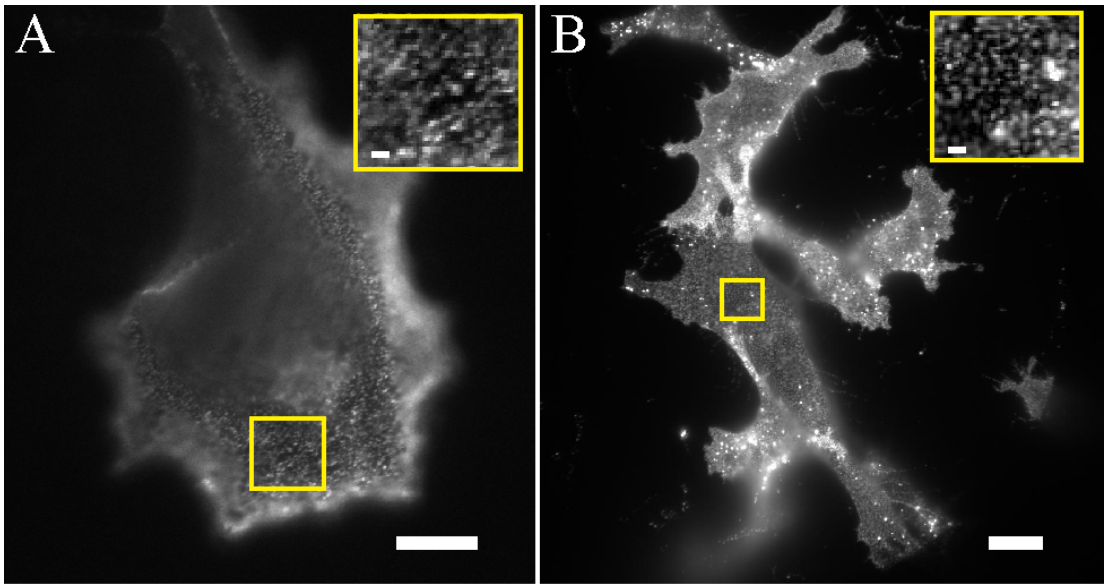

FIGURE 4.3

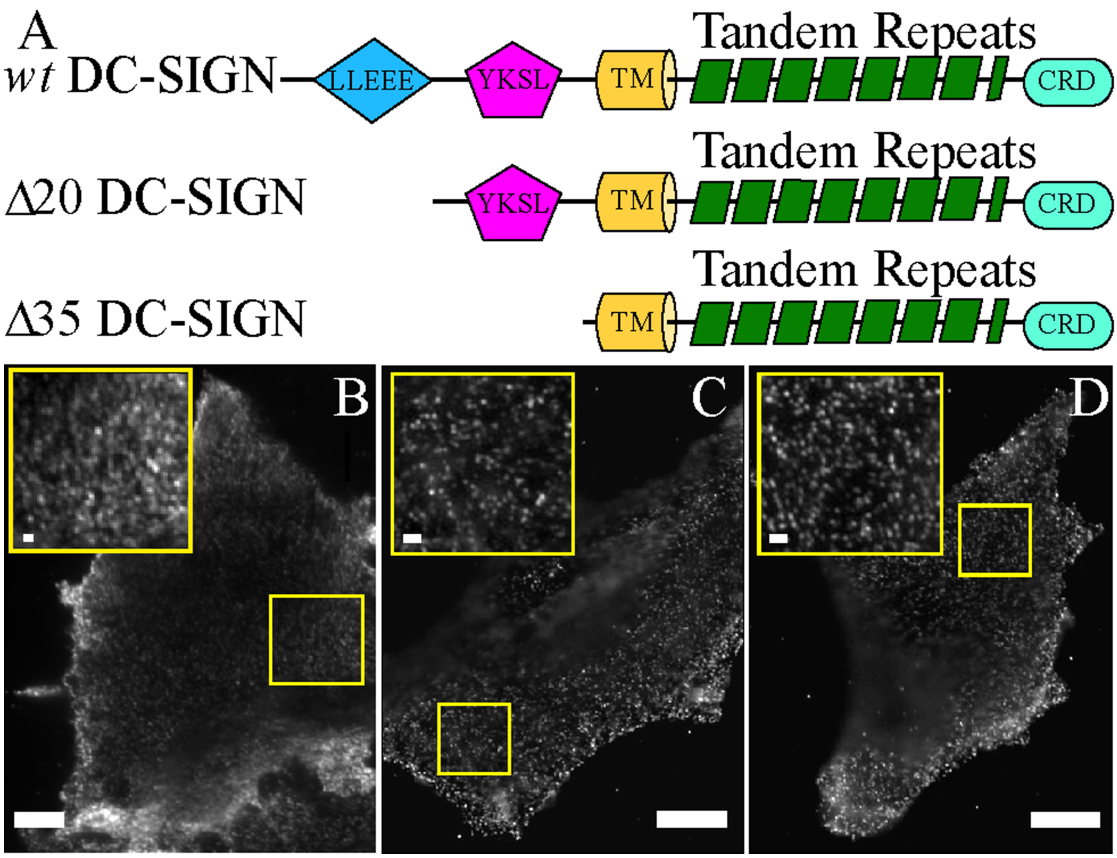
A
wt DC-SIGN
LLEEE
YKSL
TM
Tandem Repeats
CRD
Δ20 DC-SIGN
YKSL
TM
Tandem Repeats
CRD
Δ35 DC-SIGN
TM
Tandem Repeats
CRD
B
C
D

FIGURE 4.4

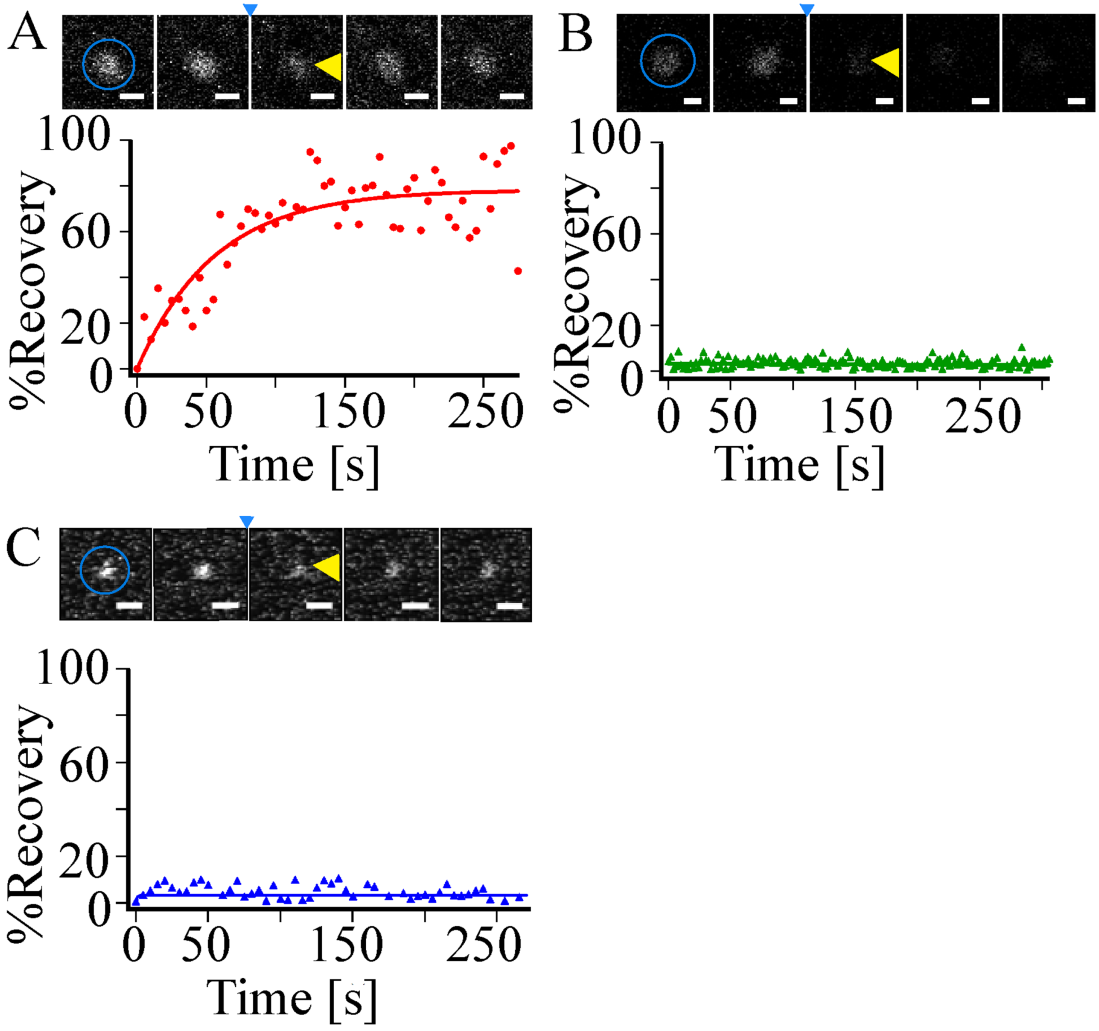

FIGURE 4.5

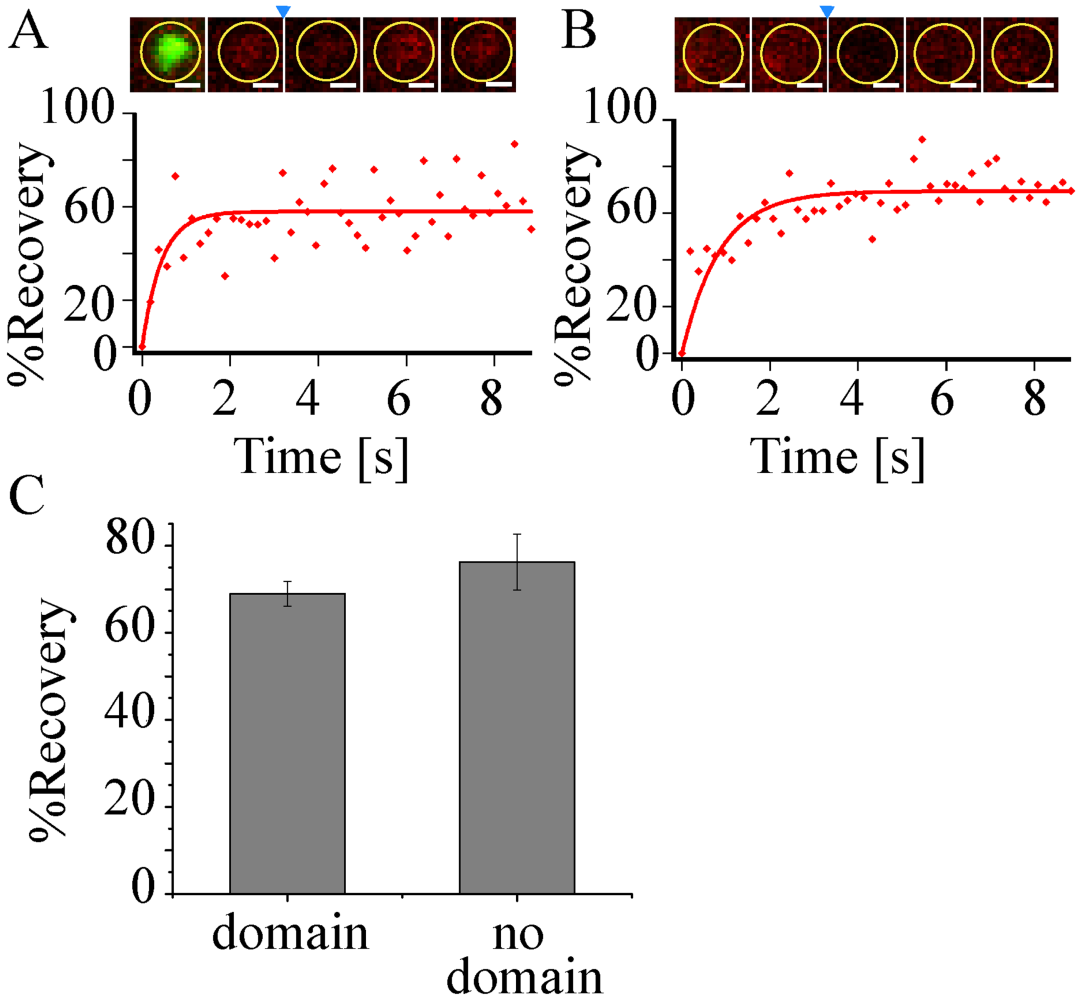
A
B
100
60
20
0
%Recovery
0
2
4
6
8
Time [s]
C
80
60
40
20
0
%Recovery
domain
no domain

FIGURE 4.6

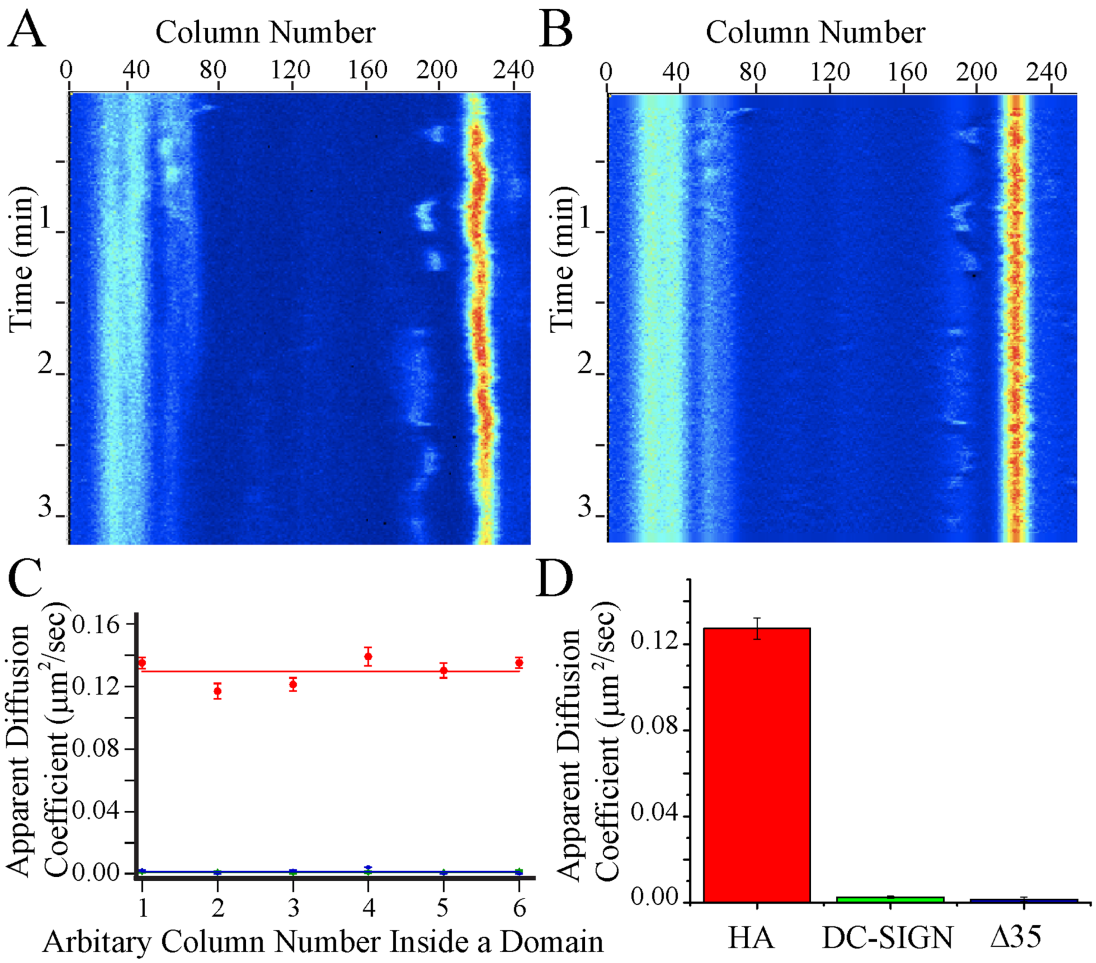
A
Column Number
0
40
80
120
160
200
240
Time (min)
1
2
3
B
Column Number
0
40
80
120
160
200
240
Time (min)
1
2
3
C
Apparent Diffusion Coefficient (μm²/sec)
0.16
0.12
0.08
0.04
0.00
1
2
3
4
5
6
Arbitary Column Number Inside a Domain
D
Apparent Diffusion Coefficient (μm²/sec)
0.12
0.08
0.04
0.00
HA
DC-SIGN
Δ35

FIGURE 4.7

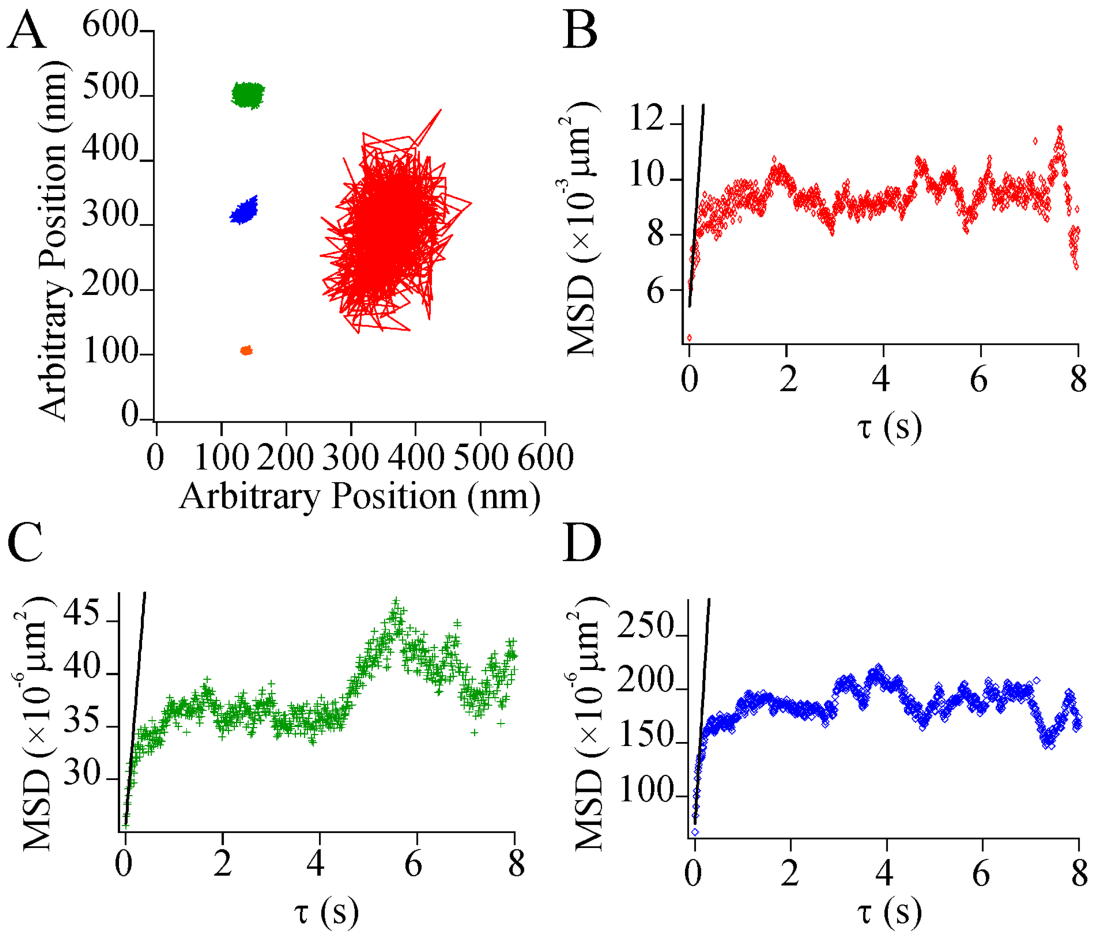
A
600
500
400
300
200
100
0
Arbitrary Position (nm)
0 100 200 300 400 500 600
Arbitrary Position (nm)
B
12
10
8
6
MSD (×10-3 µm2)
0 2 4 6 8
τ (s)
C
45
40
35
30
MSD (×10-6 µm2)
0 2 4 6 8
τ (s)
D
250
200
150
100
MSD (×10-6 µm2)
0 2 4 6 8
τ (s)

SUPPLEMENTAL FIGURE 4.1

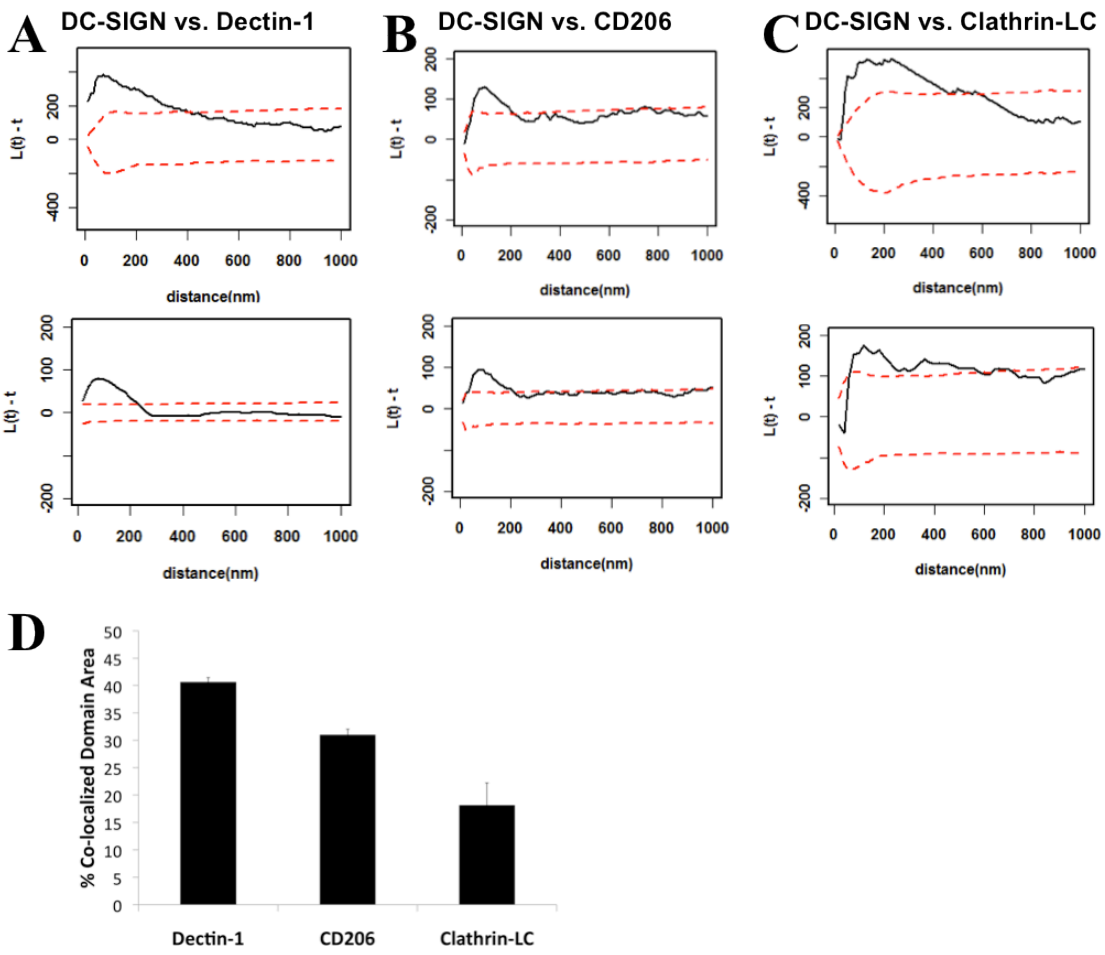

4.9 REFERENCES

1. Banchereau, J., and R. M. Steinman. 1998. Dendritic cells and the control of immunity. Nature 392:245-252.

2. Weis, W. I., M. E. Taylor, and K. Drickamer. 1998. The C-type lectin superfamily in the immune system. Immunological Reviews 163:19-34.

3. Cambi, A., M. Koopman, and C. G. Figdor. 2005. How C-type lectins detect pathogens. Cellular Microbiology 7:481-488.

4. Svajger, U., M. Anderluh, M. Jeras, and N. Obermajer. 2010. C-type lectin DC-SIGN: an adhesion, signalling and antigen-uptake molecule that guides dendritic cells in immunity. Cell Signal 22:1397-1405.

5. Feinberg, H., Y. Guo, D. A. Mitchell, K. Drickamer, and W. I. Weis. 2005. Extended neck regions stabilize tetramers of the receptors DC-SIGN and DC-SIGNR. J Biol Chem 280:1327-1335.

6. Serrano-Gomez, D., E. Sierra-Filardi, R. T. Martinez-Nunez, E. Caparros, R. Delgado, M. A. Munoz-Fernandez, M. A. Abad, J. Jimenez-Barbero, M. Leal, and A. L. Corbi. 2008. Structural requirements for multimerization of the pathogen receptor dendritic cell-specific ICAM3-grabbing non-integrin (CD209) on the cell surface. J Biol Chem 283:3889-3903.

7. Yu, Q. D., A. P. Oldring, A. S. Powlesland, C. K. Tso, C. Yang, K. Drickamer, and M. E. Taylor. 2009. Autonomous tetramerization domains in the glycan-binding receptors DC-SIGN and DC-SIGNR. J Mol Biol 387:1075-1080.

8. Cambi, A., F. de Lange, N. M. van Maarseveen, M. Nijhuis, B. Joosten, E. M. van Dijk, B. I. de Bakker, J. A. Fransen, P. H. Bovee-Geurts, F. N. van Leeuwen, N. F. Van Hulst, and C. G. Figdor. 2004. Microdomains of the C-type lectin DC-SIGN are portals for virus entry into dendritic cells. J Cell Biol 164:145-155.

9. de Bakker, B. I., F. de Lange, A. Cambi, J. P. Korterik, E. M. van Dijk, N. F. van Hulst, C. G. Figdor, and M. F. Garcia-Parajo. 2007. Nanoscale organization of the pathogen receptor DC-SIGN mapped by single-molecule high-resolution fluorescence microscopy. Chemphyschem 8:1473-1480.

10. Koopman, M., A. Cambi, B. I. de Bakker, B. Joosten, C. G. Figdor, N. F. van Hulst, and M. F. Garcia-Parajo. 2004. Near-field scanning optical microscopy in liquid for high resolution single molecule detection on dendritic cells. FEBS Letters 573:6-10.

11. Neumann, A. K., N. L. Thompson, and K. Jacobson. 2008. Distribution and lateral mobility of DC-SIGN on immature dendritic cells--implications for pathogen uptake. J Cell Sci 121:634-643.

12. Wu, L., T. D. Martin, R. Vazeux, D. Unutmaz, and V. N. KewalRamani. 2002. Functional evaluatoin of DC-SIGN monoclonal antibodies reveals DC-SIGN interactions with ICAM-3 do not promote Human Immunodeficiency Virus Type 1 transmission. Journal of Virology 76:5905-5914.

13. Chapple, J. P., A. J. Hardcastle, C. Grayson, K. R. Willison, and M. E. Cheetham. 2002. Delineation of the plasma membrane targeting domain of the X-linked retinitis pigmentosa protein RP2. Invest Ophthalmol Vis Sci 43:2015-2020.

14. Liu, P., T. Sudhaharan, R. M. Koh, L. C. Hwang, S. Ahmed, I. N. Maruyama, and T. Wohland. 2007. Investigation of the dimerization of proteins from the epidermal growth factor receptor family by single wavelength fluorescence cross-correlation spectroscopy. Biophys J 93:684-698.

15. Baribaud, F., S. Pohlmann, T. Sparwasser, M. T. Kimata, Y. K. Choi, B. S. Haggarty, N. Ahmad, T. Macfarlan, T. G. Edwards, G. J. Leslie, J. Arnason, T. A. Reinhart, J. T. Kimata, D. R. Littman, J. A. Hoxie, and R. W. Doms. 2001. Functional and antigenic characterization of human, rhesus macaque, pigtailed macaque, and murine DC-SIGN. J Virol 75:10281-10289.

16. Braciale, T. J., M. E. Andrew, and V. L. Braciale. 1981. Simultaneous expression of H-2-restricted and alloreactive recognition by a cloned line of influenza virus-specific cytotoxic T lymphocytes. J Exp Med 153:1371-1376.

17. Zhang, J., K. Leiderman, J. R. Pfeiffer, B. S. Wilson, J. M. Oliver, and S. L. Steinberg. 2006. Characterizing the topography of membrane receptors and signaling molecules from spatial patterns obtained using nanometer-scale electron-dense probes and electron microscopy. Micron 37:14-34.

18. Dorsch, S., K. N. Klotz, S. Engelhardt, M. J. Lohse, and M. Bunemann. 2009. Analysis of receptor oligomerization by FRAP microscopy. Nat Methods 6:225-230.

19. Kang, M., C. A. Day, K. Drake, A. K. Kenworthy, and E. DiBenedetto. 2009. A generalization of theory for two-dimensional fluorescence recovery after photobleaching applicable to confocal laser scanning microscopes. Biophys J 97:1501-1511.

20. Gruber, A., A. S. Chalmers, S. Popov, and R. M. Ruprecht. 2002. Functional aspects of binding of monoclonal antibody DCN46 to DC-SIGN on dendritic cells. Immunol Lett 84:103-108.

21. Digman, M. A., C. M. Brown, P. Sengupta, P. W. Wiseman, A. R. Horowitz, and E. Gratton. 2005. Measuring fast dynamics in solutions and cells with a laser scanning microscope. Biophysical Journal 89:1317-1327.

22. Petrasek, Z., and P. Schwille. 2008. Precise measurement of diffusion coefficients using scanning fluorescence correlation spectroscopy. Biophys J 94:1437-1448.

23. Ries, J., S. Chiantia, and P. Schwille. 2009. Accurate determination of membrane dynamics with line-scan FCS. Biophysical Journal 96:1999-2008.

24. Sperling, R. A., T. Pellegrino, J. K. Li, W. H. Chang, and W. J. Parak. 2006. Electrophoretic separation of nanoparticles with a discrete number of functional groups. Adv Funct Mater 16:943-948.

25. Lin, C.-A. J., R. A. Sperling, J. K. Li, Z.-Y. Yang, P.-Y. Li, M. Zanella, W. H. Chang, and W. J. Parak. 2008. Design of an amphiphilic polymer for nanoparticle coating and functionalization. Small 4:334-341.

26. Sperling, R. A., T. Liedl, S. Duhr, S. Kudera, M. Zanella, C.-A. J. Lin, W. H. Chang, D. Braun, and W. J. Parak. 2007. Size determination of (bio-) conjugated water-soluble colloidal nanoparticles - a comparison of different techniques. J Phys Chem C 111:11552-11559.

27. Dietrich, C., B. Yang, T. Fujiwara, A. Kusumi, and K. Jacobson. 2002. Relationship of lipid rafts to transient confinement zones detected by single particle tracking. Biophys J 82:274-284.

28. Cambi, A., I. Beeren, B. Joosten, and J. A. Fransen. 2009. The C-type lectin DC-SIGN internalizes soluble antigens and HIV-1 virions *via* a clathrin-dependent mechanism. European Journal of Immunology 39:1923-1928.

29. Gamblin, S. J., and J. J. Skehel. 2010. Influenza hemagglutinin and neuraminidase membrane glycoproteins. J Biol Chem 285:28403-28409.

30. Takeda, M., G. P. Leser, C. J. Russell, and R. A. Lamb. 2003. Influenza virus hemagglutinin concentrates in lipid raft microdomains for efficient viral fusion. Proceedings of the National Academy of Sciences of the United States of America 100:14610-14617.

31. Leser, G. P., and R. A. Lamb. 2005. Influenza virus assembly and budding in raft-derived microdomains: a quantitative analysis of the surface distribution of HA, NA and M2 proteins. Virology 342:215-227.

32. Hess, S. T., M. Kumar, A. Verma, J. Farrington, A. Kenworthy, and J. Zimmerberg. 2005. Quantitative electron microscopy and fluorescence spectroscopy of the membrane distribution of influenza hemagglutinin. The Journal of Cell Biology 169:12.

33. Hess, S. T., T. J. Gould, M. V. Gudheti, S. A. Maas, K. D. Mills, and J. Zimmerberg. 2007. Dynamic clustered distribution of hemagglutinin resolved at 40 nm in living cell membranes discriminates between raft theories. Proceedings of the National Academy of Sciences of the United States of America 104:17370-17375.

34. Ellens, H., J. Bentz, D. Mason, F. Zhang, and J. M. White. 1990. Fusion of influenze hemagglutinin-expressing fibroblasts with glycophorin-bearing lipsomes: role of hemagglutinin surface density. Biochemistry 29:9697-9707.

35. Shvartsman, D. E., M. Kotler, R. D. Tall, M. G. Roth, and Y. I. Henis. 2003. Differently anchored influenza hemagglutinin mutants display distinct interaction dynamics with mutual rafts. The Journal of Cell Biology 163:879-888.

36. Engel, S., S. Scolari, B. Thaa, N. Krebs, T. Korte, A. Herrmann, and M. Veit. 2010. FLIM-FRET and FRAP reveal association of influenza virus haemagglutinin with membrane rafts. Biochem J 425:567-573.

37. Pinaud, F., X. Michalet, G. Iyer, E. Margeat, H. P. Moore, and S. Weiss. 2009. Dynamic partitioning of a glycosyl-phosphatidylinositol-anchored protein in glycosphingolipid-rich microdomains imaged by single-quantum dot tracking. Traffic 10:691-712.

38. Zhang, L., and S. Granick. 2005. Lipid diffusion compared in outer and inner leaflets of planar supported bilayers. J Chem Phys 123:211104.

39. Heinsbroek, S. E., P. R. Taylor, F. O. Martinez, L. Martinez-Pomares, G. D. Brown, and S. Gordon. 2008. Stage-specific sampling by pattern recognition receptors during Candida albicans phagocytosis. PLoS Pathog 4:e1000218.

40. Neumann, A. K., and K. Jacobson. 2010. A novel pseudopodial component of the dendritic cell anti-fungal response: the fungipod. PLoS Pathog 6:e1000760.

41. Hemler, M. E. 2005. Tetraspanin functions and associated microdomains. Nat Rev Mol Cell Biol 6:801-811.

42. Grigorian, A., S. Torossian, and M. Demetriou. 2009. T-cell growth, cell surface organization, and the galectin-glycoprotein lattice. Immunol Rev 230:232-246.

CHAPTER 5

Super-Resolution Imaging of C-Type Lectin and Influenza Hemagglutinin Nanodomains on Plasma Membranes using Blink Microscopy[1]

5.1 SUMMARY

Dendritic cells express DC-SIGN, a C-type lectin (CTL) that binds a variety of pathogens and facilitates their uptake for subsequent antigen presentation. DC-SIGN forms remarkably stable microdomains on the plasma membrane. However, inner leaflet lipid markers are able to diffuse through these microdomains suggesting that, rather than being densely packed with DC-SIGN proteins, an elemental substructure exists. Therefore, a super-resolution imaging technique, Blink Microscopy (Blink), was applied to further investigate the lateral distribution of DC-SIGN. Blink indicates that DC-SIGN, another CTL (CD206), and influenza hemagglutinin (HA) are all localized in small (~80 nm in diameter) nanodomains. DC-SIGN and CD206 nanodomains are randomly distributed on the plasma

[1] Reproduced/adapted with permission from:
Itano MS, Steinhauer C, Schmied J, Forthmann C, Liu P, Neumann AK, Thompson NL, Tinnefeld P, Jacobson K, 2012. ***Super-resolution imaging of C-type lectin and influenza hemagglutinin nanodomains on plasma membranes using Blink Microscopy***, Biophysical Journal, **102**(7):1534-52.
doi: 10.1016/j.bpj.2012.02.022

Michelle S. Itano contributed to all of the Figures in the manuscript, and also was the primary contributor to the overall organization, writing and editing of this manuscript. Christian Steinhauer contributed to Figure 5.1. Jürgen Schmied contributed to Figure 5.3. Carsten Forthmann contributed to Supplemental Figure 5.3. Christian Steinhauer, Jürgen Schmied, and Carsten Forthmann also contributed to the image acquisition and the development of programs for image analysis.

membrane whereas HA nanodomains cluster on length scales up to several microns. We estimate, as a lower limit, that DC-SIGN and HA nanodomains contain on average two tetramers or two trimers, respectively, while CD206 is often non-oligomerized. Two-color Blink determined that different CTLs rarely occupy the same nanodomain although they appear co-localized using widefield microscopy. A novel domain structure emerges in which elemental nanodomains, potentially capable of binding viruses, are organized in a random fashion; evidently, these nanodomains can be clustered into larger microdomains that act as receptor platforms for larger pathogens like yeasts.

5.2 INTRODUCTION

Immature dendritic cells are professional antigen presenting cells that mediate innate and adaptive immune responses by first detecting and binding to a large variety of pathogens [1, 2]. This antigen recognition is driven by interactions of pathogens with specialized receptors, highly expressed on the surface of dendritic cells, which recognize pathogen associated molecular patterns. C-type lectins (CTLs) are one such family of receptors, which recognize carbohydrate epitopes on the surface of many pathogens [3]. One CTL, DC-SIGN (dendritic cell-specific intercellular adhesion molecule-3-grabbing non-integrin), also called CD209, is a type II membrane protein that binds to a large range of clinically relevant pathogens, including HIV, Ebola virus, *Candida albicans*, and *Leishmania* [4]. DC-SIGN is expressed in microdomains on the surfaces of dendritic cells and when ectopically expressed in fibroblasts and other cell types [5-9]. Furthermore, *in vitro* studies indicate that DC-SIGN is most probably present as a tetramer on the plasma membrane [10-16]. Recognition of and binding to pathogens by DC-SIGN appears to require that the presumed DC-SIGN tetramers, or at least DC-SIGN as a monomer, be clustered on the plasma membrane [5].

DC-SIGN forms clusters on the cell surface even in the absence of exogenous ligands and these clusters enable DC-SIGN to bind to pathogens ranging in size from viruses (typically 80-100 nm in diameter) to yeast particles (several microns in diameter). In fact, previous measurements using wide-field microscopy methods have indicated that DC-SIGN microdomains both on human immature dendritic cells and on fibroblasts ectopically expressing DC-SIGN range in size from that detectable by classical optical resolution (≈300

nm) to ~1.5 μm in dimension [8]. Other work, using transmission electron microscopy (TEM) and near-field scanning optical microscopy (NSOM), has indicated that DC-SIGN clusters are generally less than 200 nm in diameter [5-7]. Recent results using several complementary fluorescence imaging-based techniques to measure the lateral dynamics of DC-SIGN microdomains indicated that these microdomains are remarkably stable [8, 9]. However, fluorescence recovery after photobleaching experiments determined that lipids can permeate and diffuse through DC-SIGN microdomains [9], suggesting that, rather than being densely packed with DC-SIGN proteins, there may be a complex internal structure to DC-SIGN microdomains that are viewed as continuous structures using wide-field fluorescence microscopy. Throughout this paper, we will refer to domains observable by wide-field fluorescence microscopy, having a resolution limit of ~300 nm, as "microdomains", while domain structures with dimension ~100 nm or less, which are only observable by super-resolution methods, will be referred to as "nanodomains".

The studies reported in this paper describe results obtained by using a super-resolution imaging technique, Blink Microscopy (Blink), to examine the nanostructure of DC-SIGN microdomains on fixed dendritic cells. Blink Microscopy is one of several recently developed methods that use sequential, sparsely distributed single-molecule imaging to generate plots of precise locations of single molecules, with a resolution of ~30 nm [17]. This method employs oxidation and reduction agents to drive the majority of the dyes into transient dark states, with only a few sparsely-distributed dyes fluorescing, with ms-long on times, at a time. Blink offers several advantages for biological applications as it permits the use of commercial dyes (and therefore doesn't require over-expression of a fluorescent

protein fusion), it utilizes fast (<60 seconds) times for image acquisition (2-4000 frames at 30 ms integration times), and is experimentally simple to set-up (requiring only the use of standard immunostaining practices and the exchange of soluble buffers). However, as with many of the other super-resolution imaging methods, Blink is most effective when imaging fixed cells using total internal reflection fluorescence (TIRF) microscopy, and therefore can be most easily applied to image proteins at or very near the ventral cell surface or coverslip.

For comparative purposes, the distribution of DC-SIGN at sub-optical resolution was complemented by observations of another protein, influenza hemaggultinin (HA). HA is located in the viral envelope, but also forms plasma membrane microdomains when ectopically expressed in non-infected cells. The propensity for HA to form microdomains on plasma membranes is presumably related to subsequent viral budding [18, 19]. Analysis of Blink images determined that DC-SIGN and HA are predominantly expressed in small nanodomains, ~80 nm in diameter. However, while statistical analyses demonstrated that DC-SIGN nanodomains are randomly distributed on dendritic cell surfaces, the same analyses indicated that HA nanodomains are not randomly distributed on NIH 3T3 HAb2 cell surfaces at length scales up to and beyond 1 μm. Finally, the number of Blink localizations per nanodomain indicated that DC-SIGN and HA nanodomains generally contain fewer than 12 molecules, suggesting that these nanodomains are not densely packed with DC-SIGN or HA molecules, respectively, leaving room for other protein and lipid components.

To determine whether the spatial arrangement of DC-SIGN is representative of other members of the CTL family of proteins, Blink was applied to investigate the lateral

distribution of another CTL family member, CD206. Analysis of Blink images indicated that, similar to DC-SIGN, CD206 is also generally expressed in randomly distributed, small (<80 nm in diameter) nanodomains. However, CD206 nanodomains appear to contain fewer molecules on average than DC-SIGN and HA nanodomains. Further, two-color Blink imaging determined that different CTLs (DC-SIGN and CD206) are generally confined to separate nanodomains and rarely co-exist within the same nanodomain, though when viewed by widefield microscopy they appear to be co-localized.

Overall, the results reported here indicate that there is a lateral organization of nanodomains within DC-SIGN and CD206 microdomains, which cannot be resolved by wide-field fluorescence microscopy; give a considerable amount of quantitative insight with respect to this complexity; and raise key questions concerning structure-function relationships for certain classes of membrane receptor clusters.

5.3 MATERIALS & METHODS

Cells

Human monocyte-derived immature dendritic cells were prepared from human whole blood obtained from the New York Blood Center (Long Island City, NY) as previously described [8, 9]. Peripheral blood mononuclear cells were isolated from the blood by centrifuging over a Ficoll gradient (Ficoll-Paque PLUS, GE Healthcare, Uppsala, Sweden) and resuspended in Dulbecco's phosphate-buffered saline (DPBS, 0.08 M sodium phosphate, 0.14 M NaCl, pH 7.4, GIBCO, Grand Island, NY) with 0.5 % (w/v) bovine serum albumin

(BSA, Santa Cruz Biotechnology, Santa Cruz, CA). Monocytes were culled from the peripheral mononuclear cells by adherence to tissue culture flasks for 2-3 hours followed by washing with RPMI-1640 medium containing 10% fetal bovine serum (FBS). After approximately 24 hours detached cells were replated on LabTek 8-well chambered cover slides (cat# 177402, Nunc, Rochester, NY) with RPMI-1640, 10 % FBS, 500 U/ml of human IL-4 and 800 U/ml of human GM-CSF (Peprotech, Rocky Hill, NJ) to stimulate development of immature dendritic cells. An NIH 3T3 cell line (called HAb2) that permanently expresses HA from the Japan strain of influenza was obtained from Judith White (University of Virginia, Charlottesville, VA). These cells were maintained in culture using high glucose DMEM with 10 % FBS.

Antibodies

For single-color Blink measurements, two primary antibodies were prepared in-house. The mouse hybridoma DC6, which secretes IgG1 specific for human DC-SIGN [20], was a gift of Robert Doms (University of Pennsylvania, Philadelphia, PA). The mouse hybridoma FC125, which secretes IgG2a specific for human HA [21], was obtained from Thomas Braciale (University of Virginia). In both cases, hybridomas were grown in PFHM-II protein-free hybridoma medium (GIBCO). DC6 and FC125 IgG were purified from hybridoma supernatants by Protein A affinity chromatography (Pierce Biotechnology, Rockford, IL). The column was sequentially washed with 100 mM and 10 mM Tris at pH 8.0 and eluted with 50 mM glycine at pH 3.0. Eluates (1-4 ml) were immediately neutralized with 1 M Tris (pH 8.0), concentrated by using spin columns (Ultracel-10k; Millipore, Billerica, MA) and dialyzed with Slide-A-Lyzer cassettes (Pierce Biotechnology) against 4 L

PBS (diluted from PBS, 10×, Cellgro, Manassas, VA). The goat polyclonal IgG AF2534, which is specific for human CD206 (also known as MMR, Macrophage Mannose Receptor), was obtained commercially (R&D Systems, Minneapolis, MN). Commercially available goat anti-mouse Fab (Rockland, #810-1102, Hamburg, Germany) and rabbit anti-goat Fab (Rockland, #305-4102) were used as secondary antibodies. These Fabs were labeled with ATTO655-NHS (ATTO-TEC, Siegen, Germany) in PBS (pH 8) for 3 hours at room temperature. Excess dye was removed by a NAP-5 size exclusion column (GE Lifesciences, Munich, Germany). The degree-of-labeling was determined to be ~1 dye/protein by absorption spectroscopy. By using single-step photobleaching experiments, we estimated that fluorescently labeled Fabs contained approximately 1-2 fluorophores per protein (mean = 1.4, max = 3, n = 46; Supporting Figure 4.2). For the two-color Blink measurements, the primary antibodies were the mouse monoclonal IgG DCN46, specific for human DC-SIGN (R&D Systems) and AF2534. The secondary antibodies were Alexa546-conjugated donkey anti-mouse IgG (Invitrogen, Carlsbad, CA) and ATTO655-conjugated rabbit anti-goat Fab (see above).

Sample Preparation

Cells were initially plated on LabTek 8-well chamber cover slides (Nunc) in the appropriate medium. Cells were then fixed by using a paraformaldehyde solution [4 % (v/v) in PBS, pH 7.4] for 20 minutes at 25°C and then maintained in PBS/BSA overnight at 4°C. All subsequent steps were carried out at room temperature. On the day of Blink measurements using a single color, cells were treated with the appropriate primary IgG (DC6, AF2534 or FC125) at 10 μg/mL in PBS/BSA for 20 min, washed with PBS/BSA,

stained with the appropriate ATTO655-Fab as the secondary antibody at 0.5 μg/mL in PBS/BSA for 15 min, and then washed with PBS/BSA. On the day of two-color Blink measurements, cells were first treated AF2534 at 50 μg/mL in PBS/BSA for 20 min, washed with PBS/BSA, stained with rabbit-anti-goat ATTO655-Fab at 0.5 μg/mL in PBS/BSA for 15 min, and then washed extensively with PBS/BSA. The cells were then treated with DCN46 at 10 μg/mL in PBS/BSA for 20 min, washed with PBS/BSA, stained with donkey-anti-mouse Alexa546 IgG at 0.5 μg/mL in PBS/BSA for 15 min, and then washed with PBS/BSA.

For these conditions, dendritic cells were most likely saturated with primary and secondary antibodies. This conclusion is derived from measurements in which it was determined that a region of interest (ROI) imaged under constant imaging conditions with varied concentrations of primary and secondary antibody had reached maximum fluorescence intensity. The antibody concentrations were selected to be the minimum dilution that achieved the maximum fluorescence intensity of the ROI.

Blink Microscopy

Fluorescence imaging was carried out on an Olympus IX-71 applying an objective-type total internal reflection fluorescence (TIRF) configuration with an oil-immersion objective (PlanApo N 100×, NA 1.40, Olympus). For illumination, a high power single mode diode laser (λ = 650 nm, XTL, Toptica Photonics, Munich, Germany) was used, illuminating an area of about twice the size of the observation area (~3000 μm^2). The focal length of the focusing lens was 100 mm. Prior to passing through the focusing lens, the Gaussian profile

beam was expanded to ~ 1 cm in diameter. The laser beam was passed through a clean-up filter (Brightline HC 650/13, AHF Analysentechnik, Tuebingen, Germany) and coupled into the microscope objective by a dual-band beamsplitter (z532/658 rpc, AHF Analysentechnik). Fluorescence was spectrally filtered with an emission filter (HQ 700/75 M, AHF Analysentechnik) and imaged on an EMCCD camera (Ixon DU-897, Andor Technology, Belfast, Northern Ireland). For two-color experiments, a second high power single mode diode laser (λ = 532 nm, MPB Communications, Montreal, Canada) was used and imaged by a second Ixon DU-892 EMCCD camera (Andor). The green laser beam was passed through a clean-up filter (HC Laser Clean-up MaxLine 532/2, AHF Analysentechnik) and coupled into the microscope objective by a dual-band beamsplitter (z532/658 rpc, AHF Analysentechnik). Green fluorescence was spectrally filtered with an emission filter (HQ 582/75 M, AHF Analysentechnik).

Cells labeled with primary and secondary antibodies were imaged in PBS containing both 50-100 μM ascorbic acid (AA) and 0-75 μM N,N-methylviologen (MV). AA and MV concentrations were adjusted to gain sufficient localizations within 20 seconds; within this time mechanical drift is not significant (see [22] for details of how to adjust blinking for super-resolution microscopy). The typical laser power used for imaging was 200 mW (5 kW/cm^2 at the specimen plane). 2000–6000 frames were recorded at frame rates of 111-250 Hz. The laser powers were chosen to adapt the on-times of the fluorophores to the shortest possible integration time of about 4 ms of the EMCCD camera. Under these conditions, ATTO655 emits approximately 1000 photons per on-time [23]. This level of emission provides a S/N ratio of about 30 before background subtraction. For the two-color

experiments, the red and green images were acquired sequentially; first the red (ATTO655) image was acquired, and then the green (Alexa546) image was acquired. This method was implemented to reduce excitation by the green laser in the red channel. For two color images, the images were aligned for offset due to chromatic effects by imaging sparsely distributed beads fluorescent in both channels (40 nm Transfluor, Invitrogen) on glass prior to imaging cells on each day of image acquisition. To optimize the blinking of both fluorophores for two-color measurements, some cells were imaged in an alternative solution that achieved oxygen removal enzymatically (2% glucose in PBS with 50 μg/ml glucose oxidase, 100-200 μg/ml catalase, 0.1 mM TCEP-HCl (Sigma)) and contained 1- 50 mM cysteamine (MEA, Sigma) as a reducing agent.

Single-step photobleaching

Samples were prepared as for Blink Microscopy, except that cells were imaged in PBS without any other reagents added. The laser intensity was set to moderate power and 1000-2000 frames were recorded with an integration time of 100 ms until all fluorophores were bleached.

Image Reconstruction

Movies were analyzed by custom-made software written in LabView 2009 (National Instruments, Austin, TX) as in [22]. The first frames of movies were discarded because in the beginning all molecules are in the active state. The algorithm analyzes the movie frame by frame, and each local peak intensity within a frame is compared with its environment. When the peak intensity is at least 1.4 times higher than its environment, the spot is considered for

further analysis. This threshold automatically adapts to the background level in the immediate environment of the molecule under consideration. Two-dimensional Gaussian fitting yields the position of the molecules that are histogrammed for image reconstruction. To further exclude events with two molecules being simultaneously active within a diffraction-limited area and to remove cases when the two-dimensional Gaussian fitting does not converge, a circularity criterion of the identified spots has to be met. Specifically, this means that the ratio of the width of the Gaussian fit in the x-dimension vs. the y-dimension must be less than 1.2. To construct a super-resolution image from the localizations, each pixel of the original image was divided into 5 super-resolution pixels, resulting in a 20 nm pixel size in the Blink image.

Localization precision

For Blink Microscopy images, the localization precision is mainly determined by the on-counts, or the number of photons (N) per on-time [24]. The localization precision is expected to be on the order of $\sim s/(N^{1/2}) = 22$ nm, where s represents the standard deviation of the center of the point-spread-function. This value translates to a full-width half-maximum (FWHM) of ~50 nm for a single molecule being localized multiple times. Experimentally, the localization precision was determined by imaging ATTO655-Fab secondary antibodies adhered to glass. Accordingly, single molecules are localized with a FWHM = 39 nm (Table 5.1, Fig. 5.4).

Convolution of Blink images

To compare the distribution of Blink localizations with an image of the same area of the cell with standard TIRF illumination, the Blink image was convoluted with a diffraction-limited point-spread function (PSF). First, ImageJ was used to define an appropriate diffraction-limited PSF using the 'Diffraction PSF 3D' plugin (OptiNav, Inc., Bellevue, WA) and the relevant information for the microscope used to acquire the Blink movies (described above). The PSF had a Rayleigh's criterion of ~14 pixels, or ~280 nm. The image of the PSF and the Blink image were used with another ImageJ plugin, 'Convolve 3D' (OptiNav, Inc.), which convolves the Blink image with the PSF.

Nanodomain size fitting

To calculate nanodomain size, first, ImageJ was used to identify domain boundaries. For all images, peaks were identified by binarizing the image by using the 'Make Binary' routine in the software package ImageJ. Peak positions were identified using the `Analyze Particles' routine, which returned a list of centroids and a new image depicting outlines for spots meeting the condition of area $\geq$ 4 pixels. Square regions of interest (ROIs) were hand-drawn around each of the spots identified by ImageJ on the original Blink image in the Labview software. The distributions of the Blink localizations within the ROIs were then fit to two-dimensional Gaussian functions. The FWHMs were used to estimate the domain diameter. For "Overall FWHM" measurements, the FWHM from each dimension was treated as a separate measurement, so in general, there were twice as many FWHM measurements used in this calculation than the number of domains or ATTO655-Fab dyes analyzed. Very rarely (for ~1 % of the dyes), the distribution of Blink localizations for a single ATTO655-

Fab on glass was only a single pixel wide in one dimension (x- or y-). In these instances it was not possible to fit to a Gaussian in that dimension, so only one FWHM measurement was reported instead of two.

Analysis of the spatial distribution of nanodomains.

The distribution of nanodomains on the plasma membrane was analyzed using PAST [25] and CellSpan (University of New Mexico, Albuquerque, NM) software. Domain centroids for the analysis were input from the list given by the ImageJ 'Analyze Particles' routine (as in ***Nanodomain size fitting***) on Blink images that were cropped to exclude cell boundaries and space not occupied by the cell. Both Ripley's K - based statistics and a modified Hopkins function were used to compare the distributions of DC-SIGN, CD206 and HA Blink domains to that of a random distribution. The PAST program was used to run the Ripley's K test, and details regarding this software are described in [25]. In the case of the Ripley's K test, the function K(r) indicates the probability of encountering another centroid at the length scale denoted on the r-axis. For random distributions the function K(r) is proportional to the density of the centroids and πr^2. Red lines in the plots represent a 95% confidence interval for complete spatial randomness, calculated from 1000 Monte Carlo simulations of randomly distributed points for each image. Clustering is indicated at length scales where K(r) is greater than that expected due to a random distribution of points. The CellSpan program was used to run the modified Hopkin's test for spatial randomness, which compares the distances between random data points and nanodomain centroids to the actual distances between nanodomain centroids. Details of the CellSpan program and statistics used are described in [26]. A random distribution is indicated by a function that is shaped like a

normal “bell” curve centered at the Hopkin’s statistic 0.5 on the abscissa. Clustering is indicated if the plot is shifted to the right.

Simulations of Blink Microscopy images of two randomly distributed sets of clusters, in which any overlap is of a stochastic nature, were created using a custom-built Labview program. This program created images with clusters equivalent to the mean size measured for DC-SIGN and CD206 and exponential distributions of the mean number of blink localizations measured for each domain type. The clusters were randomly distributed with a density of 200 domains of each type per image with the number of blink localizations per domain determined by an exponential distribution with a mean equal to 200.

For percent co-localization analysis, the area of co-localization was determined by dividing the number of pixels that contained both red and green signal by the total number of pixels with red signal. In total, 200 simulated images and 20 two-color Blink images were analyzed.

To determine whether the co-localization was above what would be expected for two randomly distributed sets of clusters, in which any overlap is of a stochastic nature, a Ripley’s-K bivariate analysis was applied. The final domain images were cropped to exclude cell boundaries and their centroids were identified using the Particle Analyzer. The centroids were used as input for the Cellspan software (University of New Mexico, New Mexico) to perform ‘Ripley’s K for bivariate data’ analysis. Output is provided in the form of the L function, L(t)-t, as previously described [26]. This function transforms Ripley’s K function to

a form where L(t)-t=0 for random distributions at all length scales (t). When L(t)-t (black line) is within the confidence interval for randomness (i.e., between the red lines), this indicates a random distribution. L(t)-t greater than the randomness confidence interval indicates clustering on the length scales denoted on the abscissa of the graph.

5.4 RESULTS

5.4.1 Blink Microscopy on DC-SIGN Plasma Membrane Nanodomains.

DC-SIGN forms remarkably stable microdomains on the plasma membrane that range in size, as estimated from wide-field fluorescence microscopy, from the diffraction limit to ~1.5 μm in dimension [8, 9]. However, inner leaflet lipid markers are able to diffuse through these microdomains suggesting that rather than being densely packed with DC-SIGN proteins, an elemental substructure exists [9]. Therefore, a super-resolution imaging technique, Blink Microscopy [17], was applied to further investigate the lateral distribution of DC-SIGN within microdomains on the plasma membrane. Blink Microscopy achieves sub-diffraction-limited resolution by precisely localizing single molecules that are stochastically imaged in a sequential manner so that no more than one molecule is actively emitting fluorescence within the point-spread function (PSF) of the molecule [27].

Prior to antibody staining and imaging, all cells were fixed by using a paraformaldehyde solution [4 % (v/v) in PBS, pH 7.4] for 20 minutes at 25°C and then maintained in PBS/BSA overnight at 4°C. Fixed monocyte-derived immature dendritic cells were stained for DC-SIGN using indirect immunofluorescence with DC6 IgG and

ATTO655-Fab. Blink Microscopy images were generated from movies taken while the dyes were induced to blink with ms-long on-times in the presence of reducing and oxidizing agents. Specifically, cells labeled with primary and secondary antibodies were imaged in PBS containing both 50-100 μM ascorbic acid (AA) and 0-75 μM N,N-methylviologen (MV). AA and MV concentrations were adjusted to gain sufficient localizations within 20 seconds. Each point in a Blink image represents the precise location of a single molecule given by fitting the spatial distribution of the fluorescence from a single molecule to a Gaussian function. Figure 5.1 shows a representative image (one of 17 images analyzed): Figure 5.1 *A* gives the conventional TIRF image; Figure 5.1 *B* gives the Blink image; and Figure 5.1 *C* gives an overlay of the Blink image and the TIRF image. As can be readily seen by comparing Figures 5.1 *A* and *B*, Blink Microscopy provides a much higher resolution in terms of localizing centroids of DC-SIGN micro/nanodomains in the same region of the cell. For example, in some cases where a single region of fluorescence or microdomain is viewed using TIRF, the Blink image indicates that this area is actually comprised of several very small nanodomains (Fig. 5.1 *C*, inset). Additionally, the TIRF image (Fig. 5.1 *A*) and the corresponding computer-generated convolution of the Blink image to a corresponding wide-field image (Supporting Fig. 5.1) are very similar. Nonetheless, these two images are not completely identical. Most of the variation is due to differences in relative pixel intensity values between the two images, because the values in Fig. 5.1 *A* reflect actual fluorescence intensities, while the values in Supporting Fig. 5.1 were generated computationally. In addition, the number of Blink localizations within a pixel area should be, for the most part, correlated with the number of fluorophores in the area, but will also depend on the specific blinking properties during the imaging conditions (e.g., how long given fluorophores were in

the on-state), possible differences in photobleaching, and the likelihood that more than one fluorophore within the PSF at a given location is in an on-state at the same time. Furthermore, there are some areas in the TIRF image (*A*) that do not appear in either the Blink image (*B*) or the Blink image following convolution (Supporting Fig. 5.1), most likely because the TIRF image is taken at the beginning of the movie (when all fluorophores are in the on-state) but subsequently some of the fluorophores irreversibly photobleach and are not able to be detected by Blink.

5.4.2 Size Estimation of DC-SIGN Plasma Membrane Nanodomains using Blink Microscopy.

Blink Microscopy images of DC-SIGN on fixed dendritic cells stained with DC6 and anti-mouse ATTO655-Fab allowed visualization of small DC-SIGN nanodomains on the plasma membrane. To determine the range in sizes of these nanodomains, the Blink images were analyzed using ImageJ and custom-built Labview software. Nanodomains were first identified using the 'Particle Analyzer' routine in ImageJ (Fig. 5.2). The spatial distributions of Blink localizations in each nanodomain were then fit to two-dimensional Gaussian functions and the full-width half-maximum (FWHM) values of the fitted Gaussian functions were used to estimate nanodomain diameters (Fig. 5.2). The average FWHM for DC-SIGN nanodomains was 76 ± 42 nm (mean ± standard deviation (SD) for 3706 FWHM measurements, derived from 1853 nanodomains on 17 cells; Table 5.1 and Fig. 5.3). It is notable that the majority of the DC-SIGN nanodomains are smaller than 100 nm in diameter (Fig. 5.3), which is significantly less than the ~500 nm microdomain dimension observed in TIRF and epifluorescence images (Fig. 5.1 *A* and [8]). These results are consistent with those from other studies using methods with high spatial resolution, TEM and NSOM, which have

also determined that DC-SIGN is predominantly localized in domains less than 200 nm in diameter [5-7]. However, the DC-SIGN nanodomains imaged by Blink Microscopy are slightly smaller on average than those that were previously analyzed using these other techniques. For the NSOM measurements, the average DC-SIGN domain size (~100 nm) was at the lower limit of spatial resolution for this method (90-100 nm). Furthermore, the relatively large (10 nm) gold particles used for labeling antibodies for the TEM experiments may have resulted in slightly larger domain size measurements.

5.4.3 Comparison of Size Estimation of DC-SIGN Plasma Membrane Nanodomains to Those of Influenza HA and CD206, Another C-Type Lectin, using Blink Microscopy.

While the results presented thus far have primarily focused on describing the spatial distribution of DC-SIGN, work focused on describing heterogeneity on the plasma membrane and the downstream consequences of such molecular assemblies has become an issue of considerable interest. Influenza hemagglutinin (HA) domains, when HA is ectopically expressed, have been investigated by different imaging modalities [28, 29], and, therefore, it is useful to compare our results from DC-SIGN to those from HA. HA is a glycoprotein that is expressed on the envelope of influenza viruses and is required for the virus to bind to and be internalized either by target cells for infection or by immunological cells for antiviral immunity [30]. On virally infected cells, HA assembles into plasma membrane domains, presumably at sites of subsequent viral budding from the cell surface [18, 19]. When HA is ectopically expressed in fibroblasts, without other viral proteins, HA appears to accumulate into domains (ranging from 30 nm to several microns in diameter) on the plasma membrane of fixed and live cells [18, 28, 29]. Consistent with these previous

findings, Blink Microscopy on fixed HAb2 cells, an NIH 3T3 cell line that stably expresses HA, indicates that the protein is distributed in clusters on the cell surface. The size distribution of these clusters was analyzed using the same method described above for DC-SIGN. Similar to the distribution of DC-SIGN, HA is expressed in small nanodomains, the majority of which are less than 100 nm in diameter (Table 5.1 and Fig. 5.3). These nanodomains of HA were similar in dimension to the "compact clusters" described by Hess et al (2007); however, because our analysis did not include the cell margins, we did not analyze the "elongated clusters" observed earlier [28].

Additionally it is useful to compare the clustering of DC-SIGN to that of another CTL family member, CD206, to investigate whether the spatial arrangement of DC-SIGN is representative of other members of the CTL family of proteins. Previously, it was determined that CD206 was also expressed in microdomains on the plasma membrane of dendritic cells, and that these microdomains sometimes co-localized with DC-SIGN microdomains (9). Blink Microscopy on fixed dendritic cells stained with AF2534 and anti-goat ATTO655-Fab determined that CD206 is also expressed in nanodomains, which are 70 ± 41 nm in diameter (Table 5.1 and Fig. 5.3). This result suggests that other CTLs may also have a distinct nanoscale architecture.

5.4.4 Estimated Localization Precision of Blink Microscopy by Imaging Single ATTO655-Fab Molecules on Glass.

Similar to other super-resolution imaging techniques that use stochastic activation of fluorophores, each dye imaged by Blink Microscopy is typically localized multiple times (fit to Gaussian functions in multiple frames) in the final Blink image. Therefore, while the

localization precision of a single dye in a single frame depends on the number of photons collected [24], the localization precision of a single dye in a Blink image is also related to the spatial distribution of all of the Blink localizations derived from a single dye. To determine localization precision including the influence of multiple localizations of single dyes, Blink images of sparsely distributed single anti-mouse ATTO655-Fab molecules on glass were analyzed. Based on the number of bleaching steps for many individual ATTO655-Fabs, the average dye to protein ratio was determined to be 1.4 (Supporting Fig. 5.2). The average FWHM of the Gaussian fits to the distributions of Blink localizations from single ATTO655-Fabs on glass was 39 ± 11 nm (191 FWHM measurements, 97 dyes; Table 5.1). It is notable that the average FWHM measurements for DC-SIGN and HA nanodomains are significantly larger than the localization precision for a single fluorescent Fab (Fig. 5.3); therefore it is highly unlikely that the FWHM measurements of DC-SIGN are of single Fabs, and much more likely that the FWHM measurements refer to the dimensions of DC-SIGN nanodomains on the plasma membrane.

5.4.5 DC-SIGN and CD206, but Not HA, Nanodomains are Randomly Distributed on the Plasma Membrane.

Blink Microscopy provides high-resolution spatial distribution data, which allows mapping of the precise locations (or centroids) of nanodomains and makes possible discrimination between whether DC-SIGN and CD206 nanodomains are randomly or non-randomly distributed on the cell surface. Using the PAST [25] and the CellSpan [26] analysis programs, Ripley's K and modified Hopkin's tests were applied to the distributions of nanodomain centroids from Blink images that were cropped to exclude cell boundaries and areas not covered by a cell, respectively. In the case of the Ripley's K test, the PAST

program was used to calculate the function K(r), which indicates the probability of encountering another centroid at the length scale denoted on the r-axis. For random distributions the function K(r) is proportional to the density of the centroids and πr^2. Red lines in the plots represent the 95% confidence interval for complete spatial randomness calculated from 1000 Monte Carlo simulations of randomly distributed points for each image. Clustering is indicated at length scales where K(r) is greater than that expected due to a random distribution of points. Cellspan's modified Hopkin's test for spatial randomness compares the distances between random data points and nanodomain centroids to the actual distances between nanodomain centroids. A random distribution is indicated by a function that is shaped like a normal "bell" curve centered at the Hopkin's statistic 0.5 on the abscissa. Clustering is indicated if the plot is shifted to the right. For both of these analyses, the distribution of DC-SIGN and CD206 nanodomain centroids aligns closely with the expected result for a random distribution (Fig. 5.4 *A*-*F*). This finding agrees with the NSOM data [6].

Very different results were obtained when the same analysis methods were applied to centroids derived from Blink images of HA (Fig. 5.4 *G*-*I*). For every HA image analyzed (12 of 12 images), the modified Hopkin's test indicated clustering and the Ripley's K test indicated clustering of multiple nanodomains across all length scales up to 1 μm. For the Ripley's K test, clustering is indicated by the K(r) statistic being greater than the value expected for a random distribution at the length scales indicated by the values on the abscissa. The K(r) statistic for HA nanodomain centroids was consistently greater than the parabolic curve expected for a random distribution from the shortest distances measureable (~30 nm) to greater than 1 μm. In many cases, the Ripley's K test indicated clustering for

even longer distances. These results are consistent with previous analysis of the distribution of HA using electron microscopy and fluorescence photoactivation localization microscopy (FPALM) [28]. These results also indicate that the assembly and/or the maintenance of DC-SIGN and CD206 nanodomain distributions on the cell surface are regulated by distinct mechanisms from those that occur with HA nanodomains.

5.4.6 Estimated Occupancy of DC-SIGN in Single Nanodomains using Blink Microscopy.

Because the number of Blink localizations in a DC-SIGN nanodomain is, on the average, proportional to the number of molecules in the nanodomain, it is possible to estimate the occupancy of DC-SIGN in nanodomains using data derived from Blink images of DC-SIGN on fixed dendritic cells. A single molecule, in this case a single Fab, will blink with a characteristic rate, leading to an average number of Blink localizations that will be derived from a single Fab imaged with consistent experimental conditions. The average number of Blink localizations from a single Fab was 25 ± 18 (97 dyes analyzed; Table 5.1, Fig. 5.5 *A*). There is variability in the number of Blink localizations from single Fabs as different molecules may have zero, one, two or perhaps even three conjugated fluorophores (Supplemental Fig. 5.2). In addition, the blinking of each dye is a stochastic process sometimes leading to the dye having slightly longer or shorter on-times during the imaging process, leading to more or fewer blink localizations per single dye in a given blink image. Using the same laser power, camera integration time, concentrations of antibodies and analysis conditions, the average number of Blink localizations from a single DC-SIGN nanodomain was found to be 163 ± 230 (1960 nanodomains analyzed; Table 5.1, Fig. 5.5 *A*). As shown in Fig. 5.5 *A* and indicated by the large standard deviation of the measurement,

there is a large variability in the number of Blink localizations from single DC-SIGN nanodomains. The total number of Blink localizations in a single nanodomain is equal to the sum of Blink localizations from all of the single molecules in the nanodomain. Therefore, an estimate of the occupancy of DC-SIGN in single nanodomains was calculated by dividing the number of Blink localizations in a single nanodomain by the average number of Blink localizations from a single dye. The majority of both DC-SIGN and HA nanodomains contain fewer than 12 molecules (7 ± 10 and 5 ± 6, respectively) with a few nanodomains (less than 100 nm in diameter) of each type accommodating upwards of ~65 molecules (Table 5.1, Fig. 5.5 *A*). CD206 nanodomains, on the other hand, appear to contain fewer molecules on average, with a larger population of what appear to be single, non-oligomerized molecules on the cell surface (Table 5.1, Fig. 5.5 *A*). Given the average diameter of the ectodomain of a tetramer of DC-SIGN of ~8 nm [31, 32], we calculated that ~360 molecules of DC-SIGN or ~90 tetramers could fit within a nanodomain of average size (~76 nm in diameter; Table 5.1). However, we regard the nanodomain occupancy estimate as a lower limit for the following reasons: 1) a portion of the population of labeling Fabs will bind but have no dye conjugated to them; 2) whether, at saturation binding conditions for the primary antibody, every DC-SIGN can be labeled due to steric hindrance between adjacent binding antibodies; and 3) whether one bivalent primary antibody can bind two proximate DC-SIGN molecules. Nevertheless, even if the average number of DC-SIGN molecules in nanodomains was underestimated by a factor of two to three, the nanodomain would not be fully occupied by close packed DC-SIGN proteins (Fig. 5.7).

5.4.7 DC-SIGN Does Not Significantly Co-Localize with CD206 on the Nanoscale.

Wide-field fluorescence microscopy indicates that in a significant fraction of cases, Dectin-1 or CD206 co-localize with DC-SIGN on the resolution level of the light microscope [9]. Whether this result holds on the nanoscale has important implications for membrane function. It is likely that whether CTLs are separated into different elemental nanodomains and/or co-mingled in the same nanodomain will regulate their downstream signaling (i.e., either by segregating downstream enzymes and substrates or by providing coincidence of two pathways both impinging on common downstream targets). Two-color Blink Microscopy using Atto655 and Alexa546 to label the two different secondary antibody Fabs was applied to test whether DC-SIGN and CD206 are co-localized on the nanoscale (Fig. 5.6, Supplemental Fig. 5.3). To optimize the blinking of both fluorophores for two-color measurements, some cells were imaged in an alternative solution that achieved oxygen removal enzymatically (2% glucose in PBS with 50 μg/ml glucose oxidase, 100-200 μg/ml catalase, 0.1 mM TCEP-HCl (Sigma)) and contained 1- 50 mM cysteamine (MEA, Sigma) as a reducing agent. Approximately the same % co-localization is calculated for both the two-color Blink images (20 images analyzed) and for simulated images (100 images analyzed) of two overlapping randomly distributed sets of nanodomains (3.4 ± 1.9 and 1.9 ± 0.1 %, respectively, Supplemental Fig. 5.3). This super-resolution imaging determined that these two different CTLs are generally confined to separate nanodomains, and rarely co-exist within the same nanodomain.

5.5 DISCUSSION

How certain receptors are laterally organized on the membrane to enable binding to a large variety of potential ligands, and the interactions of these receptors with other membrane proteins and lipids that enable downstream signaling and internalization, remains a significant open question in biology. DC-SIGN, a CTL, forms clusters on the plasma membrane and these clusters subsequently bind to a diverse range of pathogens, ranging in size, surface composition, and infection route [4, 5]. The specific manner in which DC-SIGN clustering enables the receptor to bind to such pathogens is under active investigation [33-37]. In this work, we have investigated the distribution of DC-SIGN and another CTL, CD206, on dendritic cells using a super-resolution imaging technique, Blink Microscopy, which has a positional precision (FWHM) for a single dye on glass of ~40 nm. For reference, Blink was also used to image HA expressed on murine fibroblasts.

Blink Microscopy indicates that DC-SIGN and CD206 are organized into ~80 nm nanodomains on the surface of dendritic cells *that cannot be resolved by widefield fluorescence microscopic methods*. Thus, super-resolution [38, 39] and ultrastructural methods [5] are required to reveal this unexpected substructure. Interestingly, the viral influenza hemagglutinin protein, which forms dynamic clusters on the plasma membrane during viral budding, is also organized in ~80 nm nanodomains on the surface of a stable cell line that ectopically expresses HA. However, the overall lateral distribution of CTLs (DC-SIGN and CD206) and HA nanodomains in the plane of the plasma membrane differs greatly. In the case of DC-SIGN and CD206, nanodomains are randomly distributed on the

cell surface, whereas, in the case of HA, the nanodomains are clustered on length scales up to, and sometimes beyond, 1 μm, consistent with earlier studies [28]. Moreover, HA can exchange between its microdomains and the surrounding membrane on a rapid time-scale, whereas DC-SIGN cannot [9]. In the case of HA, which must assemble into domains capable of enclosing a virions of ~100 nm in diameter, the propensity to cluster and to be expressed in a specific lipid environment may be selecting for a non-random distribution of clusters across the cell surface.

Furthermore, as Blink Microscopy is based upon the sequential localizations of single dyes used for immunofluorescent labeling, it is possible to estimate the occupancy of DC-SIGN in nanodomains. This calculation is accomplished by dividing the number of Blink localizations per nanodomain by the average number of Blink localizations for a single Fab. This analysis estimates that a DC-SIGN nanodomain contains on average, *and as a lower bound*, 1-3 tetramers, suggesting both that DC-SIGN is not densely packed within nanodomains (Fig. 5.7) and that other proteins and lipids occupy such nanodomains. Thus, in the absence of ligand, DC-SIGN receptors are organized to have a 4- to 12- fold increased valency, at a minimum, compared to a single receptor. This multi-valency, in combination with the extreme lateral stability of the microdomains [8, 9], may allow the nanodomains to more effectively interact with weakly-binding antigen. Interestingly, it has been proposed that only a single HIV-1 Env (envelope glycoprotein) trimer is capable of initiating viral entry [40]. Furthermore, two-color Blink Microscopy determined that microdomains that appear by widefield microscopy to contain multiple CTLs are comprised of discrete nanodomains containing only one type of CTL that are positioned close to one another.

Our results raise a number of important questions for the manner in which DC-SIGN and other CTLs carry out their biological function, and also provide new information that will be useful for understanding the relationship between composition, structure and dynamics for other clusters of plasma membrane receptors in cell biology. First, will the disposition of some membrane proteins (e.g., DC-SIGN and CD206) into elemental nanodomains prove to be a paradigm for certain classes of receptors? Second, what other components reside in the DC-SIGN and CD206 nanodomains and how are these nanodomains stabilized? For DC-SIGN, these questions are particularly intriguing because microdomain stability appears not to depend directly on the presence of the cytoplasmic domain but rather on the ectodomain of the protein [9, 41]. Third, from an immunological point of view, how does the distribution of DC-SIGN nanodomains adjust to accommodate large and small pathogens with different glycan patterns on their surfaces? Answers to these questions will substantially increase our understanding of membrane domain structures, their relation to function and, in the case of DC-SIGN and other CTLs, perhaps provide clues for the design of new therapeutic agents for human infectious diseases.

5.6 CREDITS

We thank Judith White, Thomas Braciale, and Robert Doms for their generous gifts of the HAb2, FC125 and DC6 cell lines, respectively. This work was supported primarily by NIH grant GM-041402 (K.J. and N.L.T.). Additional funding was provided by NIH Cell

Migration Consortium grant GM-064346 (K.J.), NSF grant MCB-0641087 (N.L.T), and the Biophotonics IV program of the BMBF/VDI (P.T.).

5.7 FIGURE LEGENDS

Figure 5.1. Blink Microscopy on DC-SIGN plasma membrane nanodomains. (*A*) Image of DC-SIGN expression on a fixed dendritic cell stained with DC6 and anti-mouse ATTO655-Fab using diffraction-limited TIRF illumination. (*B*) Super-resolution Blink Microscopy image of DC-SIGN expression of the same region in (*A*). (*C*) Overlay of TIRF image (in red) and Blink image (in white). Scale bars, 500 nm; Scale bar inset, 100 nm.

Figure 5.2. Determining DC-SIGN nanodomain size using Blink Microscopy. Super-resolution Blink Microscopy image of DC-SIGN expression on a fixed dendritic cell stained with DC6 and anti-mouse ATTO655-Fab. The density of Blink localizations is denoted with black being least dense and white being most dense. Scale bar, 500 nm. A close-up view of the Blink localizations in a single DC-SIGN nanodomain, highlighted in the white box, appears to the right of the original image (Scale bar, 50 nm). A graph showing the distribution of the Blink localizations in the nanodomain in the x-dimension appears above the Blink image of the single nanodomain, and the Gaussian fit along the x-axis is shown with the black line. The data in the y-dimension are depicted in the graph in a vertical orientation to the right of the Blink image of the single nanodomain, and the Gaussian fit along the y-axis is shown with the red line.

Figure 5.3. Size estimation of DC-SIGN, CD206, and HA plasma membrane nanodomains using Blink Microscopy. FWHM values obtained by Blink Microscopy of single ATTO655-Fab molecules (black bars), DC-SIGN nanodomains on dendritic cells stained with DC6 and anti-mouse ATTO655-Fab (blue bars), CD206 nanodomains on

dendritic cells stained with AF2534 and anti-goat ATTO655-Fab (green bars), and HA nanodomains on HAb2 cells stained with FC125 and anti-mouse ATTO655-Fab (red bars). As shown, DC-SIGN, CD206 and HA nanodomains all have similar size distributions. The average nanodomain size is much larger than the spatial accuracy of the method as determined by imaging single ATTO655-Fab molecules and is much smaller than the conventional wide field fluorescence microscopy resolution limit.

Figure 5.4. DC-SIGN and CD206, but not HA, nanodomains are randomly distributed on the plasma membrane. (*A,D,G*) Binarized super-resolution Blink Microscopy images (cropped to exclude cell borders) of DC-SIGN expression on dendritic cells stained with DC6 and anti-mouse ATTO655-Fab (*A*), of CD206 expression on dendritic cells stained with AF2534 and anti-goat ATTO655-Fab (D), or of HA expression on HAb2 cells stained with FC125 and anti-mouse ATTO655-Fab (*G*); these images are representative of a collection of 16, 13, and 12 analyzed for DC-SIGN, CD206, and HA, respectively. (*B,E,H*) Results of a modified Hopkin's test for spatial randomness on centroids of DC-SIGN (*B*), CD206 (*E*), or HA (*H*) nanodomains (in blue) from the images in (*A*), (*D*), and (*G*), respectively. The distribution expected if the centroids were distributed randomly is depicted with the red lines. A non-random distribution or clustering would be indicated by a shift in the distribution to the right or left. (*C,F,I*) Results from a Ripley's K test for spatial randomness on centroids of DC-SIGN (*C*), CD206 (*F*), or HA (*I*) nanodomains (black lines) from the images in (*A*), (*D*), and (*G*), respectively. The red lines indicate the 95% confidence interval for complete spatial randomness calculated from 1000 Monte Carlo simulations of random distributions of centroids. Scale bars, 500 nm.

Figure 5.5. Estimated occupancy of DC-SIGN, CD206, and HA in single nanodomains using Blink Microscopy. (*A*) Histogram of the number of Blink localizations for single ATTO655-Fab antibodies on glass (black bars), single DC-SIGN nanodomains on dendritic cells stained with DC6 and anti-mouse ATTO655-Fab (blue bars), CD206 nanodomains on dendritic cells stained with AF2534 and anti-goat ATTO655-Fab (green bars), and HA nanodomains on HAb2 cells stained with FC125 and anti-mouse ATTO655-Fab (red bars). (*B*) Histogram of the minimum number of DC-SIGN molecules per nanodomain on dendritic cells (red bars), of CD206 molecules per nanodomain on dendritic cells (green bars), and of HA molecules per nanodomain on HAb2 cells (red bars). Minimal occupancies for each nanodomain type were determined by dividing the number of blink localizations per nanodomain by the average number of blink localizations for a single Fab on glass.

Figure 5.6. DC-SIGN and CD206 plasma membrane nanodomains are usually spatially distinct. Overlay image of DC-SIGN (green) and CD206 (red) expression on a dendritic cell stained with DCN46, anti-mouse Alexa546, AF2534 and anti-goat ATTO655-Fab using two-color Blink Microscopy. Regions in yellow boxes are shown at higher magnification to the right and show examples of significant overlap (top), minor overlap (middle) and no overlap (bottom); the latter is the most prevalent situation by far. Scale bar, 500 nm; Scale bars insets, 100 nm.

Figure 5.7. Model of occupancy of DC-SIGN in single nanodomains. A schematic depicting the distribution of DC-SIGN tetramers (in green) in a single DC-SIGN nanodomain (blue) on a dendritic cell. If the entire area of a ~76 nm in diameter nanodomain was

occupied by DC-SIGN tetramers (~8 nm in diameter [31, 32]), one would expect ~90 tetramers to be in a single nanodomain. However, data using the super-resolution Blink Microscopy imaging method indicates that, as a lower limit, as few as 1-3 tetramers occupy a single DC-SIGN domain, leaving room for many other receptors and lipids to co-occupy the nanodomains.

5.8 SUPPLEMENTAL FIGURE LEGENDS

Supplemental Figure 5.1. Convolution of Blink Microscopy images of DC-SIGN plasma membrane nanodomains. (*A*) Image of DC-SIGN expression on a dendritic cell stained with DC6 and anti-mouse ATTO655-Fab using diffraction-limited TIRF illumination. (*B*) Super-resolution Blink Microscopy image of DC-SIGN expression of the same region in (*A*). (*C*) Overlay of convoluted Blink image (*A*, in red) and Blink image (*B*, in white). Scale bars, 500 nm.

Supplemental Figure 5.2. Single-step photobleaching of individual ATTO655-Fabs. Histogram of the number of single photobleaching steps from individual Atto655-Fabs on glass. Mean: 1.4, median: 1, stdev: 0.54, min: 1, max: 3, count= 46.

Supplemental Figure 5.3. Assessement of overlap between two-color CD206 and DC-SIGN Blink Microscopy images and two simulated random distributions of clusters. (*A*) Representative overlay image of DC-SIGN (green) and CD206 (red) expression on a dendritic cell stained with DCN46, anti-mouse Alexa546 IgG, AF2534 and anti-goat

ATTO655-Fab. The image was acquired by using two-color Blink Microscopy (one of 20 analyzed). (*B*) A representative simulated Blink Microscopy image of two randomly arranged clusters (one of 100 analyzed). (*C*) A graph comparing the calculated % colocalization of DC-SIGN and CD206 from two color Blink images and from simulated images of two randomly distributed sets of clusters, in which any overlap is of a stochastic nature (20 and 100 images analyzed, respectively). Error bars represent standard deviations. (*D,E*) A Ripley's-K bivariate analysis is shown as L(t)-t (solid black line) for the representative analyzed image for DC-SIGN with CD206 (*D*), and the representative simulated Blink Microscopy image of two randomly arranged clusters (*E*). When L(t)-t is between the dashed lines (randomness confidence interval), the distribution is considered random; clustering is indicated when the L(t)-t is above the dashed lines. Scale bars, 1 μm.

TABLE 5.1

Characteristics of DC-SIGN, CD206, and HA nanodomains as measured by Blink Microscopy*

	DC-SIGN Domains			CD206 Domains			HA Domains			Single ATTO655-Fabs		
	Mean (Median)	Range	n (m)	Mean (Median)	Range	n (m)	Mean (Median)	Range	n (m)	Mean (Median)	Range	n (m)
Overall FWHM (nm)	76 ± 42 (66)	20-991	3706 (17)	70 ± 41 (59)	17-300	2819 (13)	74 ± 47 (61)	24-486	2910 (12)	39 ± 11 (38)	24-91	191 (6)
Area (nm^2)	5100 ± 6100 (3300)	670-80814	1853 (17)	4400 ± 4700 (2800)	360-45247	1409 (13)	5200 ± 7800 (2900)	559-90554	1455 (12)	1200 ± 580 (1200)	553-3285	97 (6)
Number of Blink Localizations	163 ± 230 (82)	8-2283	1960 (17)	78 ± 168 (24)	5-2357	1409 (13)	120 ± 142 (71)	11-1688	1099 (12)	25 ± 18 (22)	5-111	97 (6)

*Uncertainties are standard deviations. Parameters m and n are the numbers of images and nanodomains analyzed, respectively.

FIGURE 5.1

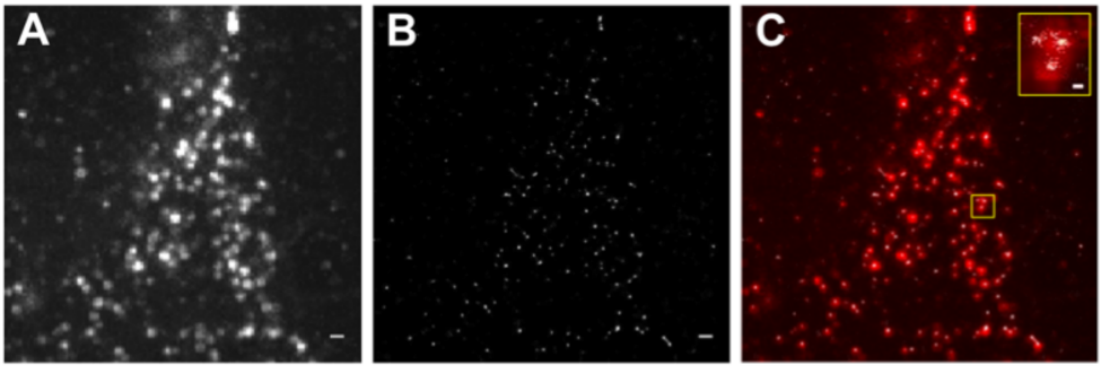

FIGURE 5.2

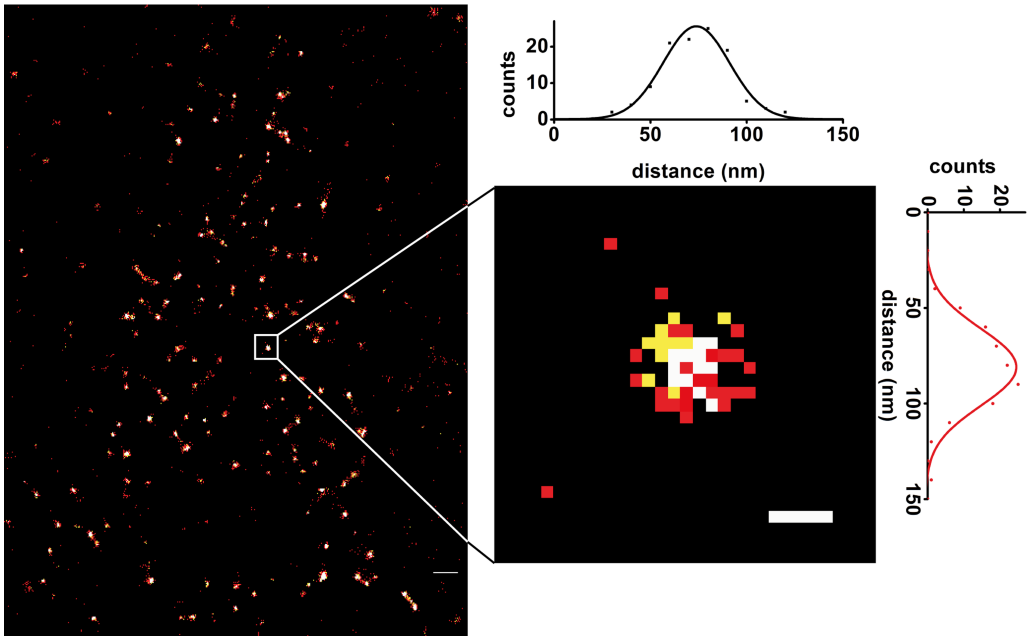
counts
20
10
0
0
50
100
150
distance (nm)
counts
0
10
20
0
50
100
150
distance (nm)

FIGURE 5.3

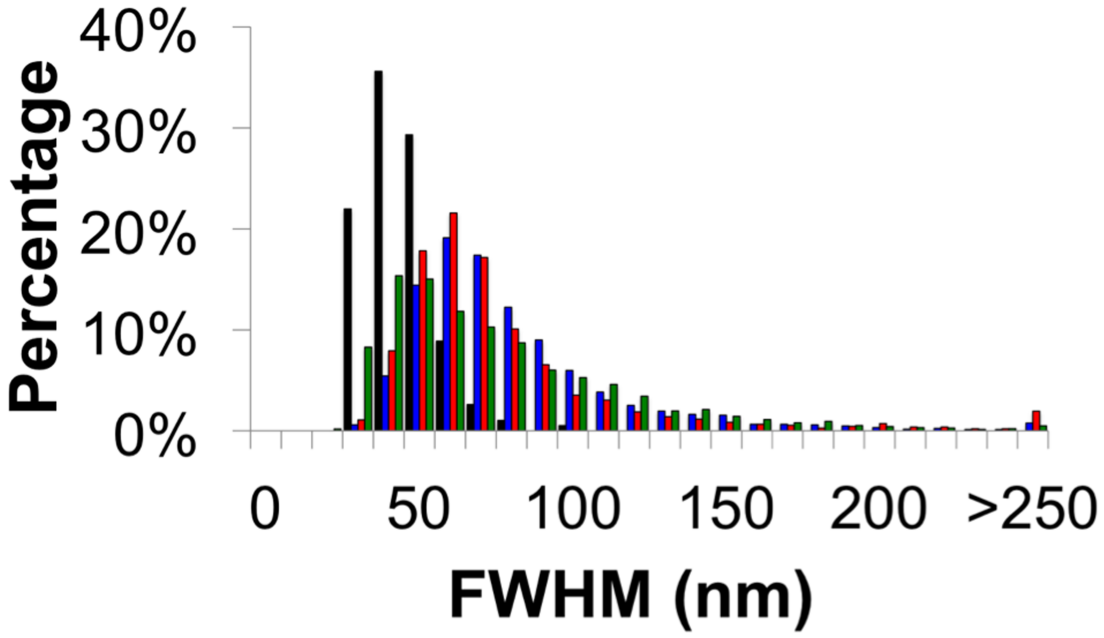

FIGURE 5.4

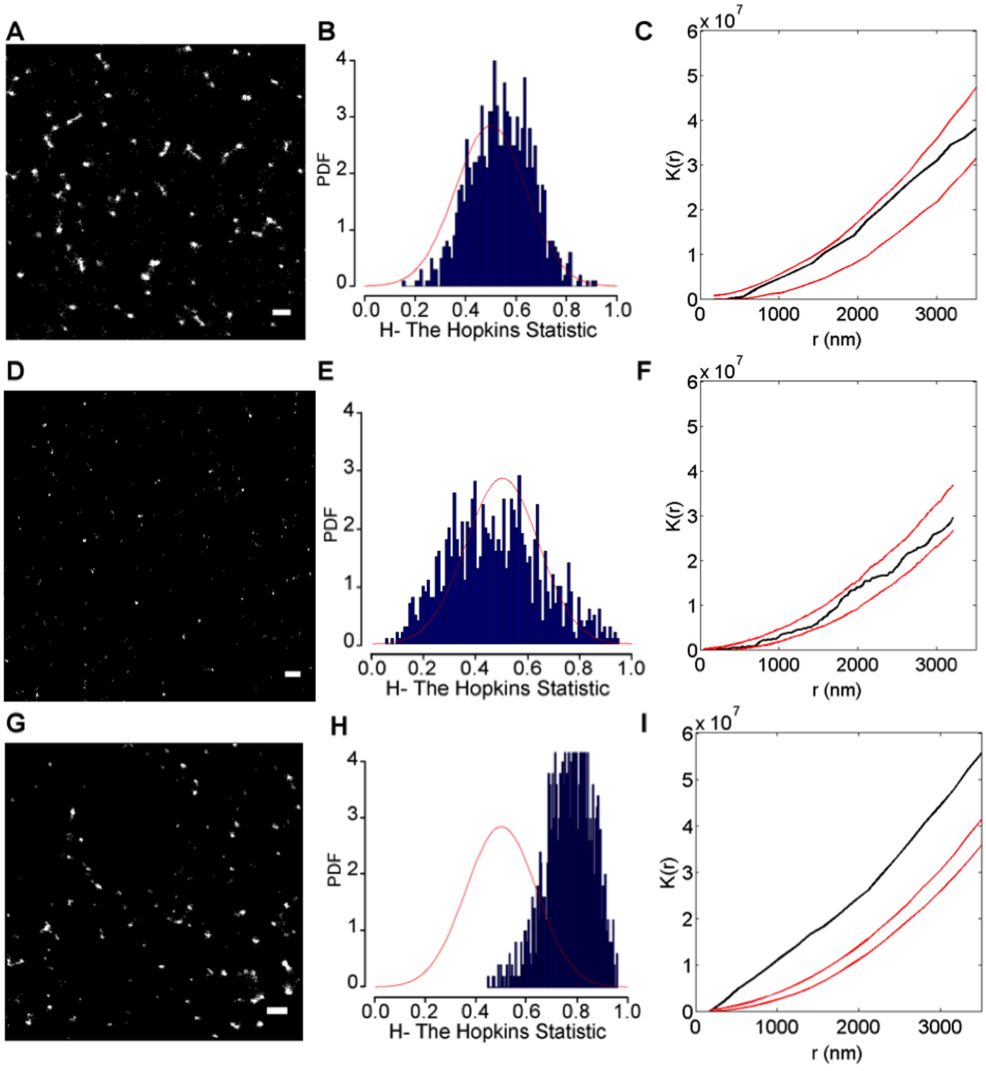

FIGURE 5.5

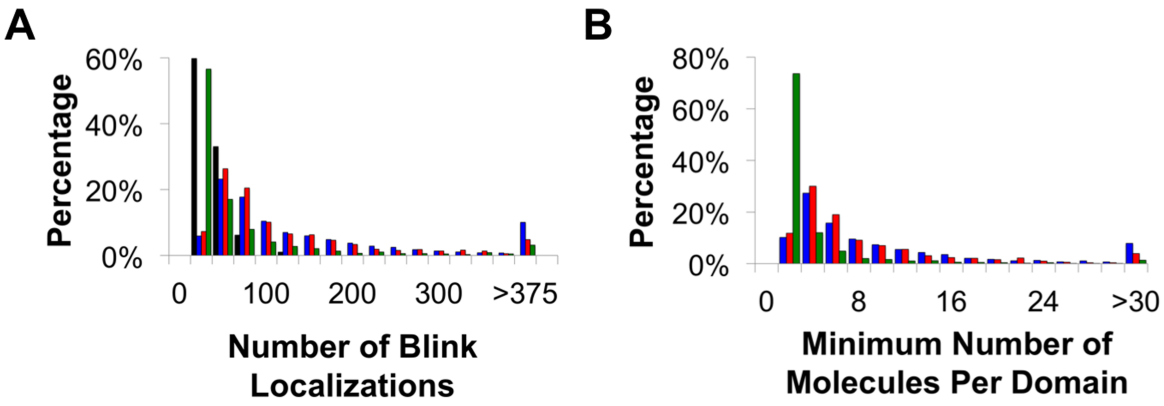
A
Percentage
60%
40%
20%
0%
0
100
200
300
>375
Number of Blink Localizations
B
Percentage
80%
60%
40%
20%
0%
0
8
16
24
>30
Minimum Number of Molecules Per Domain

FIGURE 5.6

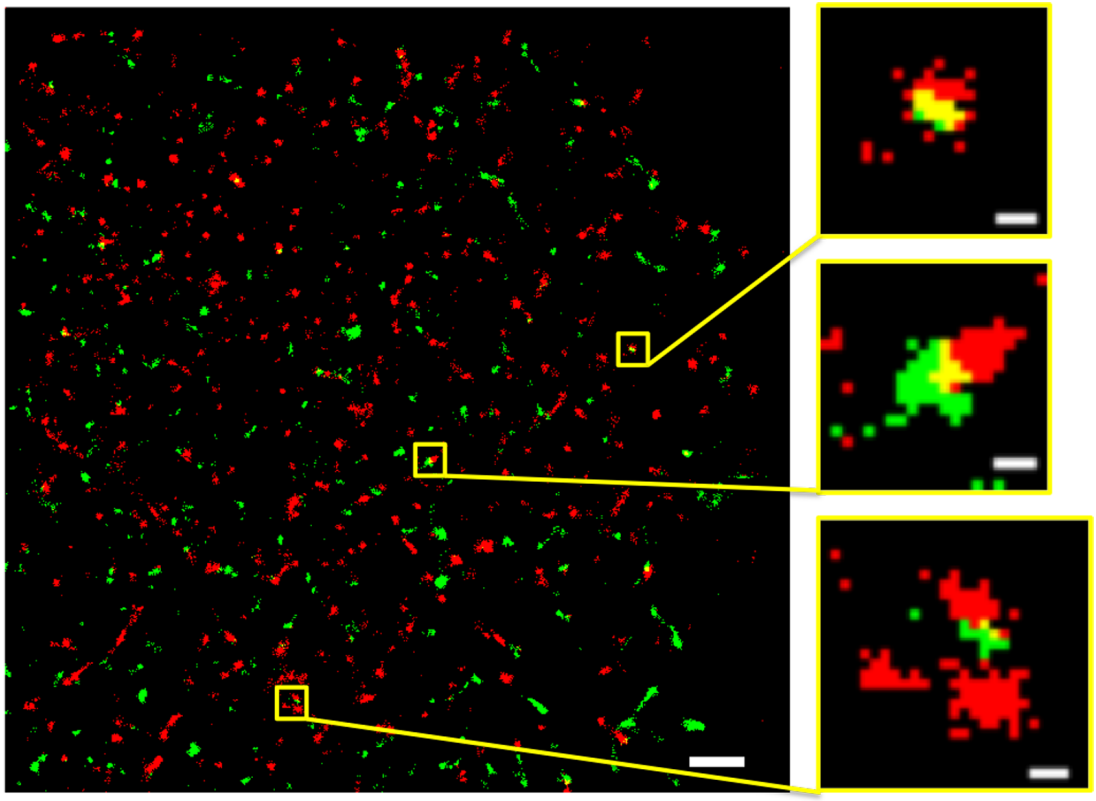

FIGURE 5.7

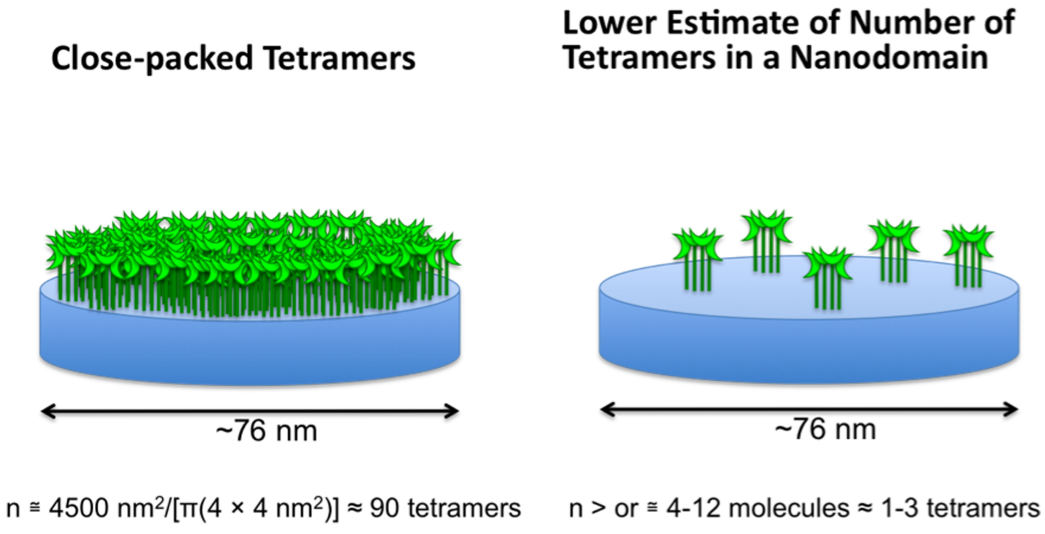
Close-packed Tetramers
Lower Estimate of Number of Tetramers in a Nanodomain
~76 nm
~76 nm
n ≅ 4500 nm²/[π(4 × 4 nm²)] ≈ 90 tetramers
n > or ≅ 4-12 molecules ≈ 1-3 tetramers

SUPPLEMENTAL FIGURE 5.1

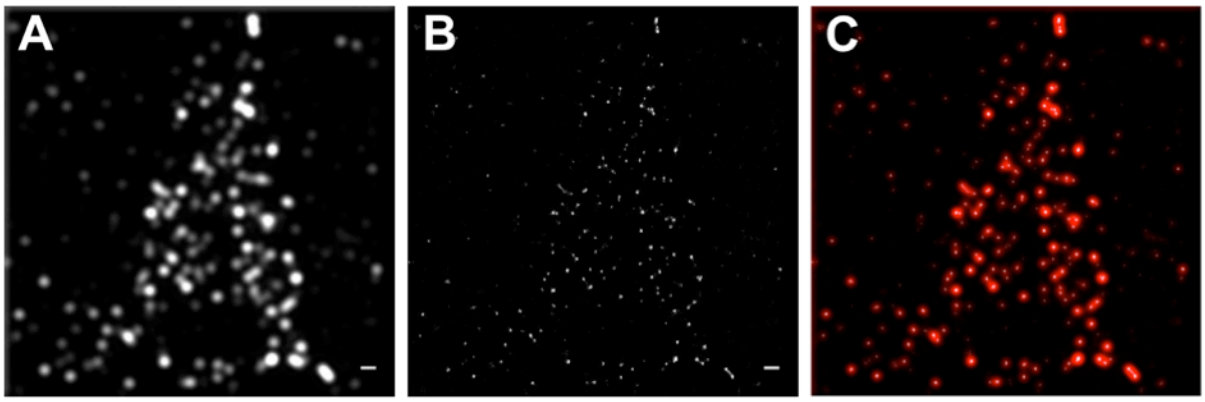

SUPPLEMENTAL FIGURE 5.2

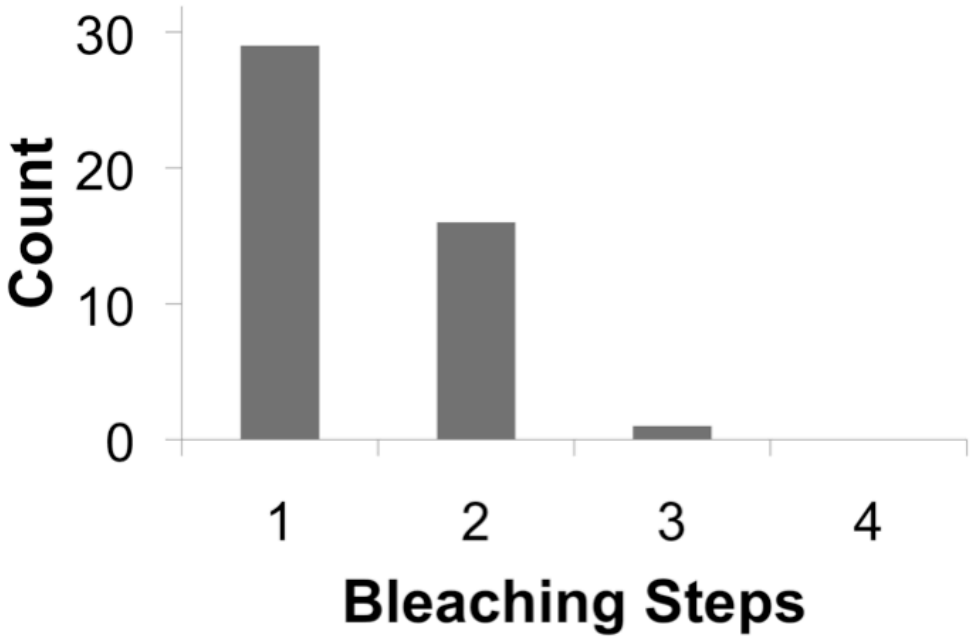

SUPPLEMENTAL FIGURE 5.3

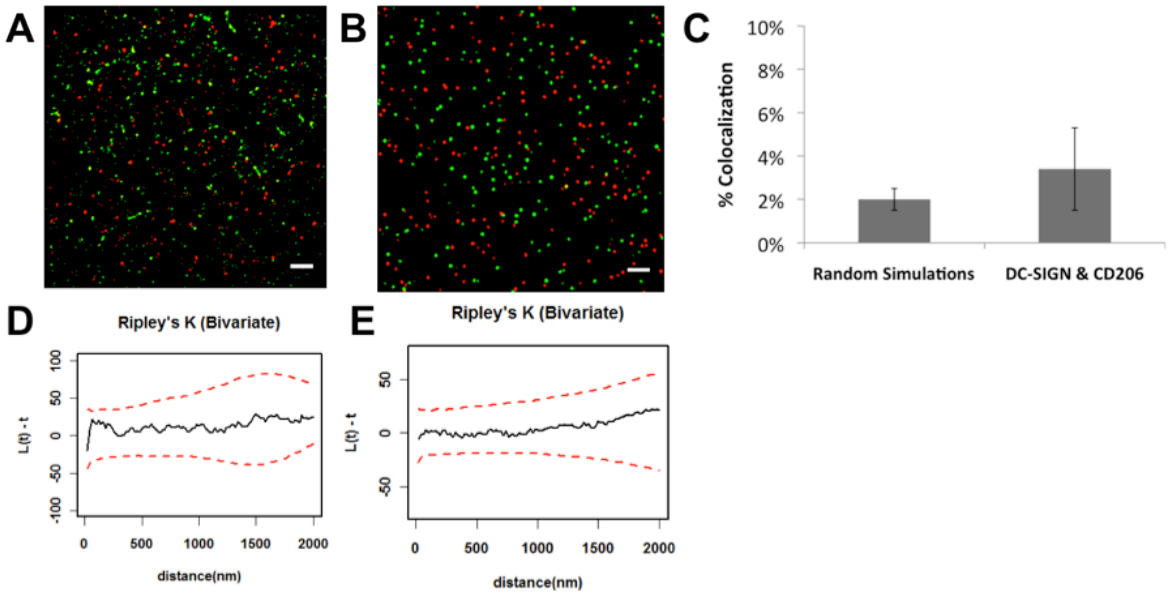

5.9 REFERENCES

1. Banchereau, J., and R. M. Steinman. 1998. Dendritic cells and the control of immunity. Nature 392:245-252.

2. Altfeld, M., L. Fadda, D. Frleta, and N. Bhardwaj. 2011. DCs and NK cells: critical effectors in the immune response to HIV-1. Nat Rev Immunol 11:176-186.

3. Cambi, A., M. Koopman, and C. G. Figdor. 2005. How C-type lectins detect pathogens. Cellular Microbiology 7:481-488.

4. Svajger, U., M. Anderluh, M. Jeras, and N. Obermajer. 2010. C-type lectin DC-SIGN: an adhesion, signalling and antigen-uptake molecule that guides dendritic cells in immunity. Cell Signal 22:1397-1405.

5. Cambi, A., F. de Lange, N. M. van Maarseveen, M. Nijhuis, B. Joosten, E. M. H. P. van Dijk, B. I. de Bakker, J. A. Fransen, P. H. M. Bovee-Geurts, F. N. van Leeuwen, N. F. Van Hulst, and C. G. Figdor. 2004. Microdomains of the C-type lectin DC-SIGN are portals for virus entry into dendritic cells. Journal of Cell Biology 164:145-155.

6. de Bakker, B. I., F. de Lange, A. Cambi, J. P. Korterik, E. M. van Dijk, N. F. van Hulst, C. G. Figdor, and M. F. Garcia-Parajo. 2007. Nanoscale organization of the pathogen receptor DC-SIGN mapped by single-molecule high-resolution fluorescence microscopy. Chemphyschem 8:1473-1480.

7. Koopman, M., A. Cambi, B. I. de Bakker, B. Joosten, C. G. Figdor, N. F. van Hulst, and M. F. Garcia-Parajo. 2004. Near-field scanning optical microscopy in liquid for high resolution single molecule detection on dendritic cells. FEBS Letters 573:6-10.

8. Neumann, A. K., N. L. Thompson, and K. Jacobson. 2008. Distribution and lateral mobility of DC-SIGN on immature dendritic cells--implications for pathogen uptake. J Cell Sci 121:634-643.

9. Itano, M. S., A. K. Neumann, P. Liu, F. Zhang, E. Gratton, W. J. Parak, N. L. Thompson, and K. Jacobson. 2011. DC-SIGN and influenza hemagglutinin dynamics in plasma membrane microdomains are markedly different. Biophys J 100:2662-2670.

10. Mitchell, D. A., A. J. Fadden, and K. Drickamer. 2001. A novel mechanism of carbohydrate recognition by the C-type lectins DC-SIGN and DC-SIGNR. Subunit organization and binding to multivalent ligands. J Biol Chem 276:28939-28945.

11. Curtis, B. M., S. Scharnowske, and A. J. Watson. 1992. Sequence and expression of a membrane-associated C-type lectin that exhibits CD4-independent binding of human

immunodeficiency virus envelope glycoprotein gp120. Proc Natl Acad Sci U S A 89:8356-8360.

12. Soilleux, E. J., R. Barten, and J. Trowsdale. 2000. DC-SIGN; a related gene, DC-SIGNR; and CD23 form a cluster on 19p13. J Immunol 165:2937-2942.

13. Su, S. V., P. Hong, S. Baik, O. A. Negrete, K. B. Gurney, and B. Lee. 2004. DC-SIGN binds to HIV-1 glycoprotein 120 in a distinct but overlapping fashion compared with ICAM-2 and ICAM-3. J Biol Chem 279:19122-19132.

14. Feinberg, H., Y. Guo, D. A. Mitchell, K. Drickamer, and W. I. Weis. 2005. Extended neck regions stabilize tetramers of the receptors DC-SIGN and DC-SIGNR. J Biol Chem 280:1327-1335.

15. Serrano-Gomez, D., E. Sierra-Filardi, R. T. Marinez-Nunez, E. Caparros, R. Delgado, M. A. Munoz-Fernandez, M. A. Abad, J. Jimenez-Barbero, M. Leal, and A. L. Corbi. 2008. Structural requirements for multimerization of the pathogen receptor Dendritic Cell-specific ICAM3-grabbing Non-integrin (CD209) on the cell surface. The Journal of Biological Chemistry 283:15.

16. Yu, Q. D., A. P. Oldring, A. S. Powlesland, C. K. Tso, C. Yang, K. Drickamer, and M. E. Taylor. 2009. Autonomous tetramerization domains in the glycan-binding receptors DC-SIGN and DC-SIGNR. J Mol Biol 387:1075-1080.

17. Steinhauer, C., C. Forthmann, J. Vogelsang, and P. Tinnefeld. 2008. Superresolution microscopy on the basis of engineered dark states. J Am Chem Soc 130:16840-16841.

18. Leser, G. P., and R. A. Lamb. 2005. Influenza virus assembly and budding in raft-derived microdomains: a quantitative analysis of the surface distribution of HA, NA and M2 proteins. Virology 342:215-227.

19. Takeda, M., G. P. Leser, C. J. Russell, and R. A. Lamb. 2003. Influenza virus hemagglutinin concentrates in lipid raft microdomains for efficient viral fusion. Proceedings of the National Academy of Sciences of the United States of America 100:14610-14617.

20. Baribaud, F., S. Pohlmann, T. Sparwasser, M. T. Kimata, Y. K. Choi, B. S. Haggarty, N. Ahmad, T. Macfarlan, T. G. Edwards, G. J. Leslie, J. Arnason, T. A. Reinhart, J. T. Kimata, D. R. Littman, J. A. Hoxie, and R. W. Doms. 2001. Functional and antigenic characterization of human, rhesus macaque, pigtailed macaque, and murine DC-SIGN. J Virol 75:10281-10289.

21. Braciale, T. J., M. E. Andrew, and V. L. Braciale. 1981. Simultaneous expression of H-2-restricted and alloreactive recognition by a cloned line of influenza virus-specific cytotoxic T lymphocytes. J Exp Med 153:1371-1376.

22. Vogelsang, J., T. Cordes, C. Forthmann, C. Steinhauer, and P. Tinnefeld. 2009. Controlling the fluorescence of ordinary oxazine dyes for single-molecule switching and superresolution microscopy. Proc Natl Acad Sci U S A 106:8107-8112.

23. Steinhauer, C., R. Jungmann, T. L. Sobey, F. C. Simmel, and P. Tinnefeld. 2009. DNA origami as a nanoscopic ruler for super-resolution microscopy. Angew Chem Int Ed Engl 48:8870-8873.

24. Thompson, R. E., D. R. Larson, and W. W. Webb. 2002. Precise nanometer localization analysis for individual fluorescent probes. Biophys J 82:2775-2783.

25. Hammer, Ø., D. A. T. Harper, and P. D. Ryan. 2001. PAST: Paleontological Statistics Software Package for Education and Data Analysis. Palaeontologia Electronica 4:9pp.

26. Zhang, J., K. Leiderman, J. R. Pfeiffer, B. S. Wilson, J. M. Oliver, and S. L. Steinberg. 2006. Characterizing the topography of membrane receptors and signaling molecules from spatial patterns obtained using nanometer-scale electron-dense probes and electron microscopy. Micron 37:14-34.

27. Vogelsang, J., C. Steinhauer, C. Forthmann, I. H. Stein, B. Person-Skegro, T. Cordes, and P. Tinnefeld. 2010. Make them blink: probes for super-resolution microscopy. Chemphyschem 11:2475-2490.

28. Hess, S. T., T. J. Gould, M. V. Gudheti, S. A. Maas, K. D. Mills, and J. Zimmerberg. 2007. Dynamic clustered distribution of hemagglutinin resolved at 40 nm in living cell membranes discriminates between raft theories. Proceedings of the National Academy of Sciences of the United States of America 104:17370-17375.

29. Hess, S. T., M. Kumar, A. Verma, J. Farrington, A. Kenworthy, and J. Zimmerberg. 2005. Quantitative electron microscopy and fluorescence spectroscopy of the membrane distribution of influenza hemagglutinin. The Journal of Cell Biology 169:12.

30. Gamblin, S. J., and J. J. Skehel. 2010. Influenza hemagglutinin and neuraminidase membrane glycoproteins. J Biol Chem 285:28403-28409.

31. Guo, Y., H. Feinberg, E. Conroy, D. A. Mitchell, R. Alvarez, O. Blixt, M. E. Taylor, W. I. Weis, and K. Drickamer. 2004. Structural basis for distinct ligand-binding and targeting properties of the receptors DC-SIGN and DC-SIGNR. Nat Struct Mol Biol 11:591-598.

32. Feinberg, H., D. A. Mitchell, K. Drickamer, and W. I. Weis. 2001. Structural basis for selective recognition of oligosaccharides by DC-SIGN and DC-SIGNR. Science 294:2163-2166.

33. Menon, S., K. Rosenberg, S. A. Graham, E. M. Ward, M. E. Taylor, K. Drickamer, and D. E. Leckband. 2009. Binding-site geometry and flexibility in DC-SIGN

demonstrated with surface force measurements. Proc Natl Acad Sci U S A 106:11524-11529.

34. Hodges, A., K. Sharrocks, M. Edelmann, D. Baban, A. Moris, O. Schwartz, H. Drakesmith, K. Davies, B. Kessler, A. McMichael, and A. Simmons. 2007. Activation of the lectin DC-SIGN induces an immature dendritic cell phenotype triggering Rho-GTPase activity required for HIV-1 replication. Nat Immunol 8:569-577.

35. Gringhuis, S. I., J. den Dunnen, M. Litjens, B. van Het Hof, Y. van Kooyk, and T. B. Geijtenbeek. 2007. C-type lectin DC-SIGN modulates Toll-like receptor signaling via Raf-1 kinase-dependent acetylation of transcription factor NF-kappaB. Immunity 26:605-616.

36. Cambi, A., D. S. Lidke, D. J. Arndt-Jovin, C. G. Figdor, and T. M. Jovin. 2007. Ligand-conjugated quantum dots monitor antigen uptake and processing by dendritic cells. Nano Lett 7:970-977.

37. Avota, E., E. Gulbins, and S. Schneider-Schaulies. 2011. DC-SIGN mediated sphingomyelinase-activation and ceramide generation is essential for enhancement of viral uptake in dendritic cells. PLoS Pathog 7:e1001290.

38. Betzig, E., G. H. Patterson, R. Sougrat, O. W. Lindwasser, S. Olenych, J. S. Bonifacino, M. W. Davidson, J. Lippincott-Schwartz, and H. F. Hess. 2006. Imaging intracellular fluorescent proteins at nanometer resolution. Science 313:1642-1645.

39. Hell, S. W. 2009. Microscopy and its focal switch. Nat Methods 6:24-32.

40. Yang, X., S. Kurteva, X. Ren, S. Lee, and J. Sodroski. 2005. Stoichiometry of envelope glycoprotein trimers in the entry of human immunodeficiency virus type 1. J Virol 79:12132-12147.

41. Liu, P., X. Wang, M. S. Itano, A. K. Neumann, N. L. Thompson, and K. Jacobson. 2012. The Formation and Stability of DC-SIGN Microdomains Require its Extracellular Moiety. Traffic, in press.

CHAPTER 6

Conclusions and Outlook

6.1 Surprising Stability of DC-SIGN Microdomains

The clustering of DC-SIGN is required for efficient pathogen binding and internalization [1], however the molecular interactions that mediate the clustering of DC-SIGN were not known. Work presented in Chapter 4 of this dissertation extends previous work by our lab, which had demonstrated that DC-SIGN domains failed to recover fluorescence following photobleaching [2]. Three complementary fluorescence-based methods of analysis (i.e., fluorescence recovery after photobleaching (FRAP), line-scan fluorescence correlation spectroscopy, and defined valency Qdot tracking), determined that DC-SIGN is extremely restricted in terms of its mobility within microdomains and therefore does not exchange with DC-SIGN in the surrounding membrane on a measurable time-scale during FRAP experiments [3]. Conventional notions would suggest that such stability of a membrane protein would be regulated by interactions between the cytoplasmic tail of DC-SIGN and the membrane-apposed cytoskeleton. However, mutants of DC-SIGN in which the cytoplasmic tail was almost completely deleted still formed very stable microdomains on the plasma membrane [3, 4]. Recent work, led by Dr. Ping Liu, utilized a mutational strategy to determine that the molecular basis of DC-SIGN domain formation and stability resides in the extracellular region of the protein, specifically the carbohydrate recognition domain [4]. Further, administration

of two different actin-disrupting drugs did not affect DC-SIGN microdomain formation [4], which also supports a model in which the extracellular region of DC-SIGN mediates microdomain stability.

6.2 Unexpected Composition, Structure and Distribution of DC-SIGN Domains

Previous work using widefield microscopy had indicated that DC-SIGN assembles into microdomains ranging from below the diffraction limit (~300 nm) to over 1.5 μm in diameter [2]. Two-color widefield microscopy experiments, presented in Chapter 4, suggested that DC-SIGN domains could contain other C-type lectin molecules and could also allow lipids to transverse through the microdomains [3]. These experiments suggested that DC-SIGN domains were not densely packed with protein, but instead are likely to contain other proteins and lipids, not yet identified. Further investigations using the super-resolution method of Blink Microscopy, in Chapter 5, determined that DC-SIGN is predominantly expressed in randomly distributed nanodomains, which are <80 nm in diameter, and that these nanodomains are randomly distributed across the cell surface [5]. Therefore, nanodomains could be in close proximity to one another so that they appeared much larger when viewed by widefield microscopy [5]. Analysis using Blink Microscopy [5] and preliminary results using quantitative total internal reflection fluorescence (TIRF) microscopy [6] estimate that DC-SIGN nano-/microdomains, respectively, generally contain fewer than 12 molecules, or three tetramers, as a lower limit. Additionally, DC-SIGN nanodomains do not generally co-localize with CD206 nanodomains [5]. Thus, proteins that appeared co-

localized using standard widefield microscopy methods are found to be spatially distinct when viewed using methods with higher resolution.

6.3 Relating Domain Characteristics to DC-SIGN's Biological Function

The manner in which the characteristics of DC-SIGN domains directly relate to the biological functions of DC-SIGN is an area of ongoing investigation. It is possible that the extreme stability of DC-SIGN microdomains helps to maintain a particular intradomain structure that enables more efficient pathogen recognition and/or internalization. For example, a particular arrangement of tetramers, number of molecules, and/or spatial arrangement of carbohydrate recognition domains may increase the relatively weak binding avidity of a single carbohydrate recognition domain for high mannose glycan residues. Also, stability on the membrane may allow for stable recruitment of other proteins and lipids important for initiating downstream signaling events following pathogen recognition. And further, lack of diffusion on the membrane may also provide stability during rapid transport from sites of pathogen binding to the perinuclear region, which is the predominant site of internalization [2].

Much still remains unknown regarding the regulation of DC-SIGN microdomain stability. Recent data suggests that mutation of one of the seven residues involved in calcium binding in DC-SIGN's carbohydrate recognition domain results in loss of microdomain formation and dynamic diffusion of DC-SIGN in the plasma membrane [4]. Therefore, it appears that active binding interactions between saccharides and the extracellular domain of DC-SIGN are responsible for DC-SIGN's ability to form stable

domains on the plasma membrane. However, whether DC-SIGN is regulated by saccharides present in the extra cellular matrix, on glycosoylated transmembrane adaptor proteins linked to the membrane-apposed cytoskeleton, or present on a currently unidentified source is an area of ongoing investigation. Further, whether or not release of such saccharide binding, either by direct competition with another saccharide and/or steric hindrance at the binding site, would also inhibit DC-SIGN's ability to form domains, and therefore the ability of DC-SIGN to bind and internalize pathogens, remains a possibility. An important step in identifying the factors regulating DC-SIGN stability is identifying the proteins and lipids that interact with DC-SIGN. A proteomics-based investigation on identifying proteins that are pulled-down with beads coated with DC-SIGN IgG is ongoing and will be key to answering many of these remaining questions. These investigations are especially important considering the fact that DC-SIGN exists in clusters much smaller than the diffraction limit, and that proteins that appear co-localized using widefield microscopy methods actually reside in distinct, though proximate locations.

All of the work presented in this dissertation was performed in the absence of pathogens. However, it is now known that DC-SIGN and CD206 assemble into large patches (> 2μm in diameter) at pathogen contact sites with yeast particles and that the interaction between the yeast particle and CD206 drives the formation of the "fungipod," an actin-rich cell extension that stably attaches to the yeast [7]. Identifying the manner in which DC-SIGN nanodomains assemble into the large patches when incubated with yeast particles may provide important insight into the regulation of DC-SIGN diffusion and

pathogen recognition by DC-SIGN. Super-resolution imaging of dendritic cells that have been exposed to pathogens will provide important information regarding the structure of the DC-SIGN domains. And further, super-resolution imaging of cells following the time course of pathogen recognition and internalization and/or with a variety of ligands will identify important steps in the regulation of DC-SIGN pathogen recognition. In all, C-type lectin domains emerge as a new and unique model of how stable protein aggregation in the plasma membrane can lead to important biological function.

6.4 References

1. Cambi, A., F. de Lange, N. M. van Maarseveen, M. Nijhuis, B. Joosten, E. M. van Dijk, B. I. de Bakker, J. A. Fransen, P. H. Bovee-Geurts, F. N. van Leeuwen, N. F. Van Hulst, and C. G. Figdor. 2004. Microdomains of the C-type lectin DC-SIGN are portals for virus entry into dendritic cells. J Cell Biol 164:145-155.

2. Neumann, A. K., N. L. Thompson, and K. Jacobson. 2008. Distribution and lateral mobility of DC-SIGN on immature dendritic cells--implications for pathogen uptake. J Cell Sci 121:634-643.

3. Itano, M. S., A. K. Neumann, P. Liu, F. Zhang, E. Gratton, W. J. Parak, N. L. Thompson, and K. Jacobson. 2011. DC-SIGN and influenza hemagglutinin dynamics in plasma membrane microdomains are markedly different. Biophys J 100:2662-2670.

4. Liu, P., X. Wang, M. S. Itano, A. K. Neumann, K. Jacobson, and N. L. Thompson. 2012. The Formation and Stability of DC-SIGN Microdomains Require its Extracellular Moiety. Traffic, in press.

5. Itano, M. S., C. Steinhauer, J. Schmied, C. Forthmann, P. Liu, A. K. Neumann, N. L. Thompson, P. Tinnefeld, and K. Jacobson. 2012. Super-resolution imaging of DC-SIGN and Influenza hemagglutinin nanodomains on plasma membranes using Blink Microscopy. Biophysical Journal 102:1534-1542.

6. Liu, P., X. Wang, M. S. Itano, A. K. Neumann, N. L. Thompson, and K. Jacobson. 2012. Quantification of DC-SIGN in nanodomains on plasma membranes using TIRF Microscopy. in preparation.

7. Neumann, A. K., and K. Jacobson. 2010. A novel pseudopodial component of the dendritic cell anti-fungal response: the fungipod. PLoS Pathog 6:e1000760.